

**The influence of snow physical properties on
the ski-snow friction: From real scale measurements on skis
to investigations of fundamental processes on the microscale**

Zur Erlangung des akademischen Grades eines
DOKTORS DER INGENIEURWISSENSCHAFTEN (Dr.-Ing.)

von der KIT-Fakultät für Maschinenbau des
Karlsruher Instituts für Technologie (KIT)

angenommene

DISSERTATION

von

Dipl.-Sporting. Fabian Wolfsperger

Tag der mündlichen Prüfung: 24.06.2024

Hauptreferent: Prof. Dr.-Ing. habil. Matthias Scherge
Korreferent: Prof. Dr.-Ing. habil. Volker Schulze

Vorsitzender: Prof. Dr.-Ing. Marcus Geimer

Abstract

Previous research has shown that friction between ski and snow can vary substantially due to changes in snow conditions. However, despite multiple attempts over the last decades, to date no model can predict ski-snow friction from snow physical properties. Besides the difficulty to access tribological parameters under realistic skiing conditions and the limited transferability of laboratory conditions to the real case, this is because processes that control snow friction are still not fully understood. For the first time, this work combines kinematic athlete data and comprehensive snow surface measurements to infer the coefficient of friction of skis and snowboards across a wide range of snow conditions. Beyond that, laboratory experiments were carried out to investigate slider-snow interactions on dry and wet snow focusing the influence of snow physical properties on the accumulation of interfacial water as well on the formation of the real contact area.

Athletes' point mass kinematics were recorded at more than 200 straight gliding runs with differential global navigation satellite systems. The subjects' air drag and lift were deployed from wind tunnel measurements. Along with the kinematic data and data from wind measurements, a mechanical model of the athlete was established to solve the equation of motion for the coefficient of friction between a ski/snowboard and the snow. The friction coefficients for ski (snowboard) ranged from 0.023 ± 0.006 (0.026 ± 0.008) to 0.139 ± 0.018 (0.143 ± 0.017) and could be explained well ($R^2_{adj} = 0.77$) from the measured snow parameters using a multivariate statistical model. Minimal friction occurred at speeds between about 5 and 12 m s^{-1} depending mainly on the snow temperature and wetness. To gain insights into the processes behind the quantified snow friction on the field, various laboratory experiments with different snow types were conducted: (1) slider-snow friction measurements, (2) mechanical characterization of snow under compression including (3) capacitance measurements to estimate interfacial water accumulations, and (4) estimations of the formed real contact area deduced from high resolution x-ray computed tomography. Friction coefficients ranged from 0.06 ± 0.01 , on dry coarse-grained snow, to about 0.100 ± 0.006 on wet fine-grained snow. Snow deformations were dominated by permanent brittle and plastic deformation, but also elastic and viscoelastic deformations were measured, and, based on a rheological model, viscoplastic deformation were shown to gain relevance on fine-grained wet snow. On the same type of snow, enhanced water accumulations near the ski-snow interface were found. Besides the high water-holding capacity of fine-grained wet snow, its high compressibility was identified as a key property. Relative real contact areas were found between 2.3 and 6 %, assuming an entirely smooth slider. In combination with the quantified snow properties and speed dependence of the ski-snow friction found on the field, the following conclusion were made concerning the frictional processes: (1) Even on groomed snow macroscopic compaction and plowing can contribute relevantly to the snow friction. (2) The speed dependence of the coefficient of friction showing distinct friction minima at characteristic speeds, which shifted depending on snow temperature and wetness, confirmed self-lubrication from frictional heating as a dominating process. (3) Elevated friction of fine-grained snow results from an increased real contact area which impacts dry and hydrodynamic friction. (4) The strong increase in

friction for higher speeds on wet snow strengthen the idea of a capillary drag force caused by water bridges between unloaded grains and the ski base. (5) Highest friction on wet new snow results from the concurrent increase of real contact area and interfacial water increasing both, hydrodynamic friction as well capillary drag. Besides new insight into wet snow friction processes, the data and models revealed from the snow friction field measurements provide a new quantitative tool for practitioners to predict the friction of skis and snowboards on snow of various conditions. This is supposed to improve the validity of models used to design low impact snow park jumps for ski and snowboard freestyle disciplines.

Zusammenfassung

Obwohl unter Skifahrern bekannt ist, dass die Reibung zwischen Ski und Schnee massgeblich von den Schneebedingungen beeinflusst wird und dies auch in wissenschaftlichen Studien belegt wurde, existiert bis heute kein Modell, welches die Ski-Schnee-Reibung als Funktion von messbaren Schneeparametern berechenbar macht. Dies liegt neben der Schwierigkeit die Reibung unter realen Bedingungen zu messen sowie der begrenzten Übertragbarkeit von Reibungsmessungen im Labor auch daran, dass die Prozesse im Reibkontakt zwischen Ski und Schnee noch nicht vollständig verstanden sind. Diese Arbeit verbindet darum erstmals kinematische Messungen von Ski- und Snowboardfahrern mit einer umfassenden Erfassung schneephysikalischer Parameter, mit dem Ziel Reibungskoeffizienten über einen grossen Bereich von Schneebedingungen zu ermitteln. Zudem wurden Laborexperimente durchgeführt, um die Reibungsprozesse im Übergang von trockenem zu nassem Schnee besser zu verstehen. Dabei galt der Fokus den Materialeigenschaften des Schnees und dessen Auswirkungen auf Wasserverteilung und reale Kontaktfläche an der Ski-Schnee Grenzfläche.

Trajektorien von mehr als 200 Gleitversuchen auf Ski und Snowboard wurden mittels differenziellem globalem Navigationssatellitensystem aufgezeichnet. Unter Einbezug von Windmessdaten entlang der Teststrecke sowie der im Windkanal bestimmten individuellen Aerodynamik der Athleten, wurde die Bewegungsgleichung des als Punktmasse vereinfachten Athleten nach dem Ski-Schnee Reibungskoeffizienten aufgelöst. Die so bestimmten Reibungskoeffizienten für Ski (Snowboard) lagen zwischen $0,023 \pm 0,006$ ($0,026 \pm 0,008$) und $0,139 \pm 0,018$ ($0,143 \pm 0,017$). Mit Hilfe eines multivariaten statistischen Modells wurde ein starker Zusammenhang mit den gemessenen Schneeparametern nachgewiesen ($R^2_{adj} = 0,77$). Reibungsminima der einzelnen Testläufe traten bei Geschwindigkeiten zwischen etwa 5 und 12 m s^{-1} auf und wurden massgeblich von Schneetemperatur und -feuchte beeinflusst. Um Einblicke in die Prozesse hinter der im Feldversuch quantifizierten Schneereibung zu gewinnen, wurden folgende Laborexperimente mit unterschiedlichen Schneearten durchgeführt: (1) Messung der Gleitschneereibung am Tribometer, (2) mechanische Charakterisierung von Schnee unter Kompression einschließlich (3) Kapazitätsmessungen zur Abschätzung von Wasseransammlungen an der Ski-Schnee Grenzfläche und (4) Schätzungen der gebildeten realen Kontaktfläche, abgeleitet aus hochauflösender Röntgen-Computertomographie. Die im Labor gemessenen Reibungskoeffizienten lagen zwischen $0,06 \pm 0,01$ bei trockenem, grobkörnigem Schnee und etwa $0,100 \pm 0,006$ bei nassem, feinkörnigem Schnee. Die Schneeverformung wurde von permanenten spröden und plastischen Verformungsanteilen dominiert; elastische und viskokelastische Verformungen waren hingegen klein. Anhand eines rheologischen Modells wurde zudem gezeigt, dass auf feinkörnigem Nassschnee auch viskoplastische Verformungen relevant sind. Ebenfalls auf feinkörnigem Nassschnee wurden verstärkte Wasseransammlungen an der Ski-Schnee-Grenzfläche nachgewiesen, was auf dessen grosses Wasserhaltevermögen und hohe Kompressibilität zurückgeführt wurde. Schätzungen der relativen realen Kontaktflächen lagen für die verschiedenen Schneearten zwischen 2,3 und 6 % unter Annahme einer glatten Gleitfläche. Die beschriebenen Laborresultate in Verbindung mit den gemessenen Schnee- und Geschwindigkeitsabhängigkeiten der Reibung im Feldversuch ergaben hinsichtlich

der Reibungsprozesse folgende Schlussfolgerungen: (1) Auch auf präpariertem Pistenschnee können makroskopische Verdichtung und Pflügen einen relevanten Beitrag zur Schneereibung leisten. (2) Die Geschwindigkeitsabhängigkeit des Reibungskoeffizienten sowie die systematische Verschiebung der Reibungsminima zu höheren Geschwindigkeiten bei abnehmender Schneefeuchte bzw. -temperatur, bestätigte die etablierte Annahme der Schmierung durch selbstgeneriertes Schmelzwasser als dominierenden Prozess. (3) Die erhöhte Reibung auf feinkörnigem Schnee resultiert aus einer vergrößerten realen Kontaktfläche, welche sowohl die Trockenreibungsanteile erhöht als auch die hydrodynamischen Reibungsanteile beeinflusst. (4) Der starke Anstieg der Reibung bei höheren Geschwindigkeiten auf nassem Schnee unterstützt die Annahme einer kapillaren Widerstandskraft, die durch Wasserbrücken zwischen unbelasteten Körnern und dem Skibelag verursacht wird. (5) Höchste Reibung auf nassem Neuschnee resultiert aus der gleichzeitigen Vergrößerung der realen Kontaktfläche und der Wassermenge an der Grenzfläche, was vermutlich sowohl die hydrodynamische Reibung als auch Widerstände durch Kapillarbrücken erhöht. Neben Einblicken in die Reibungsprozesse auf Nassschnee bieten die im Feld gewonnenen Daten und Modelle ein neues, quantitatives Werkzeug für Praktiker, um die Ski-Schnee-Reibung bei unterschiedlichsten Schneebedingungen zu berechnen.

Acknowledgements

I would like to thank my colleagues and superiors at SLF and KIT, as well as industrial partners, friends and my family who supported me in various ways during my doctorate:

Prof. Matthias Scherge for making this work possible and supporting me as doctorate supervisor with valuable advice, guidance and patience.

Hansueli Rhyner, Prof. Michi Lehning, Dr. Martin Schneebeli and Dr. Charles Fierz, which founded the snow sport topic at SLF, kept it alive, and acted for me as the best mentors possible. Dr. Matthias Gilgien, Dr. Fred Meyer, Dr. Henning Löwe and Dr. Denes Szabo, which gave indispensable scientific advices and discussions.

Dr. Matthias Gilgien for integrating SLF to the IOC-Slopestyle Project and setting the topic of ski-snow friction into the context of injury prevention in ski and snowboard freestyle.

Nicolas Puget, Stephane Mougin, Jacky Christoud and Angelo Maina (Rossignol S.a.r.l) for the fruitful collaboration on the applied science of the ski-snow interaction.

Ethical declaration

As parts of this study involved ski and snowboard athletes, the study was approved by the ethics committee at the Norwegian School of Sport Sciences, and the Norwegian Centre for Research Data, and conducted according to the Declaration of Helsinki. All subjects gave their written informed consent prior to participation.

Declaration of authorship

I hereby confirm that I am the sole author of the written work here enclosed and that I have compiled it in my own words, not committed any form of plagiarism, not manipulated any data, and mentioned all persons who were significant facilitators of the work. Parts excepted are corrections of form and content by supervisors, reviewers and co-authors of publications created within the framework of this thesis.

Publications

The first section of the research presented in this thesis (ski-snow friction on the real scale) was published as follows:

Wolfsperger, F., Meyer, F., Gilgien, M., 2021. The snow-friction of freestyle skis and snowboards predicted from snow physical quantities. *Frontiers in Mechanical Engineering*, 7, 728722. (18 pp.). doi: 10.3389/fmech.2021.728722.

Wolfsperger, F., Meyer, F., Gilgien, M., 2019. Towards more valid simulations of slopestyle and big air jumps: snow friction during in-run. 23rd International Congress on Snow Sport Trauma and Safety. Oral presentation held on 12th April 2019.

Further journal and conference contributions which are related in smaller parts with this thesis were published as follows:

Wolfsperger, F., Meyer, F., Gilgien, M., 2021. Towards more valid simulations of slopestyle and big air jumps: aerodynamics during in-run and flight phase. *Journal of Science and Medicine in Sport*, 24(10), 1082-1087. doi: 10.1016/j.jsams.2021.05.005.

Wolfsperger, F., Szabo, D., Rhyner, H., 2020. How to glide well on wet snow? Can roughness and hydrophobicity lower friction of polymers on snow? *Gliding* (2), 6-14.

Wolfsperger, F., Ziegler, S., Schneebeli, M., Löwe, H., 2022. Evaluation of the InfraSnow: a handheld device to measure snow specific surface (SSA). International Symposium on Snow 2022, Davos. Presented on 26th Sept.. doi: 10.13140/RG.2.2.31566.95047.

Figures presenting state-of-the art knowledge in the introduction of this thesis were used from earlier journal and book publications as follows:

Wolfsperger, F., Rhyner, H., Schneebeli, M., 2018. *Pistenpräparation und Pistenpflege. Das Handbuch für den Praktiker*. Davos, WSL-Institut für Schnee- und Lawineforschung SLF. (pp. 232).

Wolfsperger, F., Szabo, D., Rhyner, H., 2016. Development of alpine skis using FE simulations. In *Procedia Engineering* 147. Conference proceedings the engineering of sports 11, 366-371. doi: 10.1016/j.proeng.2016.06.314.

Wolfsperger, F., Rhyner, H., 2014. Mechanical and dynamical properties of racing snowboards and their modification by different binding plates. In Procedia Engineering: Vol. 72. Conference proceedings of the engineering of sport 10, 356-361. doi: 10.1016/j.proeng.2014.06.062

I hereby confirm that for all the above listed publications, I am the leading author with predominant contributions regarding all stages of the study starting with the conceptional design of the research, data processing, analysis, calculations and interpretation, as well writing and formatting. The co-authors supported the publications mainly with their conceptional consultancy, control of calculations as well as by reviewing of the manuscripts for readability, spelling and grammar. Detailed information on the use and the contributions of published content within this thesis is given at the beginning of each chapter or subchapter.

For all skiing engineers

Contents

Abstract	iii
Zusammenfassung	v
Acknowledgements	vii
Ethical declaration	viii
Declaration of authorship	viii
Publications	ix
Nomenclature	xiv
List of Figures	xviii
List of Tables	xxii
1 Introduction	1
1.1 Snow tribology	3
1.1.1 Snow and ice as sliding surface	3
1.1.2 The ski and its sliding surface	10
1.1.3 Snow and ice tribometry and modeling	11
1.2 Research questions	22
2 Methods	23
2.1 Study overview	23
2.2 Ski/Snowboard-snow friction field measurements	23
2.2.1 Research design	23
2.2.2 Data acquisition & processing	25
2.3 Slider-snow friction laboratory experiments	41
2.3.1 Research design	41
2.3.2 Snow preparation and characterization	41
2.3.3 Snow tribometry	44
2.3.4 Snow macro-mechanical characterization under compression	47
2.3.5 Snow liquid water redistribution under compression	52
2.3.6 RCA estimation and snow morphological changes	55
3 Results	58
3.1 Ski/Snowboard-snow friction field measurements	58
3.1.1 Friction coefficients for skiing and snowboarding	58
3.1.2 Parametrizations of snow friction with snow physical properties	60
3.1.3 Speed dependency of snow friction	67
3.1.4 Measurement uncertainties	68

3.2 Slider-snow friction laboratory experiments	70
3.2.1 Snow preparation	70
3.2.2 Snow tribometry	73
3.2.3 Snow macro-mechanical characterization under compression	75
3.2.4 Snow liquid water redistribution under compression	79
3.2.5 RCA estimation and snow morphological changes	82
4 Discussion	87
4.1 Ski/Snowboard-snow friction field measurements	88
4.1.1 Comparison of the results with the literature	88
4.1.2 Interpretation and limitations of the friction measured on the field	89
4.2 Laboratory experiments in the context of the found ski/snowboard-snow friction	91
4.3 Practical implications	97
5 Conclusion	98
Bibliography	100
Appendix	113
Supplementary materials - field measurements	113
Supplementary materials - laboratory experiments	121
InfraSnow development and evaluation	124
Curriculum Vitae	131

Nomenclature

α	slope (°)
Δz	ski sinkage (mm)
$\dot{\epsilon}$	strain rate (s^{-1})
ϵ	strain ($m\ m^{-1}$)
η	dynamic viscosity of water (N $m^{-2}\ s$)
η_{index}	rheological dashpot constant (N $mm^{-2}\ s$)
γ_{index}	surface energy of indexed medium (J m^{-2})
κ	curvature (m^{-1})
λ	thermal conductivity (W $m^{-1}\ K^{-1}$)
ρ_{index}	density of indexed medium (kg m^{-3})
σ	stress (N mm^{-2})
σ_c	compressive strength (N mm^{-2}) or (MPa)
τ	shear strength (N mm^{-2})
ε_{index}	measured relative permittivity of snow (-)
ε_r^{index}	relative permittivity of indexed medium (-)
a	acceleration ($m\ s^{-2}$)
A_{cntc}	contact area (mm^2)
c	specific heat capacity (J $kg^{-1}\ K^{-1}$)

$c_D A$	aerodynamic drag area (m^2)
$c_L A$	aerodynamic lift area (m^2)
CI	confidence intervall (a.u.)
COF_{index}	coefficient of friction due to indexed process (-)
COV_{index}	coefficient of variance of indexed variable (-)
D_s	coefficient of thermal diffusion ($\text{J kg}^{-1} \text{ K}^{-1}$)
E	Young's modulus or E-modulus (GPa)
E_{index}	spring constant of indexed rheological element (N mm^{-2})
F_D	aerodynamic drag force (N)
F_F	snow friction force (N)
F_{Gx}	gravity component parallel to ground (N)
F_{Gz}	gravity component normal to ground (N)
F_L	aerodynamic lift force (N)
F_N	normal force (N)
F_R	radial force (N)
F_z	vertical force (N)
g	standard acceleration due to gravity (m s^{-2})
h	water film thickness (μm)
h_{fall}	fall height of dynamic penetration mass (m)
H_{index}	surface hardness of indexed solid (MPa)
K_ρ	compression modulus (N mm^{-2})
l	ski running length (mm)

L_{wet}	length of lubricated ski (m)
LWC	liquid water content (%)
m	mass of skier (kg)
$m_{stat/dyn}$	static or dynamic penetration mass (kg)
OED	optical equivalent diameter (mm)
p_{atm}	atmospheric pressure (N m ⁻²)
p_{dyn}	dynamic air pressure (N m ⁻²)
PR	penetration resistance of snow (N)
Q_L	latent heat of fusion of ice (kJ kg ⁻¹)
R_z	average maximum profile height (μm)
R_{adj}^2	adjusted coefficient of determination (-)
R_a	average roughness (μm)
r_c	contact spot radius (mm)
R_h	gas constant for humid air (kg ⁻¹ K ⁻¹)
R_{sk}	roughness profile skewness (μm)
R_{sm}	mean width of roughness profile elements (μm)
RCA	real contact area (mm ²)
RCA_{rel}	relative real contact area (%)
RH	relative air humidity (%)
s_{dyn}	penetration depth of penetrometer (m)
s_{index}	snow deformation of indexed mode (mm)
s_x	skier's distance travelled in x-direction (m)

<i>sd</i>	standard deviation (a.u)
<i>SSA</i>	specific surface area ($\text{mm}^2 \text{ mm}^{-3}$)
<i>T_h</i>	homologous temperature (K)
<i>T_{index}</i>	temperature of indexed medium (°C)
<i>T_{melt}</i>	melting temperature (°C) or (K)
<i>v</i>	speed (m s^{-1})
<i>v_{rel}</i>	relative airflow speed (m s^{-1})
<i>w_{def}</i>	snow deformation work (mJ)
<i>w_{slider}</i>	ski width at tip (mm)
CC	cross country
PTFE	polytetrafluoroethylene
SB	Snowboard
SLF	WSL-Institute for Snow and Avalanche Research SLF
UHMWPE	ultra-high molecular weight polyethylene

List of Figures

1.1	Left) Three-dimensional image of typical round-grained snow with a density of 248 kg m ⁻³ which equals a porosity of 0.73. The gray 3D structures represent the ice framework, consisting of coalesced (sintered) monocrystalline ice interspersed with air-filled pores. The ice framework and pores are both contiguous (from Wolfsperger et al., 2018; with authorization of the WSL-Institue for Snow and Avalanche Research SLF). Right) Three-dimensional image of snow (ca. 3 × 3 × 3 mm) visualizing interconnected monocrystalline snow grains. The change in color estimates the crystallographic grain boundaries (unpublished Figure from Theile and Schneebeli, 2011, printed with their authorization).	4
1.2	Examples of the different snow types based on microscopic images (image field 4.3 x 3.2 mm) and, classified according to Fierz et al., (2009): (top left) Precipitation particles, (top right) small rounded grains, (bottom left) faceted crystals, and (bottom right) machine-made snow (reprinted from Wolfsperger et al., 2018, with authorization of the SLF).	5
1.3	Homologous temperature and water pressure of ice (calculated from Wagner et al., 1994) versus temperature.	6
1.4	Cross-section of a sandwich construction of a slalom ski consisting of the polyamide top sheet, several epoxy/fleece gluing layers, upper structural layers (glass fiber, aluminum alloy), elastomer, the polyurethane core, sidewalls, lower structural layers, steel edges and a polyethylene base (unpublished Figure from Wolfsperger et al., 2016, printed with their authorization).	10
1.5	Exemplary force distribution underneath a racing snowboard on a 2 mm elastomer used as snow replicate measured on a laboratory device at SLF (unpublished data from Wolfsperger et al., 2014, printed with their authorization).	12
1.6	Left) 3D surface topography of stone grinded ski base as revealed from white light interferometry. Right) Extracted 2D roughness profile along the marked blue line with values for $R_a = 3.7 \mu\text{m}$ (average roughness) and $R_z = 18.9 \mu\text{m}$ (average maximum profile height) (SLF, 2012, printed with authorization).	12
1.7	Contributions to the ski-snow friction adapted and reprinted from Colbeck (1988), showing the total friction coefficient COF , dry friction coefficient COF_{dry} , lubricated friction coefficient COF_{hydro} , and the friction coefficient due to capillary forces COF_{cap} versus water film thickness for a contact spot diameter of 2 mm and a velocity of 10 m s ⁻¹	19

2.1	Overview and interlinks of the study's components. Red question marks denote the major research questions.	24
2.2	Location of the gliding tracks (red arrows) at Weissfluhjoch (a) and Bolgen (b) (© swisstopo, 2021).	25
2.3	Gliding tracks at Davos Weissfluhjoch (a) and Bolgen (b) with a skier and a snowboarder holding the defined mid-extended posture. Side view photographs of this posture were shown in (Wolfsperger et al., 2021).	26
2.4	Skier during wind tunnel measurements to reveal the individual speed-dependent functions of the aerodynamic drag and lift.	27
2.5	Speed dependent functions of the drag area (top) and lift area (bottom) of the test skiers (left) and snowboarders (right) holding the inrun-posture as shown in Fig. 2.4.	28
2.6	Free body diagram visualizing the forces acting on an athlete during a test run. The curvature of the terrain is not visualized.	30
2.7	Instruments used to measure the snow properties: InfraSnow (top left), Dielectric sensors for <i>LWC</i> measurements (top right) and density (bottom left), and the adapted Swiss Rammsonde (bottom right).	35
2.8	Fine-grained snow samples after a series of compression experiments.	42
2.9	Linear friction tester with the mounted UHMWPE slider. The mounted pink strap was not used for compression or friction tests (see chapter 4).	45
2.10	Left) Sketch of the laboratory setup for friction and compression tests. Right) A broken snow sample after a friction test.	45
2.11	Exemplarily COF-curve of a single snow friction measurement starting with a distinct peak (static friction), followed by oscillations on a constant level (kinetic friction) until the snow sample partly collapsed. The coefficient of kinetic friction was calculated as average between the green lines. The oscillations were assumably a result of the strong starting acceleration.	46
2.12	Two fine-grained snow samples after a compression test.	48
2.13	Force-displacement raw signals of the compression of dry and wet FG, MG and CG snow samples.	48
2.14	Top) Measured force and distance of two consecutive compression tests of a wet (<i>LWC</i> = 7 %) fine-grained snow sample including loading and unloading. Middle) Calculated compression module of the first compression experiment, which was averaged throughout the linear section of the force curve marked by the green vertical lines. Bottom) Stress σ , strain and its fit (Burger model) during the period of constant stress of the first compression test.	50
2.15	Setup of compression tests of snow samples using a co-planar capacitive sensor to monitor of liquid water accumulation at the slider-snow interface.	52
2.16	Permittivity measurements (dashed, magenta) and compression force (red) over compression distance of fine-grained (FG) dry (top left) and wet snow with increasing <i>LWC</i> (top right to bottom left). The vertical lines in green mark the height at initial sensor-snow contact and at full compression. Corresponding graphs for mid and coarse-grained snow can be found in the appendix.	54

2.17 Comparison of two snow sample sub-volumes (ca. $9 \times 9 \times 0.9$ mm) before (left) and after (right) the slider contact visualized as 3D surface mesh models. Due to the slider contact, the sample surface on the left side is more equally leveled and has more flat surface features within the same horizontal plane.	55
2.18 Frequencies of flat (horizontal) surface elements along the depth of the meshed snow sample microstructure 3D representation revealed from μ CT-scans.	56
3.1 COF (mean \pm sd) of consecutive snowboard runs throughout a test day (ca. 9:00 to 15:00) on spring snow (18/04/08), and on groomed new snow (18/03/28) with increasing LWC from 0 % to ca. 10 %. The consecutive numbering of the runs also includes runs performed by skiers which are not plotted.	59
3.2 Mean (\pm sd) friction coefficients of all analyzed ($n = 114$) ski runs plotted versus the corresponding approximated snow properties (\pm RMSE) at the time of each run. Fitted curves represent single snow parameter models specified in the methods.	62
3.3 Mean (\pm sd) friction coefficients of all analyzed ($n = 100$) snowboard runs plotted versus the corresponding approximated snow properties (\pm RMSE) at the time of each run. Fitted curves represent single snow parameter models specified in the methods.	63
3.4 COF contour maps of skiers (a to c) and snowboarders (d to f) visualizing multivariate models of the COF -snow property relationship for low (top), mid and high (bottom) PR . The measured COF -values are visualized by small black dots revolved by larger filled circles (= 1 run). If the measurement (filled circle) has the same value (color) as the model (background), only the small black dot is visible.	66
3.5 Mean COF -speed curves with error bands (\pm sd) and vertical lines to mark COF_{start} and COF_{min} for six snow categories: a) Skis on frozen spring snow ($n = 4$). b) Skis on very wet spring snow ($n = 4$). c) Skis on winter snow ($n = 3$). d) Skis on cold winter snow ($n = 5$). e) Snowboard on dry new snow ($n = 5$). f) Snowboard on very wet new snow ($n = 2$).	69
3.6 a) Five consecutive runs of skier S1 on cold winter snow (18-02-13) with calm air ($v_{wind} = 0.1 \pm 0.7$ m s^{-1} , $COF = 0.059 \pm 0.001$). b) Five consecutive runs of skier S4 on warm winter snow (18-03-04) with a light breeze ($v_{wind} = 2.2 \pm 1.1$ m s^{-1} , $COF = 0.054 \pm 0.006$).	70
3.7 The different groups of snow samples and the reproducibility of sample preparation showed by the averages and variation of their density (mean \pm sd).	71
3.8 9 by 9 mm crop of the top 0.9 mm of a fine-grained snow sample (FG2mm) in dry state.	72
3.9 9 by 9 mm crop of the top 0.9 mm of a mid-grained snow sample (MG1mm) in dry state.	72
3.10 9 by 9 mm crop of the top 2.7 mm of a coarse-grained snow sample (CG1mm) refrozen after having a LWC of 5.9 %.	73

3.11 Kinetic friction coefficients (COF_{kin}) of a UHMWPE slider on fine, mid and coarse-grained snow in dry and various wet states with liquid water contents from about 2 % to 15 %.	74
3.12 Deformation work of fine, mid, and coarse-grained snow in dry and various wet states with liquid water contents from about 2 to 15 %.	75
3.13 Permanent brittle and plastic (left), elastic (middle), and viscoelastic deformation fractions of fine, mid and coarse-grained snow in dry and various wet states with liquid water contents from about 2 to 15 %.	76
3.14 Compression module of fine, mid, and coarse-grained snow in dry and various wet states with liquid water contents from about 2 to 15 %.	77
3.15 Parameter of the burger model fitted to the strains under constant stress loading of fine, mid, and coarse-grained snow in dry and various wet states with liquid water contents from about 2 to 15 %. Left) Dashpot constant representing viscoplastic deformations. Right) Relaxation time (η_{KV}/E_{KV}) representing the viscoelastic deformations.	78
3.16 Increase of relative permittivity of snow from dry to wet state vs. overall LWC at the initial contact of sensor and snow (lower values), and at full load (connected higher values). The overall LWC were revealed from calorimetry measurements of the complete snow samples.	80
3.17 Left) Increase of the relative permittivity of snow from the initial snow-sensor contact until full load was reached vs. the overall LWC . Right) Increase of the relative permittivity of snow from the initial snow-sensor contact until full load was reached vs. the corresponding snow deformation. The marker size corresponds to the overall LWC , which were revealed from calorimetry measurements of the complete snow samples.	81
3.18 Density profiles of the snow samples before (pre) and after (post) the compression experiments.	83
3.19 Estimated RCA_{rel} of five snow samples after compressive contact with a slider deduced from the samples' flat surface features as revealed from μ CT-scans. From each snow sample four equally sized sub-volumes were used to deduce the RCA-values.	84
3.20 Surface topography and contact spots (black) of a coarse-grained snow sample after compressive contact. Left) Snow with a LWC of 5.9 % and a deduced RCA_{rel} of 3.4 %. Right) Snow with a LWC of 14.6 % and a RCA_{rel} of 3.5 %.	85
3.21 Surface topography and contact spots (black) of a mid-grained snow sample after compressive contact. Left) Snow in dry state with a deduced RCA_{rel} of 3.6 %. Right) Snow with a LWC of 4.5 % and an RCA_{rel} of 3.7 %.	85
3.22 Surface topography and contact spots (black) of two fine-grained snow samples after compressive contact. The snow samples had overall LWC of about 7 % and RCA_{rel} of 6 % (left), and 4.6 % (right).	86

List of Tables

2.1	Properties of the test skis and snowboard including surface roughness parameters ($n = 10$) and dynamic contact angles of distilled water ($n = 8$). The advancing (receding) angle is the contact angle which occurs in the course of wetting (de-wetting) of the ski base.	26
2.2	Weather description and average (mean $\pm sd$) weather parameters during the captured runs of each test day (date).	32
2.3	Snow conditions on each test day: Colloquially described, classified after Fierz et al. (2009), and quantified by the daily range ($TLWC$) or mean ($\pm sd$) of the measured snow physical properties. HN24 (HN72) describes the height of fallen new snow during the past 24 (72) hours.	36
2.4	Values and explanations of the assumed uncertainties of the measured and deduced input quantities.	40
2.5	Properties of the UHMWPE slider including surface roughness parameters ($n = 5$) and dynamic contact angles of distilled water ($n = 7$). The advancing (receding) angle is the contact angle which occurs in the course of wetting (de-wetting) of the ski base.	46
3.1	Friction coefficients averaged over 2 to 6 consecutive runs with constant snow conditions, categorized into spring, winter and new snow with different snow temperature or snow wetness sub-categories. The overall COF (mean $\pm sd$) were averaged from 5 to 15 $m s^{-1}$. Instantaneous COF -values at the start (after 4 m of gliding; COF_{start}), when reaching the minimum COF (COF_{min}), at 10 $m s^{-1}$ (COF_{10}), 15 $m s^{-1}$ (COF_{15}) and at maximum speed (COF_{vmax}), provide information on the COF -speed dependency.	61
3.2	Density and SSA of the prepared samples measured with different methods.	71

1 Introduction

*The paragraphs 3, 4 and 5 of the following chapter are parts of the publication: Wolfsperger, F., Meyer, F., Gilgien, M., 2021. The snow-friction of freestyle skis and snowboards predicted from snow physical quantities. *Frontiers in Mechanical Engineering*, 7, 728722.*

Skiing has a long history starting several thousand years ago (Finstad et al., 2018). Until today the original function of skis as a mode of travel over snow is still common (Nansen, 1891). However, since skiing was started to be understood as a joyful activity without any teleological purpose, and as a sport, its rapid development started in the late 19th century to what it is today – a mass sport embedded in global tourism and substantial industries. As typically for most sports, also in skiing a considerable body of research was built-up since the middle of the 20th century, which came along with growing professionalism and commercialization of the sport (Taylor, 2015). However, skiing is past its best, suffering from stagnating popularity and reputational damage due to non-sustainable major sport events like the Olympics (Eberts, 2014; Koerkamp, 2014), as well as pollution and health hazards from fluorinated waxes (Carlson and Tupper, 2020). In addition, climate warming substantially threatens the natural snow reliability of ski areas in the future (Marty et al., 2017). Although snow making can well compensate the natural scarcity of snow during the next three decades, it is expected to reach its limits within the second half of this century (Spandre et al., 2019). This indicates that skiing, and winter sports in general, including its related industries, organizations and sciences, have to align their activities to new requirements resulting from changing boundary conditions. A good example is the current research effort to replace fluorinated waxes with eco-friendly substances aiming to provide good gliding on wet snow conditions, which must be expected more frequently with ongoing climate warming.

Regarding the science of skiing, its major fields mirror the components which underlie a skiers outcoming performance. It is dominated by the athlete, which is subject to sport science and medicine, the equipment, which is subject to engineering sciences, and the playing field which is subject to snow science and meteorology. This multidisciplinarity and the interaction of the different components is a huge challenge when aiming to understand their contributions to an outcoming performance of a skier competing a race. Assuming the skier as a static load in a straight-down run reduces the systems' complexity to the interaction of the ski and the snow surrounded by the given atmospheric conditions. In engineering sciences, this can be described as a tribological system consisting of two contact bodies in relative sliding motion, dissipating energy during the transfer of potential energy into kinetic energy. As every tribosystem, also the ski-snow friction can be strongly modified by the lubricant between the contacting bodies and by the surrounding media. Particular for a tribosystem including ice or snow as

contact body is the strong interdependence between the lubricant (water), the surrounding atmosphere and the snow or ice surface. On the one hand, the lubricant can be generated due to melting by frictional heating within the gliding process. On the other hand, water can be released to the ski-snow interface from the snow by melting due to energy input from the atmosphere. Besides winter sports disciplines, this complex tribological interplay governs several other technical applications in cold environments (e.g. winter tyres, snow blowers, icebreakers). To investigate such systems, methods and knowledge from both field, tribology and snow science are needed to be applied. Moreover, to measure the friction on snow in real skiing scenarios, kinematical and dynamical aspects needs to be included to separate the snow friction force from the air drag and the gravitational forces, which are typically in the scope of sport biomechanics.

Ski-snow friction, air drag and gravity are the three forces that regulate speed in skiing. The acceleration due to gravity is dependent on the incline of the slope, while air drag is a function of speed, frontal area, the shape and material properties of the athlete's clothing, and air density. The most complex force that acts on skiers is the ski-snow friction force. Its underlying mechanisms and their contribution to the frictional resistance of a ski on snow are still controversial (Bowden and Hughes, 1939; Colbeck, 1992; Bäuerle, 2006; Böttcher et al., 2017; Canale et al., 2019; Lever et al., 2021; Scherge et al., 2021). A major challenge within the science of snow friction is to isolate the processes between contact mechanics (dry friction) and fluid dynamics (lubricated friction) which interact thermodynamically at the interface. A key factor within this interaction is the complex material behavior of snow during deformation depending on the strain rate and its various material properties. The material properties of snow vary considerably as a result of differing porosity, proximity to the melting point (high homologous temperature), and markedly different microstructures and degrees of sintering. In consequence, the level of ski-snow friction and the governing mechanisms can change distinctly, as the material properties of the snow change (Nachbauer et al., 1996; Buhl et al., 2001; Fauve et al. 2005). In addition, the snow's physical instability facilitates rapid changes in properties (Szabo and Schneebeli, 2007), and hence increases the difficulty of describing the mechanics of the frictional contact between snow and ski. Moreover, the lack of appropriate measurement devices to quantify snow physical properties on the field makes it difficult to access the data necessary to investigate the relationship of ski-snow friction and snow properties. For those several reasons, the coefficient of friction (*COF*) of a skier, although repeatedly measured (Kaps et al., 1996; Habel, 1968; Kuroiwa, 1977; Leino and Spring, 1984; Kaps et al., 1996), could so far not been well predicted for a given snow condition. In particular, this concerns the friction on snow at its melting point and has been aggravated, as the unification of available ski-snow friction data has mostly been impossible due to the limited comparability of snow friction measurement methods or missing information of the physio-chemical characteristics (wax and topography) of the gliding surfaces of the skis.

Therefore, this study focused the snow's influence on the ski-snow friction, first, aiming to quantify the snow friction of real skis and snowboards in a consistent and comparable manner for a comprehensive snow parameter space, which sufficiently represents the range of snow conditions occurring on ski slopes. This required to measure a set of snow quantities on

the field, as well as to apply sport biomechanical methods, as well as real scale wind tunnel experiments, to access the snow friction force of a skier in a real skiing scenario to finally reveal a well-determined and valid *COF* parametrization. And second, based on those findings on the real scale, laboratory experiments aimed to improve the understanding of the interactions between the physical properties of snow, the snow deformation and the resulting frictional contact and friction force. To realize that a short distance snow tribometer was used and combined with newly developed snow preparation and analyzation methods.

Besides narrowing down existing knowledge gaps in the field of snow tribology, this research was additionally motivated by an application-oriented problem in the field of sports: Severe injuries of freestyle skiers and snowboarders on snow park jumps typically occur if athletes miss the inclined landing zone when jumping too short or too far (Florenes et al., 2010; Henrie et al., 2010; Florenes et al., 2011; Bianchi et al., 2016; Soligard et al., 2019). The engineering solution to reduce the probability of those injuries provoking events addresses the improvement of the jump design by optimized landing geometries to minimize landing impacts (Shealy and Stone, 2008; Levy et al., 2015; Heer et al., 2019; Schindelwig et al., 2019). This includes the use of models calculating the kinematics and kinetics of athletes from the in-run to the landing of a jump to evaluate the safety of new jump geometries. Although remarkable research studies on jump design are available (McNeil et al., 2012; M., 2015), the modeling of jumps still has considerable uncertainties with respect to the validity of snow friction coefficients and aerodynamic drag and lift for ski and snowboard (SB) freestyle athletes. Obviously, a precise quantification of the *COF* depending on the snow conditions is needed to calculate the take-off speed, and so the jump distance, precisely. Moreover, the energy dissipation due to snow deformation at the landing impact is to be considered when calculating landing kinetics of snow park jumps. For both aspects, the friction during the in-run and the impact at the landing, the snow physical properties have determining influence. Therefore, this research study was also motivated to provide the missing data for more valid simulations of the kinematics and kinetics of snow park jumps, helping to design safer snow park jumps.

1.1 Snow tribology

1.1.1 Snow and ice as sliding surface

The following subchapter includes two figures (1.1 left; 1.2) from the book: Wolfsperger, F., Rhyner, H., Schneebeli, M., 2018. Pistenpräparation und Pistenpflege. Das Handbuch für den Praktiker. Davos, WSL-Institut für Schnee- und Lawineforschung SLF. (pp. 232).

Ice, as occurring under natural atmospheric conditions, is the solid phase of water, where H_2O molecules arrange in a hexagonal lattice due to the water molecule's affinity of building hydrogen bonds. Ice is a transparent, usually polycrystalline material and is obtained from freezing water or condenses from vapor forming single crystals with a variety of shapes, e.g.

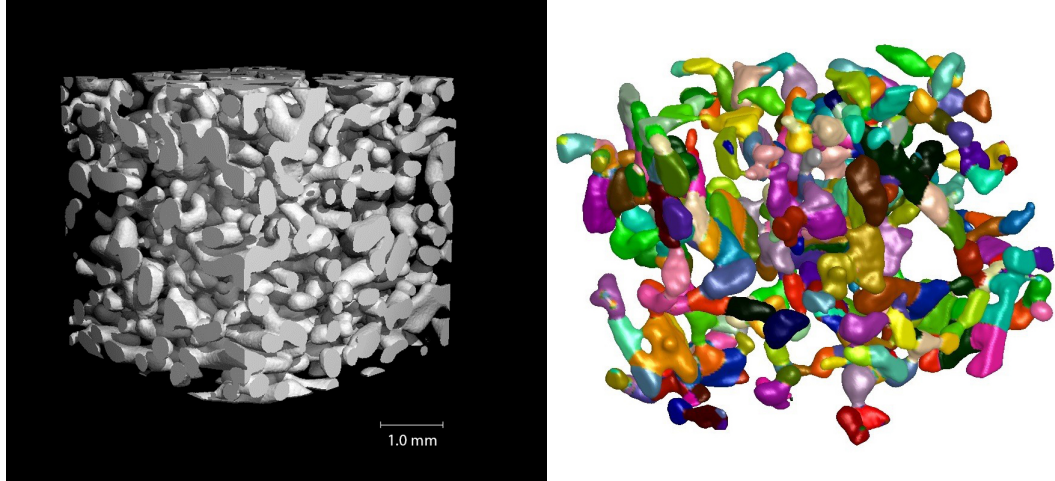


Figure 1.1: Left) Three-dimensional image of typical round-grained snow with a density of 248 kg m^{-3} which equals a porosity of 0.73. The gray 3D structures represent the ice framework, consisting of coalesced (sintered) monocrystalline ice interspersed with air-filled pores. The ice framework and pores are both contiguous (from Wolfsperger et al., 2018; with authorization of the WSL-Institue for Snow and Avalanche Research SLF). Right) Three-dimensional image of snow (ca. $3 \times 3 \times 3 \text{ mm}$) visualizing interconnected monocrystalline snow grains. The change in color estimates the crystallographic grain boundaries (unpublished Figure from Theile and Schneebeli, 2011, printed with their authorization).

dendrites, platelets, or needles, which are known as snow crystals revealing the hexagonal symmetry of the crystal lattice of ice (Petrenko and Whitworth, 2002). As soon as snow reaches the ground, it undergoes morphological changes, known as snow metamorphism (Bader, 1954; Kämpfer and Schneebeli, 2007), where single hexagonal snow crystals transform to a connected matrix of consolidated, less filigree snow grains (Fig. 1.1 left; Fig. 1.2). Natural snow can therefore be considered as a porous material of sintered ice monocrystals as shown by Theile and Schneebeli (2011) (Fig. 1.1 right). Because of its strong and quick morphological changes, snow exhibits a wide range of physical properties, e.g. density, which can range from 50 up to 830 kg m^{-3} from whereon it is called (porous) ice (Wolfsperger et al., 2018).

There are mainly two factors which, on the one hand, drive metamorphism processes revealing the snow's versatile and vivid character, and, on the other hand, contribute to the unique mechanics of ice as the constitutive material of snow: First, the warm nature of ice and snow, as they occur on earth only at high homologous temperatures $T_h = T[K]/T_{melt}[K]$. For skiing, T_h mostly exceeds values of about 0.9, which is equivalent to -26°C (Fig. 1.3). And second, the high vapor pressure of ice. Both aspects make snow and ice a rather unstable material whose physical properties can rapidly change with small changes of ambient conditions. For example, the compressive strength of ice almost doubles when dropping the temperature from 0 to -10°C (Petrovic, 2003). This makes it difficult to capture the properties

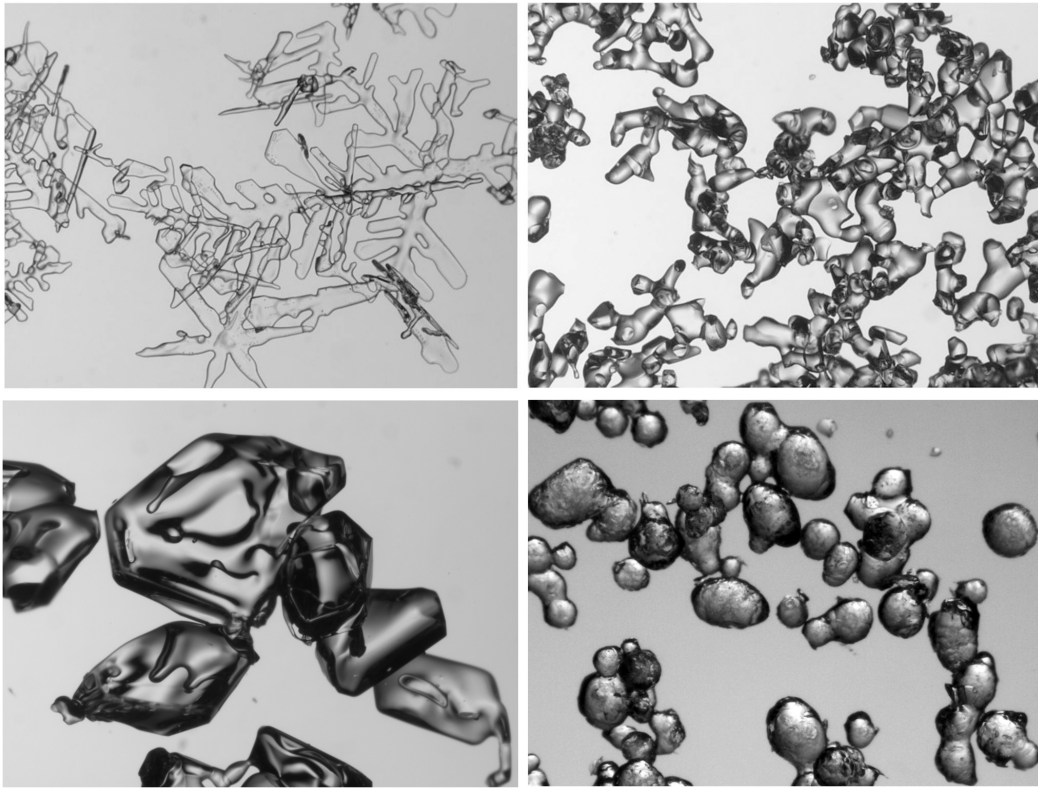


Figure 1.2: Examples of the different snow types based on microscopic images (image field 4.3 x 3.2 mm) and, classified according to Fierz et al., (2009): (top left) Precipitation particles, (top right) small rounded grains, (bottom left) faceted crystals, and (bottom right) machine-made snow (reprinted from Wolfsperger et al., 2018, with authorization of the SLF).

of ice and snow in a way that correctly represents their actual state during a tribological experiment. Moreover, the frictional processes itself are affected by these inherent mechanical and thermodynamical fragilities.

The high vapor pressure of ice for highest homologous temperatures indicates, that the surface of ice has properties distinctively different from the bulk, which was referred to as a quasi-liquid-layer (Petrenko and Whitworth, 2002). It is not ice specific, that surfaces of a solid have different properties compared to the bulk, as atoms or molecules at a free surface only experience bonding forces to other molecules from one side. However, for ice, these surface properties extend to lower temperatures and to greater depth (Petrenko, 1994). Lever et al. (2021) summarized model and measurement-based insights from the last two decades showing large variations in quasi-liquid-layer thickness versus temperature starting from a few nanometers near -40 °C to tens of nanometers near 0 °C (Döppenschmidt and Butt, 2000; Pittenger et al., 2001; Rosenberg, 2005; Li and Somorjai, 2007; Slater and Michaelides,

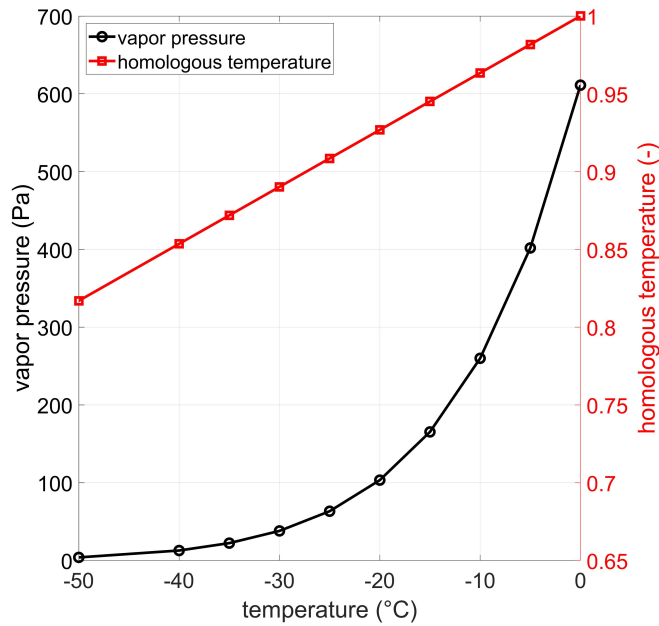


Figure 1.3: Homologous temperature and water pressure of ice (calculated from Wagner et al., 1994) versus temperature.

2019). This confirmed earlier measurements showing maximal thicknesses of 50 nm at an ice temperature of $-0.3\text{ }^{\circ}\text{C}$ (Dosch et al., 1995). Whereas there is consensus on the existence of a quasi-liquid-layer, its relevance concerning the ski-snow friction is under debate. Plausibly, a reduced shear strength of the ice surface could explain low dry friction if the slider asperities interact only to the depth of the quasi-liquid-layer, not reaching bulk material (see chapter 1.1.3). Especially at lowest speeds and paired with a reported velocity-independence, this is convincing (Nagata et al., 2019). However, other frictional processes related to higher, ski-relevant speeds, might be more important (see chapter 1.1.3). Besides direct effects of the quasi-liquid-layer on friction processes, nano- and microscale surface properties influence macro-mechanical properties of snow, e.g. the process of snow sintering (Willibald et al., 2021), and therefore the snow strength. Beyond that, as snow sintering was reported to be astonishing fast (Szabo and Schneebeli, 2007), it might play a more active role for the ski-snow friction than widely assumed.

Regarding larger scaled morphological properties, the surface topography of snow and ice, manifesting on the micro- to the macroscale, is of high interest. For tribological surfaces this is referred to as surface roughness. Bäuerle (2006) used optical profilometry to measure the roughness of ice surfaces (2D profiles perpendicular to the direction of motion) before and after sliding experiments revealing R_z -values (average maximum profile height) of $0.5\text{ }\mu\text{m}$ and $1.8\text{ }\mu\text{m}$, respectively. Not surprisingly, low roughness was found on the undisturbed ice surface expressing the typical smoothness of ice where the largest features in the roughness profiles

originated from the grooves of ice grain bonds. Typically for tribological measurements on ice was the distinct change of surface topography towards the roughness of the slider after several runs. Similar as for ice, also for snow the pre- and post-state of the surface is of interest. However, this was seldom reported in the literature. Recently, Hasler et al. (2022) deduced the surface roughness of compacted machine-made snow ($\rho_s = 440 \text{ kg m}^{-3}$) before and after several passes with a cross country ski at temperatures between -19 and -1 °C from x-ray micro computed tomography (μCT). The average surface roughness before the first run was between 163 and 168 μm , decreasing after the first run to about 30 to 50 μm . Interestingly, on cold snow the surface roughness increased again for the following runs to about 80 μm . Whereas, for mid and warm snow temperatures, the roughness further decreased. Whereas for ice, the microscopic surface is well determined due to a sharp and solid interface with the surrounding medium, for snow, this transition is blurred due to its large surface roughness, which continues as porosity and microstructure when virtually penetrating deeper into the material. The snow microstructure describes the geometry of the snow grains interlinked in the ice matrix (see chapter 2.2.2.4). The snow surface in the frictional contact with a ski, must therefore be considered over a certain surface-near volume. This is especially important when snow becomes wet, containing varying amounts of liquid water (Fierz et al., 2009).

Besides morphological properties of surface and material, the mechanical properties of snow and ice must be known to describe the contact with a ski. Whereas the mechanical properties of ice are determined by temperature, grain size and strain rate (Petrenko and Whitworth, 2002), for snow, density, microstructure, and the degree of sintering has to be considered, too (Shapiro et al., 1997). Polycrystalline ice and most snow types have anisotropic mechanical properties and stiffen and strengthen with increasing strain rate and decreasing temperature. Strain rates occurring during the ski-snow/ice contact were assumed to be larger than 10^{-2} s^{-1} , which is above the brittle-to-ductile transition of ice ($< 5 \cdot 10^{-4} \text{ s}^{-1}$) and snow ($< 5 \cdot 10^{-3} \text{ s}^{-1}$) at -10 °C (Batto and Schulson, 1993; Löwe et al., 2020). Fukue (1979) found the critical deformation rate between ductile and brittle behavior for high density snow to decrease with increasing of σ_c and assumed microstructure and temperature to further influence the critical rate. Values ranged between 0.1 and 0.3 mm s^{-1} , confirming the dominating brittle regime of snow deformation underneath a ski ($> 0.7 \text{ mm s}^{-1}$; assuming a ski of 1.5 m with 1 m s^{-1} penetrating 0.5 mm). Considering loading times at the ski-snow contact, the short duration of consecutive microscopic contacts of asperities with the rough ski base needs to be distinguished from the relatively long time of loading of a macroscopic volume of snow. However, assumable the latter might influence the number of micro contacts, and for wet snow the contact lubrication (see chapter 1.1.3). Their rate-dependence makes snow and ice complex materials responding on load with elastic, viscoelastic, plastic and viscoplastic deformation or brittle yield. Whereas for ice, the rate-dependent plasticity is described by Glen's Law and explained by dynamics of dislocations in the ice lattice (Schulson, 2009), for snow, this is still an object under investigation. Plastic deformation (creep) was currently related with snow's microstructure, quantified by the optical equivalent diameter OED , identifying a sharp transition of OED (0.5 to 0.6 mm) from where on plastic flow distinctively drops (Sundu et al., 2023) as grain bond gliding becomes less dominant. For higher strain rates, when grain bonds start to yield (brittle), rapid sintering of grains act as a self-healing mechanism against

macroscopic snow failure, which stretches the ductile-to-brittle transition to larger strain rates (Löwe et al., 2020). As snow sintering fastens with increasing temperature (Blackford, 2007), ductile behavior expands to higher strain rates for snow near the melting point (Kinosita, 1967; Wang et al., 2021). Compared to the current state of knowledge of dry snow deformations, there is less known on the mechanics of wet snow deformation as “*experiments are difficult to control and a theory has to involve, in addition to the dry snow processes, complex surface phenomena in the three-phases system*” (Salm, 1982). Wakahama (1968; 1975) first investigated the phenomena of wet snow deformation and metamorphism. The latter was described as grain growth and reduction of size and number of grain bonds, which was later explained by liquid phase sintering (Armstrong and Brun, 2008). Whereas deformations were explained with grain bond gliding until closest packing, followed by a second phase with large plastic deformations of grains and growing bonds until snow turned into porous ice. Colbeck and Parssinen (1978) conducted further compression experiments under constant stress and low strain rates and described the processes of wet snow compression in terms of pressure melting and plastic deformations at grain contacts considering effects, e.g. of grain size and capillary pressure. Up to date, the mechanical properties of wet snow and the underlying mechanisms are not fully understood, especially the case for ski specific conditions of rapid loads (Zwimpfer et al., 2011; Mitterer and Schweizer, 2014).

For polycrystalline ice, the Young's modulus E lays in a confined range from about 9 to 11 GPa (Petrenko and Whitworth, 2002; Petrovic, 2003). Instead for snow, a wide range from 0.3 to 0.8 GPa for densities between 400 and 500 kg m⁻³ at temperatures between -10 and -20 °C was reported (e.g. Mellor, 1975; Gerling et al., 2017). Not much is known how the Young's modulus of snow changes at the melting point. Mellor (1975) reported a reduction by about 20 % from -10 °C to 0 °C.

The compressive strength σ_c of ice at high strain rates (10⁻² s⁻¹) increased from 5 MPa at the melting point to about 35 MPa at -50 °C (Haynes, 1978). For snow, σ_c ranges even wider. Lintzen et al. (2014) found the (unconfined) σ_c of machine-made snow at -10 °C at high strain rates (2.5·10⁻³ to 5·10⁻³ or 0.3 to 0.6 mm s⁻¹) within a rather narrow range of 1.6 ± 0.2 MPa (510 to 550 kg m⁻³). However, old and coarsened machine-made snow largely scattered between 0.2 and 1.3 MPa, although its density was higher (550 to 700 kg m⁻³). The order of magnitude of Lintzen's data matched well with the ones summarized by Mellor (1975), who found values of 0.1 MPa at 400 kg m⁻³ to about 1 MPa at 600 kg m⁻³. However, Lintzen et al. (2014) exemplarily showed, that density does not necessarily explain σ_c of snow if its microstructure is not taken into account. Recent compression experiments over a wide range of deformation rates (0.02 to 5 mm s⁻¹), densities (350 to 600 kg m⁻³) and temperatures (-5 to -25 °C) showed, that the σ_c peaks for loading rates around 0.3 mm s⁻¹ at the ductile-to-brittle transition, followed by a distinct decrease for faster loading (Wang et al., 2021). At -25 °C σ_c dropped from a peak of 1.1 to 0.4 MPa, and from 0.8 to 0.2 MPa at -5 °C ($\rho_s = 500$ kg m⁻³).

The surface hardness of a material, understood as the resistance against indentation, is a crucial tribological parameter affecting the interaction of microscopic contacts between two

bodies, and is usually related to the plastic properties of ductile materials (Popov, 2015). The hardness is typically measured by the force required to press a small (< 1 mm) indenter into a surface, divided by the imprinted (projected) area, or depth of indentation (Beitz and Grote, 2001). The hardness of ice H_{ice} decreases with increasing temperature and loading time ranging from 15 MPa at 0 °C to about 60 MPa at -10 °C when shortly loaded (10^{-4} s), and from 15 to 40 MPa for a loading time of 1.5 s (Barnes et al., 1971). More recent measurements revealed ice hardness between 15 and 21 MPa for the same temperature range (Poirier et al., 2011). As shown by Böttcher et al. (2017), the temperature dependence of the hardness of ice and of the ski base material can be crucial for the ski-snow friction if their hardness-temperature curves cross within the relevant temperature for skiing. In contrast to typical hardness measurements with long loading times, dynamic ice hardness measurement as cited above were shown to involve brittle failure of the ice (Poirier et al., 2011). Similar as for ice, the snow hardness is the resistance against penetration of an object into snow revealing a quasi-objective, instrument dependent, hardness value in Newton (see chapter, 2.2.2.4, Fierz et al., 2009). The indenter and the snow interact on a larger scale of several centimeters and the measurement provides no additional information related to processes of the ski-snow friction compared to what is revealed from the compression strength of snow. However, as it is a field-ready method it can serve as an estimate of snow strength or snow density.

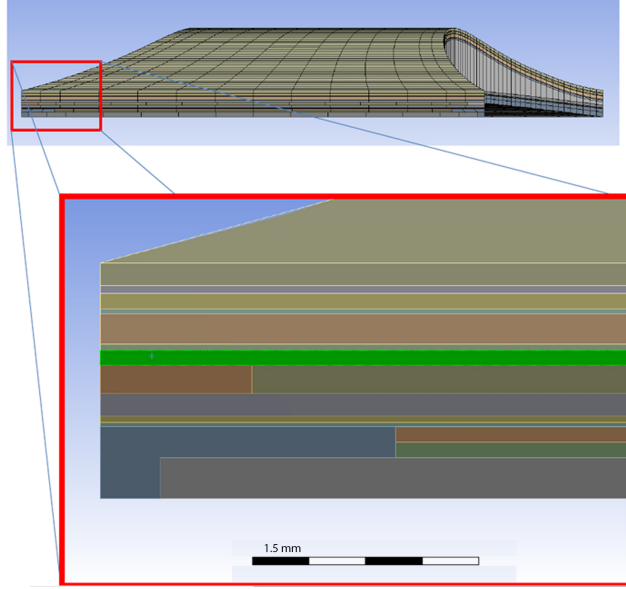


Figure 1.4: Cross-section of a sandwich construction of a slalom ski consisting of the polyamide top sheet, several epoxy/fleece gluing layers, upper structural layers (glass fiber, aluminum alloy), elastomer, the polyurethane core, sidewalls, lower structural layers, steel edges and a polyethylene base (unpublished Figure from Wolfsperger et al., 2016, printed with their authorization).

1.1.2 The ski and its sliding surface

The following subchapter includes two Figures generated from data from two earlier publications (Fig. 1.4 and 1.5): Wolfsperger, F., Szabo, D., Rhyner, H., 2016. Development of alpine skis using FE simulations. In Procedia Engineering 147. Conference proceedings the engineering of sports 11, 366-371, and: Wolfsperger, F., Rhyner, H., 2014. Mechanical and dynamical properties of racing snowboards and their modification by different binding plates. In Procedia Engineering: Vol. 72. Conference proceedings of the engineering of sport 10, 356-361. Both Figures were generated by myself as the leading author of the named publications. Although the underlying data were generated within the cited studies, the here selected Figures have not been printed in the publications (prevent copyright conflicts).

A ski can be understood as a bending beam with high elasticity. Its different materials (fiber compounds, metals, polymers) and geometric properties are specifically arranged, mostly in a sandwich construction design, to reveal the desired overall mechanical and dynamical properties depending on the aimed application and user (Fig. 1.4). When a skier stands on her skis, the weight is distributed along the ski's running base. Depending on the elastic properties of the ski-binding-plate-system and the compressive strength of snow, the pressure can differently be distributed along the ski, creating the macroscopic ski-snow contact (Fig. 1.5).

The ski base is typically made of ultra-high molecular weight polyethylene (UHMWPE) with various additives. Molecular weight, as well as density significantly range from about $3.5 \cdot 10^6$ to $5 \cdot 10^6$ g mol $^{-1}$, and 928 to 1130 kg m $^{-3}$, respectively (P-tex 2000 HC; CPS-GmbH, 2022a vs. P-tex 5188; CPS-GmbH, 2022b). The properties of additives can modify chemical properties like surface energy and contact angles, as well as mechanical factors like strength, hardness, and temperature dependence. The Young's moduli of the above mentioned ski bases also vary distinctively ranging from 380 MPa (P-tex 2000 HC) to about 940 MPa (P-tex 5188). The hardness of ski bases is also assumed to vary, but mostly no information is provided from the manufacturers or hardness values are not comparable. One reason might be the temperature dependency of the hardness of UHMWPE and the low temperature range of use (≤ 0 °C). Scherge et al. (2021) proposed to estimate the hardness H_{PE} , given in MPa, as a function of the snow surface temperature T_{SS} as follows:

$$H_{PE} = 41.66 - 0.33 \cdot T_{SS} \quad (1.1)$$

Ski base surfaces can be modified in various ways on different scales to improve their performance. After manufacturing skies got roughly grinded to make their running surface perfectly planar. Afterwards several stone grinding runs create empirically found functional surface topographies, which have an isotropic roughness strongly aligned along the longitudinal axis of the ski (Fig. 1.6). Stone grinding and manual grooving can alter the surface topography to create specific patterns and roughness depending on snow conditions. The roughness of a ski base along the skis lateral axis usually ranges between 1 and 5 µm. Finally chemical coatings like ski wax modify the surface properties of the ski base concerning its hardness and surface energy. The latter affect the contact angle with water, which is important to reduce friction on wet snow as widely known among ski technicians and has been confirmed by measurements, too (Wolfsperger et al., 2020).

1.1.3 Snow and ice tribometry and modeling

The sliding friction between snow and a ski is governed by different mechanisms on different scales dissipating or transforming kinematic energy of the skier. The relevant scales for frictional processes range from the size of atoms and molecules over nano- and microscale processes (µm to mm) to effects manifesting on the macroscale (> mm). There is a fluent transition between the different frictional processes and their governing scales. For example, the physicochemical surface property hydrophobicity results from atomic properties (e.g. dipoles, electronegativity) as well as from nano and micro scaled roughness effects. From the point of view of ski technicians, the different scales of frictional processes correspond with their three major adjusting screws of ski preparation: (1) The ski selection to provide optimal ski mechanical and geometrical properties (e.g. bending stiffness distribution) depending on the prevailing snow conditions to minimize resistive forces due to effects on the scale of a ski like snow plowing at the ski front. (2) The snow specific topographical configuration of the

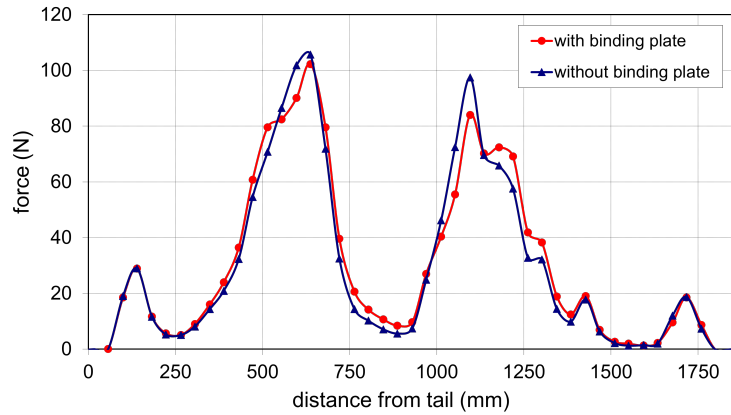


Figure 1.5: Exemplary force distribution underneath a racing snowboard on a 2 mm elastomer used as snow replicate measured on a laboratory device at SLF (unpublished data from Wolfsperger et al., 2014, printed with their authorization).

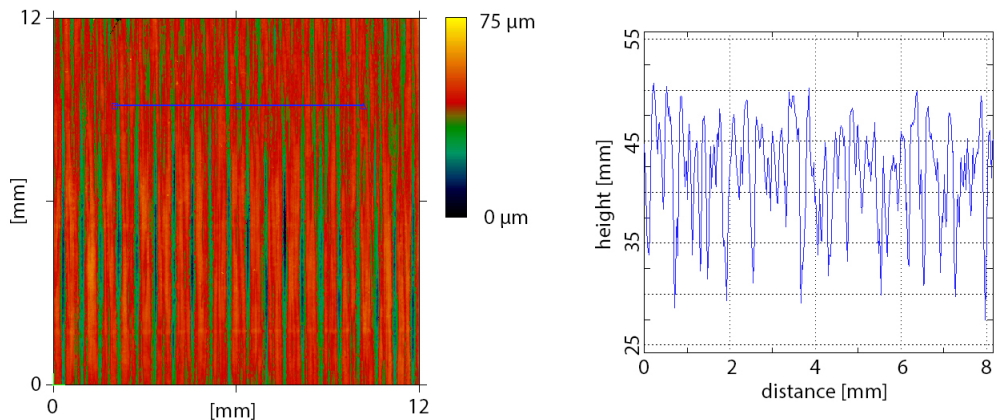


Figure 1.6: Left) 3D surface topography of stone grinded ski base as revealed from white light interferometry. Right) Extracted 2D roughness profile along the marked blue line with values for $R_a = 3.7 \mu\text{m}$ (average roughness) and $R_z = 18.9 \mu\text{m}$ (average maximum profile height) (SLF, 2012, printed with authorization).

gliding surface by manually indented grooves and stone grinding aiming to provide an optimal tribological surface. (3) The proper selection of a ski base polymer as well as waxing composition and surface finishing (e.g. polishing) to provide the optimal physicochemical properties of the gliding surface (atom to nanoscale) but also to optimize mechanical interactions at the ski-snow contacts.

On the scale of the size of a ski (m) to the size of a snow grain (mm) energy is transferred by plowing of snow in front of the ski, and dissipated by snow compaction below the ski. For snow compaction during track setting with a ski, the occurring quasi-plastic compaction resistance was proposed (Slotfeldt-Ellingsen, 1979; Glenne et al., 1987) as follows:

$$F_{comp} = \frac{\Delta z \cdot F_N}{l} \quad (1.2)$$

This process was mostly considered neglectable in existing ski-snow friction studies as the sinkage Δz is expected to be small on compacted ski slopes, while the ski running length l is large. However, on a wet snow piste, sinkage of several millimeters occurs leading still to a small but unnegelectable contribution to ski-snow friction ($COF_{comp} = 0.002$ at 3 mm sinkage). In addition to the deformation work due to snow compaction, which was addressed with a static approach, snow resting on the ski's path also is assumed to experience a transfer of momentum from the ski (Lind and Sanders, 2004). An approximation of this so-called plowing force or frontal impact resistance, was proposed by Glenne et al. (1987) as follows:

$$F_{plow} = \rho_s \cdot \Delta z \cdot w_{slider} \cdot v^2 \quad (1.3)$$

Where ρ_s is the snow density, w_{slider} is the ski width at the tip, and v is the skiing speed. Similar as for compaction, as soon the sinkage reaches a few millimeters this resistance force significantly contributes to the ski-snow friction. Especially on soft wet snow due to its high density and with increasing speed ($COF_{plow} = 0.034$ at 3 mm sinkage, 400 kg m^{-3} , 10 m s^{-1}). However, in-depth knowledge on the compaction processes during skiing is missing, leading to uncertainty concerning the validity of the approximated macroscopic resistance forces. At the transition from macro- to microscale processes, also snow surface deformations due to snow grain disaggregation might be important as a snow surface under real skiing conditions is almost never an entirely compact fully sintered material (Colbeck, 1992; Hasler et al., 2022), except for a classical CC-track in absence of snow fall. Instead, there are mostly loose grains on a compacted basis. However, the contribution of this kind of mechanism has never been investigated so far.

On the microscale, sliding friction is divided into dry friction and lubricated friction processes. For skiing mostly both processes are assumed to occur concurrently, what is referred to as mixed friction. Dry friction describes a solid-solid interaction of the asperities of the contact bodies (Bowden and Tabor, 1950; 1966). This theory reached back to the findings of da

Vinci and Coulomb centuries before, who stated the sliding friction between solid bodies proportional to the normal load and independent from the apparent contact area and from sliding speed. Neglecting friction contributions from adhesion and microscopic plowing, the dry friction force F_{Fdry} originates from shearing off asperities of the contact body of lower shear strength τ , which is for the case of skiing usually the ski wax or the ice (Bowden, 1953; Nachbauer et al., 2016).

$$F_{Fdry} = \tau \cdot RCA \quad (1.4)$$

In contrast to the apparent contact area A_{cntc} , the real contact area RCA strongly affects friction but is up to date difficult to observe or capture metrologically. For most surfaces of elasto-plastic materials that are in contact, RCA is assumed to equal the ratio of normal load and compressive (yield) strength of the softer material F_N/σ_c (Persson and Tosatti, 1996), which is for skiing usually the one of ice. This reveals the dry friction coefficient of a snow or ice slider as follows:

$$COF_{dry} = \frac{F_{Fdry}}{F_N} = \frac{\tau}{\sigma_c} \quad (1.5)$$

Sometimes the compressive strength of ice is replaced by the hardness of ice, as it better represents the complex loading of the microscopic contact geometries (Popov, 2015). Although the mechanical properties of UHMWPE and its temperature dependence can differ, ice has a lower compressive strength than UHMWPE, even for low temperatures, but a higher Young's modulus. Therefore, ice is assumed to yield when the stress exceeds its compressive strength at a ski-snow contact spot, while the ski base deforms mainly elastically and consequentially resists well again wear (e.g. Theile et al., 2009). Interestingly, the dry friction coefficient on snow or ice as described in equation 1.5, gets smaller with lower temperatures, as the ice strength in compression increase distinctively more than in shear with decreasing temperature. Based on τ and σ -values from Carter (1970), COF_{dry} theoretically ranges from 0.11 at -32 °C to 0.45 at 0 °C (Colbeck, 1992). For an experienced skier, this is clearly counterintuitive, but give reason to assume that in skiing other processes might dominate or that assumptions involved with equations 1.4 and 1.5 might have limited validity for sliding on ice or snow. On the one side, snow and ice are not simple elasto-plastic materials. Instead, they show a pronounced viscoelastic and viscoplastic behavior (creep), even at high strain rates relevant for the ski-snow contact. Moreover, the strength of ice asperities under mixed loading as assumably occur at the ski-snow contacts is unclear and might include shear, compression, and possibly tension. On the other side, certain simplifications and assumptions are necessary to be able to quantitatively describe dry ice or snow friction. Colbeck (1992) proposed, based on a plasticity index, that plastic and partly brittle yield is dominant for more angular or dendritic fragile snow grains, shifting to an elastic response for rounded grains and reviewed relative real contact areas $RCA_{rel} = RCA/A_{cntc}$ between 0.1 to 1.4 %, based on ice strength data of Bowden (1953) and Huzioka (1962). Theile et al. (2009) first included viscoelastic snow

and ice deformation as well as information deduced from real snow surface topographies. Assuming a flat slider, the authors found RCA_{rel} of about 0.4 % and a relative contact spot diameter of 110 μm . Bäuerle (2006) used μCT to determine the contact spots between a smooth polyethylene surface and snow. He found RCA_{rel} as 7 ± 1 % at a pressure of 40 kPa for a snow grain size of about 0.5 to 1 mm at a temperature of -10 °C. Contact spot size diameters ranged from 10 to 400 μm with an average of about 150 μm . Hasler et al. (2022) also estimated contact areas from μCT measurements from 2 % to high values up to 27 % (see chapter 4). As Colbeck (1992) mentioned, the ice asperity geometry influences the contact geometry and consequentially the deformation mode and the contact area.

From a ski technicians' point of view, the influence of the ski base topography on the size of the contact area has even higher importance. Böttcher et al. (2017) used Hertzian elastic contact theory to deduce RCA_{rel} between typical ski base topographies in contact with ice. Values of RCA_{rel} ranged from 1.3 % to 2.1 % showing decisive influence on the measured COF . Based on the assumption of pure plastic ice deformation at the ski-snow contact Scherge et al. (2021) calculated RCA_{rel} of about only 0.07 % applying a bearing model approach with realistic ski base topographies and unbounded ice spheres representing unbonded machine-made snow. The authors showed correlation with real ski gliding performance and pointed out, that the spatial scale of the grinding structure should be adapted to the snow grain size to prevent snow grains from penetrating into the structure which increases the RCA . Beyond considerations concerning effects of topography and the mechanics of the ice-UHMWPE contact, the RCA gets enlarged by the horizontal movement of the slider, flattening ice asperities, be it due to frictional melting or abrasion (e.g. Bäuerle, 2006). Moreover, for low snow densities, larger scaled brittle deformation of the snow matrix occur, which assumably involve ice grain rearrangement until the snow is compacted to counteract the external load, while the number of grains in contact grew. When sliding on snow, it is not clear how RCA is affected during this process of compaction and ice grain rearrangements with repeated, mainly brittle bond and grain failure, fast sintering, and intergranular friction. Most likely, besides the number of contacts also the contact spot size rises during the pass of the ski (Lever et al., 2021).

To distinguish if morphological changes of the ice asperities resulted from wear or other deformation mechanisms or from melting and refreezing induced by frictional heating is difficult. Although the theory of melt water generation has found broad acceptance (e.g. Colbeck, 1992; Nachbauer et al., 2016) since it was first hypothesized (Bowden and Hughes, 1939), Lever et al. (2019; 2021) stated ice abrasion at the contacts spots and the absence of self-generated water as the dominating process of ski-snow friction even at temperatures above -10 °C. Although their data were not convincing (e.g. temperature measurements of thin films by infrared emission), the work pointed out the difficulty to disentangle dry and lubricated frictional processes of a ski sliding on snow.

Colbeck (1992) argued that for dry snow friction effects of adhesion can be neglected, as UHMWPE and ice are very dissimilar materials concerning their molecular structure, their surfaces are not molecular smooth, and the time for interaction is too small. Since heat accumulates along the ski length, dry processes are assumed dominantly only at the front of

the slider or at very cold temperatures (Colbeck, 1992). In contrast, Makkonen et al. (1994; 2014) presented a formulation of the dry friction between ice and a slider included adhesive effects (besides others) where the frictional power is calculated from the differences of surface energy when bodies are in contact with each other ($\gamma_{ice-slider}$) at the time of through pass compared to the non-contact situation before (γ_{ice}) and after (γ_{slider}) it. The COF_{dry} then follows as:

$$COF_{dry} = \frac{n \cdot a}{2 \cdot F_N} \cdot (\gamma_{ice} + \gamma_{slider} - \gamma_{ice-slider}) \quad (1.6)$$

where n describes the number of contacts and a their size. Although dry friction, under most snow conditions, is most likely not the dominating process of ski-snow friction, it has high importance from a thermodynamically point of view, as it acts as heat source to generate melt water which then acts as a lubricant. The rate of heat generation is given by the product of COF , the skier's speed v , and the normal force F_N as follows:

$$\frac{dQ}{dt} = COF_{dry} \cdot v \cdot F_N \quad (1.7)$$

To understand the dynamics of melt-water generation on ice, heat generation and temperature increase at the contacts was first investigated by Evans et al. (1976). The authors divided the generated frictional heat into three parts. Heat conducted through the base (1st term in Eq. 8), heat diffusing into the snow (2nd term), and heat used to melt ice (3rd term). The sum of the heat fractions equals the contribution to friction due to energy transferred into heat (sensible and latent) and can be expressed as a COF when divided by F_N . Depending on the type of heat transfer into slider and ice, the material properties (thermal conductivity λ , specific heat capacity c , and density ρ), skiers speed and temperature difference of snow and slider $T_{melt} - T_{SS}$, the following expression was revealed for a rectangular area of contact:

$$COF_{wet} = \frac{C_1 \lambda_{slider} \cdot (T_{melt} - T_{SS})}{F_N \cdot v} + \frac{2b\lambda_s \cdot \left(\frac{L_{wet}}{\pi \cdot D_s}\right)^{\frac{1}{2}} \cdot (T_{melt} - T_{SS})}{F_N \cdot v^{\frac{1}{2}}} + COF_{melt} \quad (1.8)$$

L_{wet} is the length and b the width of the lubricated ski. $D_s = \lambda_s \rho_s^{-1} c_s^{-1}$ is the coefficient of thermal diffusion depending on the material properties of the contact bodies. The constant C_1 is a function of the contact area and geometry of the slider. COF_{melt} is the resistance caused by the heat used to melt snow, which according to Evans et al. (1976) makes only a small contribution up to 0.005. Equation 1.8 shows that heat transfer induced friction increase with colder snow and slower speeds and for sliders with high conductivity. Besides a quantification of the heat induced friction contribution of a snow ski, the thermodynamical approach also allows the calculations of the so-called dry length of a ski, which determines

the part of the ski, starting at the tip, which is subjected to dry friction before any ice could be melted from frictional heat. Assuming, that the pressure exerted by a slider is limited by the bearing capacity of the material beneath the slider, the dry length can be calculated as follows (Evans et al., 1976; Colbeck, 1992; Nachbauer et al., 2016):

$$L_{dry} = \frac{\pi \cdot \lambda_s^2 \cdot (T_{SS} - T_{melt})^2 \cdot RCA^2}{4 \cdot COF_{dry}^2 \cdot D_s \cdot v \cdot F_N^2} \quad (1.9)$$

Based on the work on Evans et al. (1976), others elaborated thermodynamical approaches to calculate the heat balance at the frictional ice or snow contact and combined them with classical approaches of dry and hydrodynamic friction aiming to calculate the resulting water film thickness at the contact, and by that, predicting the frictional regime for prevailing conditions of the ski-snow system (Colbeck, 1988; Oksanen and Keinonen, 1982; Lehtovaara, 1989, Makkonen and Tikanmäki, 2014). Although a mixed lubrication regime is mostly assumed for skiing, the hydrodynamic friction regime of fully lubricated contacts needs to be considered. Similar as for dry friction, fully lubricated friction is described as the resistance against shearing. However, it is a viscous fluid which is sheared instead of a solid body, and in the case of skiing, this fluid is water. Lubricated friction is proportional to the speed gradient within the fluid $\frac{dv}{dz}$, whereas dz represents the water film thickness h , as well as to the area of wetted contact RCA_{wet} . Including the dynamic viscosity of water η as proportional factor describing the fluid property, and assuming laminar flow within the water film, the coefficient of friction due to a hydrodynamic resistance at fully lubricated contacts is given by

$$COF_{hydro} = \frac{\eta \cdot RCA_{wet} \cdot v}{h \cdot F_N} \quad (1.10)$$

Analogous to dry friction, the size of the lubricated contact area is crucial to well estimate the hydrodynamic contribution to the ski-snow friction. RCA_{wet} is not independent from the amount water available at the contact and is assumed to grow with increasing water film thickness. Beyond that, RCA_{wet} is affected by deformations of ice asperities during dry friction prior to the lubricated state and by larger snow deformations. A linear increase of hydrodynamic friction is expected for increases of speed and/or viscosity. Nano-rheological measurements revealed distinctively elevated values of viscosity (35 to 80 mPa s at 0 °C) of melt water at an ice-glass frictional interface compared to pristine water (2 mPa s) increasing with temperature and decreasing with speed (Canale et al., 2019). Changes of viscosity correlated with measured friction which let the authors conclude a hydrodynamic-like behavior of the interfacial water film. However, they assumed the film a water-ice particle-like emulsion causing the high viscosity values and questioned the prevailing theories of melt water lubrication with a straightforward transition from its solid to liquid phase. They conclude that low ice friction results from an excellent hydrodynamic lubricant behavior of the high viscosity interfacial H₂O, able to bear higher loads without getting removed from the contacts, preventing solid-solid contacts better, even at a rather thin film thickness. As the tested speeds

were below 0.1 m s^{-1} , the experiments' relevance for skiing is limited.

Besides a correct representation of the water generation within snow and ice friction models, the description of processes removing water from the contacts are important. Colbeck (1988) formulated the balance among frictional melting, water removal, and film thickness. Mechanisms of water removal were distinguished between removal by shear and by squeeze out. The shear removal mechanism (and similarly the hydrodynamic friction) was later assumed to be weakened by water slippage (expressed in Eq. 1.11 by $S = [0...1]$) at the gliding base of a ski which are typically hydrophobic (Colbeck, 1992). Accounting for that, the water film thickness can be assumed to reach an equilibrium state if the meltwater production rate equals the water removal by squeeze and shear which was formulated by (Colbeck, 1992) as follows:

$$\frac{\pi \cdot \eta}{Q_L \cdot \rho_{ice}} = \frac{2\pi}{3\eta \cdot C_A} \cdot \left(\frac{h^2}{v \cdot r_c} \right)^2 + S \frac{h^2}{v \cdot r_c} \quad (1.11)$$

where Q_L is the latent heat of fusion of ice (333.5 kJ kg^{-1}) and $C_A = RCA_{rel} \cdot F_N^{-1}$ the constant ratio of contact area to load, and r_c is the size of the contact of an ice sphere on a flat glider. Colbeck (1988, 1992) assumed 1D transient heat conduction for different boundary conditions (e.g. $\lambda_{slider} = 0$; $T_{ss} < \text{or} = 0 \text{ }^\circ\text{C}$) to calculate melt water production rates and the resulting water film thickness, which was then used within the equations of the different frictional contributors: $COF_{dry} = C_{dry} \cdot \exp(-\beta \cdot h)$ assuming to decrease with increasing film thickness, COF_{hydro} as formulated in Equation 1.10, and COF_{cap} addressing friction due to capillary attraction (further explanations see below). The parameters C_{dry} and β were deduced revealing a best fit to reported friction data. The three snow friction components were then combined, to an overall analytical expression of the COF , taking wet and dry friction as parallel processes as follows:

$$COF = COF_{cap} + \frac{COF_{dry} \cdot COF_{hydro}}{COF_{dry} + COF_{hydro}} \quad (1.12)$$

Although there were several limitations of Colbeck's analytical description of the self-lubricated snow friction (e.g. $C_A = const.$; simplified contact geometry and mechanics), it provided plausible explanation of the observed friction during real skiing, as well as an overview on possible order of magnitudes of the different sub-processes and their collective dependence on the water film thickness. The author concluded that the COF varies little over a rather wide range of film thicknesses (0.2 to 1.2 μm , Fig. 1.7). In his eyes, this confirmed the slight change of ski-snow friction over a wide range of speeds and temperatures and is a result from the balanced interaction between heat generation and water removal within the dominating lubricated frictional regime.

Makkonen and Tikanmäki (2014) deduced a comparable formulation based on the work of

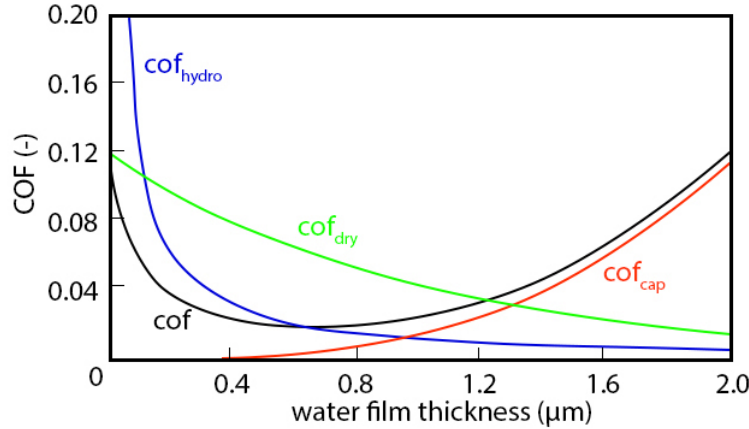


Figure 1.7: Contributions to the ski-snow friction adapted and reprinted from Colbeck (1988), showing the total friction coefficient COF , dry friction coefficient COF_{dry} , lubricated friction coefficient COF_{hydro} , and the friction coefficient due to capillary forces COF_{cap} versus water film thickness for a contact spot diameter of 2 mm and a velocity of 10 m s^{-1} .

Oksanen and Keinonen (1982) also considering the coupling between the hydrodynamic friction and heat conduction but included an extended description of the mechanical contact considering the material hardness of both contact bodies. As mentioned above, Böttcher et al. 2017, elaborated the model of Makkonen and Tikanmäki by implementing *RCA* using Hertzian elastic contact theory as well as the temperature dependence of the hardness of ice and UHMWPE. From modeled and measured data, they found ice temperature and *RCA* as decisive parameters of the ice-ski tribosystem. To best fit modeled and measured data, *RCA* was assumed larger than revealed from Hertzian contacts. This adaptation compensated for friction contributions assumably due to microscopic ploughing. Bäuerle, (2006) presented a numerical quasi-2D model for sliding on ice including dry friction, heat generation and transfer, as well as hydrodynamic friction and water film squeeze out. A major advantage of his approach is the ability to model the evolution of contacts and water film throughout the length of a slider. In consequence, *RCA* was no longer treated as a constant, but as a process parameter which increases due to ongoing melt of ice asperities. By that, measured evolution of COF could be explained in the model with increasing RCA_{wet} . However, the model did not predict properly the magnitude of the measured COF values, whereas the water film thicknesses of 0.1 to 1 μm appeared realistic compared to calculations from other groups, which proposed film thicknesses of about 0.001 to 1.3 μm (Evans et al., 1976; Oksanen and Keinonen, 1982; Lehtovaara, 1989, ; Makkonen and Tikanmäki, 2014). A very few estimations of water film thicknesses underneath a snow or ice slider were deduced from measurements. Ambach and Mayr (1981) measured water film thicknesses between 5 and 14 μm with a 100 mm^2 capacitance sensor integrated into a real ski. Canale et al. (2019) reported on measured water film thicknesses of 0.1 to 0.5 μm for a borosilicate glass sphere sliding on ice at temperatures from -16 to 0 $^{\circ}\text{C}$ and speeds up to 0.1 m s^{-1} . Assuming typical

average roughness's of a ski base ranging from 1 to 5 μm , modeled water thicknesses rather indicate boundary or mixed lubrication friction regimes, than pure hydrodynamic friction.

Glenne et al. (1987) pointed out that not only self-generated water due to frictional heat should be considered, but also the snow's interstitial liquid water content (*LWC*), upward percolation of liquid water to the sliding interface due to snow compaction, and meltwater due to local high pressures. Although the friction of skis on wet snow has high relevance in practice, as the *COF* rises, and effects of ski preparation become larger, wet snow friction processes have rarely been investigated. Colbeck (1988, 1992) assumed that capillary effects may add drag to the ski due to the hysteresis in the contact angle of water (advancing angle $>$ receding angle as described by Popov, 2015) bridging unloaded snow grains with the ski base. Moreover, a vertical capillary force must be assumed, whose direction depends on the contact angle of the water with the contact body materials revealing shape and pressure of the water bridge (Popov, 2015). As ice is hydrophilic, a downward force can be assumed, which gets the smaller, the more the contact angle on the ski base exceeds 90°. Although forces perpendicular to the direction of motion cannot directly impact friction, a downward force possibly reduces the water film thickness at adjacent lubricated contacts, which then have to bear the skier's weight plus the sum of capillary downward forces, which in consequence, would increase hydrodynamic friction. Without giving a physical description of the mechanisms of capillary effects on the ski-snow friction, Colbeck (1988) anyhow assumed its importance increase with the availability of water coming from squeeze and shear removal from the lubricated contacts, which follows h^4 and h^2 , respectively. According to that, while neglecting other water sources, he proposed to describe capillary drag as given in Equation 1.13, where C_{cap} is a constant for given snow conditions.

$$COF_{cap} = C_{cap} \cdot h^3 \quad (1.13)$$

The existence of possible mechanisms resulting in additional drag due to excessive amounts of water at the interface have neither been proved nor thoroughly investigated. However, high *COF* (0.1) as measured on wet snow conditions (Kuroiwa, 1977; Leino and Spring, 1984) could not be explained by an increase of hydrodynamic friction alone. Although Bäuerle (2006) stated, based on modeled data, that a strong increase of RCA_{wet} (100 %) could explain high *COF* (0.12), which he had measured at speeds of 9 m s^{-1} on 0 °C ice, there is reasonable doubt if such an *RCA*-value can be realistic.

Due to the existing knowledge gaps, as well as because of the rising relevance of wet snow friction in time of climate warming, more research is required. On the one side, real skiing *COF* data are required for different snow conditions and speeds to quantify the collective result of all involved frictional processes as a total *COF* in a manner, which allows to recognize shifts between different dominating regimes. On the other side, tribological investigation have to be conducted to relate quantified effects on the real scale, with frictional processes taking place on the macro- and microscale. Concerning capillary drag (Eq. 1.13), this means that additional water sources must be included and their role of modifying the interfacial

water distribution has to be unveiled. Similar to the existing work summarized above, which pronounced the interdependence of the different mechanical and thermodynamical processes, a major challenge in wet snow friction research is to disentangle indirect effects of excessive water on hydrodynamical processes (e.g. increased F_N , increased RCA_{wet}) from capillary effects based on the contact angle hysteresis. Beyond that, wet snow friction is increasingly influenced by the macroscopic resistances of plowing and compaction as the snow softens with melting. The given summary of the here relevant state-of-the-art snow and ice tribological research is best concluded with the words of Glenne et al. (1987): “*A runner on snow slides on snow crystals (grains) and an interface, more or less soft, more or less wet, more or less present. This insidious interface, a result of ambient conditions, compaction, and frictional mechanisms, controls the sliding resistance through the amount and types of material in contact with the runner.*”

1.2 Research questions

As set out above the following research questions were formulated and divided into two groups related a) to real scale field measurements, and b) to down-scaled tribological and mechanical measurements in the cold laboratory:

- a1) What is the full range of the *COF*, for skis and a snowboard across a wide range of snow conditions of a groomed slope? Are the applied on-field *COF* measurements sufficiently accurate to investigate the influence of snow and process parameters on the ski/SB-snow friction?
- a2) Can simple categories of snow conditions determine typical levels of the *COF* distinctly? How well do physical properties of snow, and their interactions, predict the snow friction of skis and snowboards? Should meteorological parameter be preferred as *COF* predictors?
- a3) How is the *COF* influenced by the gliding speed? In which way does this relation changes with different snow conditions?
- b1) Can snow samples be prepared, which represents the range of snow conditions as observed on the field? To what extent correspond a *COF* as measured on a short distance snow tribometer to the findings from the real scale.
- b2) In which way does mode and extent of macroscopic snow deformation change with different snow conditions? How does that influence the *COF* and the microscopic real contact area?
- b3) In which way is the distribution of liquid water within the snow influenced by the macroscopic snow deformation and by different snow physical properties. How is that affecting the water accumulation at the ski-snow interface (solid-liquid phase interaction under compression).

To answer the formulated research questions, the following research design and methods were selected.

2 Methods

2.1 Study overview

This study was divided into two parts investigating the ski/SB-snow friction. (1) On the field, to quantify the snow friction and its dependence on snow conditions promising the best possible external validity, and (2) in the laboratory, to be able to observe involved processes concerning the snow deformation, the *RCA* between a typical gilding surface and the snow, as well as the behavior of containing liquid water during loads occurring at skiing on snow at the melting point.

The field study consisted of calculations of the ski/SB-snow friction deduced from kinematic and aerodynamic measurements of athletes, as well as of comprehensive snow surface and meteorological measurements. The former were applied for the first time to access the ski/SB-snow friction and included wind tunnel measurements with skiers and snowboarders. The latter required work on the development and calibration of snow measurement devices. Methods involved in the field study are explained in chapter 2.2.

The laboratory part of this study was realized with an existing infrastructure consisting of a short-distance linear tribometer, which also served as a compression testing machine and was placed in a cold chamber. Several tools, instruments and methods were applied, adapted, or developed to infer the above-mentioned processes of the ski-snow frictional contact as explained in chapter 2.3.

2.2 Ski/Snowboard-snow friction field measurements

2.2.1 Research design

The following subchapter, including Figures 2.2, 2.3 and Table 2.1, is part of the publication: Wolfsperger, F., Meyer, F., Gilgien, M., 2021. The snow-friction of freestyle skis and snowboards predicted from snow physical quantities. Frontiers in Mechanical Engineering, 7, 728722.

A test team consisted of three skiers and three snowboarders (1.82 ± 0.05 m; 80.3 ± 8.6 kg; 36 ± 1.2 years; ski and/or snowboard instructor level or higher) was acquired. Gliding tests

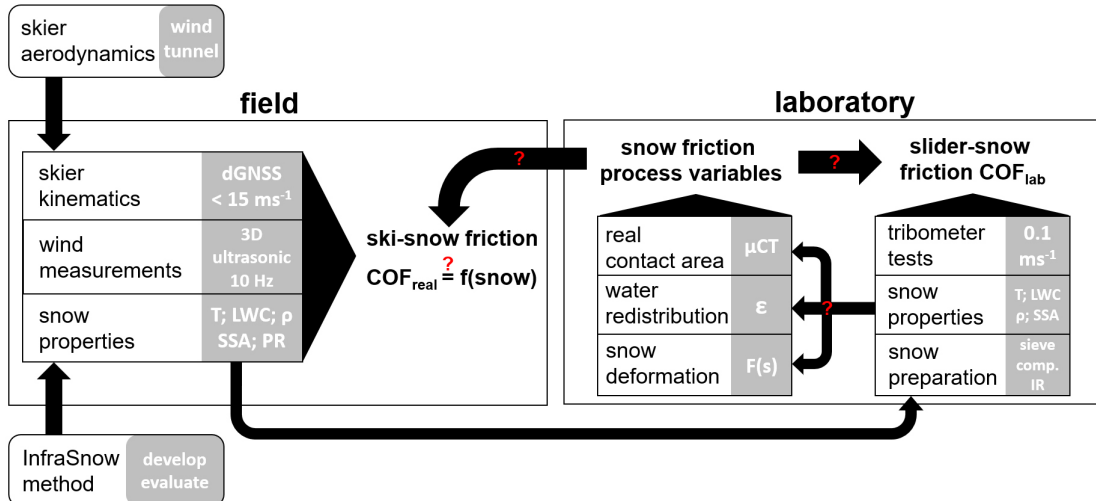


Figure 2.1: Overview and interlinks of the study's components. Red question marks denote the major research questions.

were performed on 14 days during winter 2016/17 and 2017/18 at Davos, Weissfluhjoch (WFJ, 2600 m) and Davos, Bolgen (BOL, 1580 m) on groomed gliding tracks that were closed to the public (Fig. 2.2, 2.3). The test days were selected to capture a wide range of snow conditions typical on ski slopes. A test day included several (7 to 24) consecutive runs by one skier and/or one snowboarder using the same test skis or snowboard for each data collection.

The test skis/snowboard were equipped with a sintered transparent running base made of ultra-high molecular weight polyethylene and were waxed by a professional ski/snowboard technician (Steiner Sport, Davos, CH) prior to each test day, using a mid-temperature hydrocarbon ski wax (Beta Mix Red, Holmenkol GmbH, D). Topology and hydrophobicity of the running surfaces were characterized using tactile 2D roughness measurements (MarSurf PS1, Mahr GmbH, D), as well as dynamic contact angle measurements (Drop Shape Analyzer, Krüss GmbH, D) in waxed and unwaxed states (Table 2.1).

The skiers were running in a defined and easy-to-reproduce, mid-extended posture without poles, with the hands placed on the knees and straight arms with the elbow joint in full extension (Fig. 2.4). The snowboarders, were running in a typical riding posture, characterized by considerable knee flexion, slight elbow flexion and upper arm abduction. Athletes wore the same, regular-fit personal ski or snowboard apparel for each test day. The aerodynamic drag and lift were quantified in a wind tunnel experiment using the same posture and apparel as during the gliding tests. Further wind tunnel measurements were conducted to develop empiric aerodynamic models for freestyle skier and snowboarder depending on posture and apparel aiming to improve the validity of jump kinematic models (Wolfsperger et al., 2021). Athletes' kinematics, wind velocity, meteorological parameter, and snow parameters were

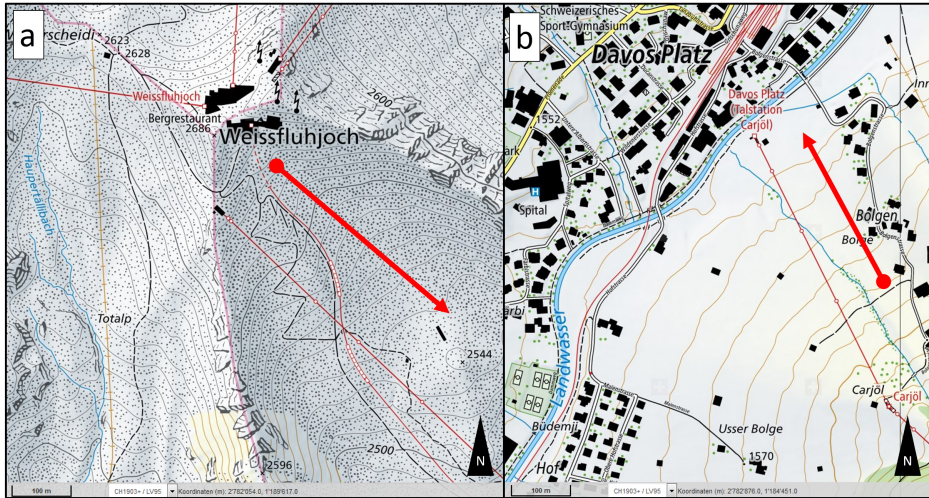


Figure 2.2: Location of the gliding tracks (red arrows) at Weissfluhjoch (a) and Bolgen (b) (© swisstopo, 2021).

captured as described below. Each run was documented by videotaping (Fig. 2.3).

2.2.2 Data acquisition & processing

2.2.2.1 Aerodynamics

The following subchapter, excluding Figures 2.4 and 2.5, is part of the publication: Wolsperger, F., Meyer, F., Gilgien, M., 2021. Towards more valid simulations of slopestyle and big air jumps: aerodynamics during in-run and flight phase. *Journal of Science and Medicine in Sport*, 24(10). I predominantly conceived and conducted the here described data acquisition and processing. Co-author Frederic Meyer assisted the wind tunnel measurements.

To quantify drag and lift forces representative for a straight run of each athlete of the test team, wind tunnel measurements were carried out in an atmospheric closed loop wind tunnel with a closed test section of 7.5 x 11 meters, at RUAG Aerospace Center at Emmen, Switzerland (Fig. 2.4). Each skier (A, B, D) and snowboarder (A, C and D) performed two trials each with the predefined in-run posture at relative air flow speeds v_{rel} of 9, 16.7 and 23.6 m s^{-1} , wearing the same regular fit snow sports apparel as for the gliding tests. For each trial drag force F_D , lift force F_L , the dynamic pressure $p_{dyn.} (= \frac{1}{2} \rho_{air} v_{rel}^2)$, and the air temperature T_{air} , were measured at 0.5 Hz during 20 s. The sensor accuracy was ± 0.01 N for the forces and ± 0.01 Pa for the dynamic pressure. Drag area $c_D A$ and $c_L A$ were calculated as described in Equations 1.14 and 1.15.



Figure 2.3: Gliding tracks at Davos Weissfluhjoch (a) and Bolgen (b) with a skier and a snowboarder holding the defined mid-extended posture. Side view photographs of this posture were shown in (Wolfsperger et al., 2021).

Table 2.1: Properties of the test skis and snowboard including surface roughness parameters ($n = 10$) and dynamic contact angles of distilled water ($n = 8$). The advancing (receding) angle is the contact angle which occurs in the course of wetting (de-wetting) of the ski base.

	SKI	SB
model	Scott Park 178	Burton Vapor 157
length / width / running length (mm)	1780 / 1410	1570 / 1170
width (tail / waist / tip) (mm)	114 / 78 / 103	294 / 250 / 294
weight (incl. bindings) (g)	5684	4833
mean peak-to-valley height R_z (μm)	20.3 \pm 2.3	19.4 \pm 3.0
mean width of profile elements R_{S_m} (μm)	345.8 \pm 65.1	333.3 \pm 68.3
profile skewness R_{sk} (μm)	-0.31 \pm 0.25	-0.45 \pm 0.17
advancing angle unwaxed ($^\circ$)	92 \pm 2.4	79.3 \pm 3.5
receding angle unwaxed ($^\circ$)	56.3 \pm 5.5	45 \pm 6.9
advancing angle waxed ($^\circ$)	98.1 \pm 2.5	104.8 \pm 4.6
receding angle waxed ($^\circ$)	72.4 \pm 3.2	75.1 \pm 3.8



Figure 2.4: Skier during wind tunnel measurements to reveal the individual speed-dependent functions of the aerodynamic drag and lift.

$$c_L A = \frac{2 \cdot F_L}{\rho_{air} \cdot v_{rel}^2} \quad (2.1)$$

$$c_D A = \frac{2 \cdot F_D}{\rho_{air} \cdot v_{rel}^2} \quad (2.2)$$

Mean ($\pm sd$) $c_D A$ and $c_L A$ values were calculated for each athlete and speed level. The dependencies of $c_D A$ and $c_L A$ on speed of each athlete were then expressed, using least squares first or second order regression (Fig. 2.5), which were later used to approximate the aerodynamic forces occurring during the gliding tests. R_{adj}^2 and slopes of regression m were stated if significant ($p \leq 0.001$) to quantify the strength and relevance of those $c_D A/c_L A$ -speed relationship. The uncertainties of the regression coefficients were given by their 95 % confidence intervals ($\pm CI/2$).

2.2.2.2 Kinematics

*The following subchapter, including Figure 2.6, is part of the publication: Wolfsperger, F., Meyer, F., Gilgien, M., 2021. The snow-friction of freestyle skis and snowboards predicted from snow physical quantities. *Frontiers in Mechanical Engineering*, 7, 728722. Co-author Matthias Gilgien contributed to the publication with operating the calculation routine to reveal position data from the dGNSS signal using the commercial software Justin as he described in the first 7 lines of the following paragraph. Based on the revealed position data all data*

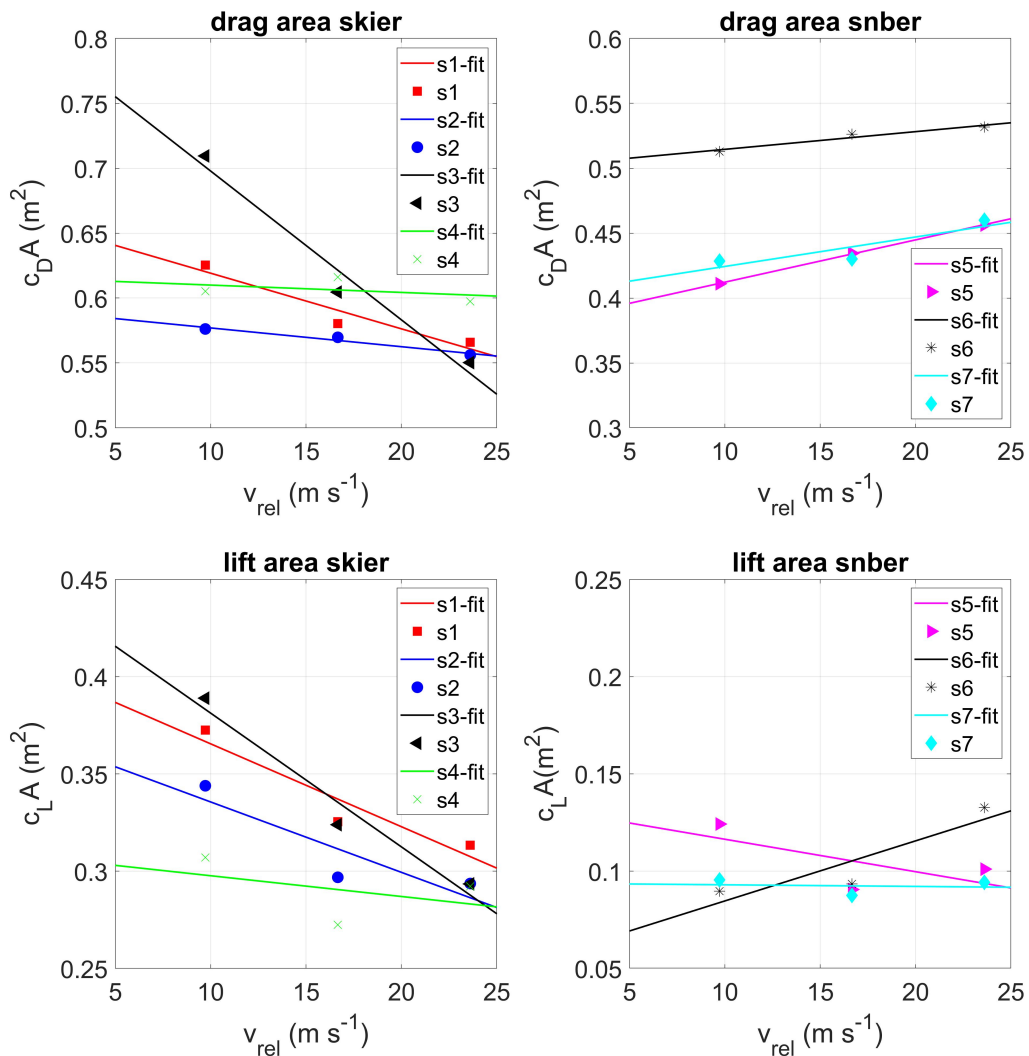


Figure 2.5: Speed dependent functions of the drag area (top) and lift area (bottom) of the test skiers (left) and snowboarders (right) holding the inrun-posture as shown in Fig. 2.4.

processing and calculations were performed by myself. Co-author Frederic Meyer assisted with the kinematic measurements on the field.

When gliding down the test track, athletes' positions were measured with a differential global navigation satellite system (dGNSS). The dGNSS system was composed of a GNSS antenna (G5Ant-2AT1, Antcom Corp., USA) carried on the athlete's helmet and a GNSS receiver (Alpha-G3T, Javad GNSS Inc., USA) carried on the athlete's chest, underneath the jacket. Dual frequency (L1 and L2) GPS and GLONASS signals were logged at 25 Hz and a short baseline kinematic carrier phase dGNSS solution was calculated using Justin (Javad GNSS Inc., USA) post-processing software (Gilgien et al. 2013). Positions were smoothed using the dGNSS solutions accuracy estimates as weighted into a spline filter. From the smoothed position data, the distance travelled s_x was calculated as the aggregated distances between the measured positions and smoothed (4-second-moving average). The athlete's instantaneous velocity and acceleration vectors were computed as the first and second time derivatives using the finite central difference formulae followed by smoothing (4-second-moving average) and removal of spikes (Hampel filter: 1-second-window, 1-sd-threshold). Instantaneous speed v was calculated as the norm of the velocity vector. Instantaneous acceleration a along the skier's direction of travel was calculated by firstly projecting the acceleration vector on the velocity vector and secondly calculating the scalar of the projected acceleration vector. The slope α and curvature κ of the terrain along the trajectory was calculated from the incline of the instantaneous velocity vector (Gilgien et al., 2013, Gilgien et al., 2015).

The relative airflow speed resulted from the sum of wind and athlete velocity. Speed dependent drag and lift area were determined by wind tunnel measurements for each athlete considering their personal apparel and posture characteristics. This allowed an accurate calculation of the aerodynamic force components of drag and lift throughout each run (Eq. 2.3). A mechanical model of the athlete as a point of mass m was used (Fig. 2.6), incorporating air drag and lift force, as well as gravitational (F_{Gx} , F_{Gz}) and radial forces F_R (Eq. 2.4) to solve the equation of motion for the friction force F_F (Gilgien et al., 2015). The coefficient of friction was calculated by the division of F_F by the resultant normal force F_N (Eq. 2.5). The friction force included all resistive forces of the ski-snow interaction that counteracted the direction of motion, including micro-mechanical friction forces or dissipation due to snow deformation on the macroscale.

In total, 239 runs were captured, of which 25 runs had to be excluded, due to inaccurate position data (18), strong wind fluctuations (5), or posture variations of the athlete (2). Of the remaining 214 runs, 99.5 % of the time, the post processing software managed to solve the ambiguities in the dGNSS solution (dGNSS fixed solution) and for 0.5 % the solution was dGNSS float (when the ambiguity integers could not be fixed in the dGNSS solution).

$$\begin{pmatrix} F_D \\ F_L \end{pmatrix} = \frac{1}{2} \cdot \rho_{air} \cdot \begin{pmatrix} c_{DA} \\ c_{LA} \end{pmatrix} \cdot v_{rel}^2 \quad (2.3)$$

$$F_R = -m \cdot v^2 \cdot \kappa \cdot \text{sign} \left(\frac{d^2 s_z}{ds_x^2} \right) \quad (2.4)$$

$$COF = \frac{F_F}{F_N} = \frac{F_{Gx} - F_D - m \cdot a}{F_{Gz} + F_R - F_L} \quad (2.5)$$

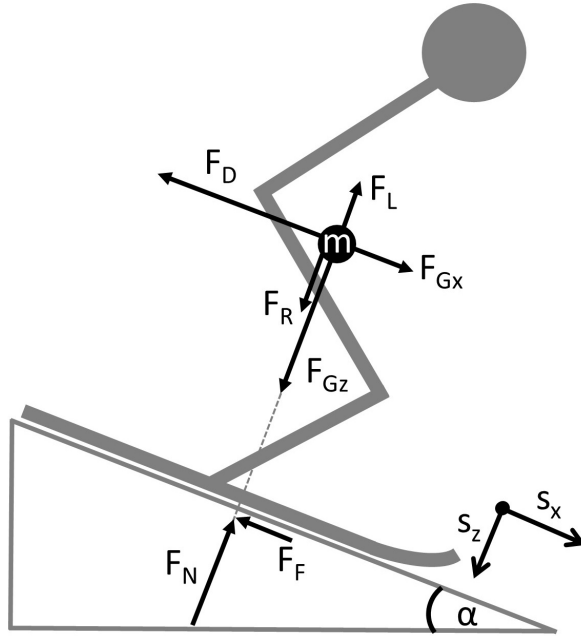


Figure 2.6: Free body diagram visualizing the forces acting on an athlete during a test run. The curvature of the terrain is not visualized.

2.2.2.3 Wind and weather

The following subchapter, including Table 2.2, is part of the publication: Wolfsperger, F., Meyer, F., Gilgien, M., 2021. The snow-friction of freestyle skis and snowboards predicted from snow physical quantities. *Frontiers in Mechanical Engineering*, 7, 728722.

During the gliding tests, 3D wind velocities were recorded at 1 Hz with two ultrasonic anemometers (Model 8100, R. M. Young Company, USA) at the top and the bottom of the test tracks. Wind velocities were interpolated from 1 to 25 Hz using a symmetric FIR filter method to synchronize with the kinematic data. The UTC-GPS time offset of 18 seconds, and the wind logger clock offset, which was manually annotated, were considered in the time synchronization. Wind data were smoothed and cleaned of spikes as described for the velocity

above. The instantaneous ambient wind velocity at the position of the athlete during a run was calculated from the two wind stations, placed at the top and bottom of the track. The distance between athlete and the wind stations was used to weigh the contribution from each station measurement to the weighted average wind velocity. The components of the wind vector were rotated into the athletes' instantaneous position coordinate system (trajectory). The atmospheric pressure, air temperature, relative humidity RH , and incoming shortwave radiation SWR were measured with stationary (SLF, 2021) and mobile (Sensorscope, CH) weather stations proximate to the test tracks (Tables 2.2, 2.3). The air density air ρ_{air} was calculated from atmospheric pressure p_{atm} , air temperature T_{air} and relative humidity RH using the ideal gas law (Eq. 2.6) adapted with an approximated universal gas constant for humid air R_h ranging from 287.1 to 288.3 $J\ kg^{-1}\ K^{-1}$ (Sonntag, 1982).

$$\rho_{air} = \frac{p_{atm}}{R_h \cdot T_{air}} \quad (2.6)$$

Table 2.2: Weather description and average (mean \pm sd) weather parameters during the captured runs of each test day (date).

date	weather	T_{air} (°C)	RH (%)	wind (m s^{-1})	SWR m 2)	(W	track	athlete	runs anal- ysed / cap- tured
2017-03-30	sunny	3.3 \pm 0.3	32 \pm 3	-0.3 \pm 0.6	832 \pm 72	WFJ	s2	15 / 15	
2017-03-31	sunny	2.0 \pm 0.4	48 \pm 1	-1.2 \pm 0.6	829 \pm 99	WFJ	s7	9 / 11	
2018-02-01	strong snowfall	-7.7 \pm 1.0	98 \pm 1	1.2 \pm 2.1	214 \pm 12	WFJ	s2	5 / 5	
2018-02-07	partly sunny, fog	-8.1 \pm 2.6	83 \pm 27	-0.2 \pm 0.6	296 \pm 125	WFJ	s1	10 / 10	
2018-02-08	fog, slight snowfall	-11.2 \pm 0.6	97 \pm 2	-0.6 \pm 0.5	481 \pm 98	WFJ	s5	8 / 9	
2018-02-13	sunny	-16.0 \pm 0.8	55 \pm 13	0.1 \pm 0.7	600 \pm 57	WFJ	s2	10 / 11	
2018-02-21	partly sunny, slight snowfall	-12.9 \pm 0.4	77 \pm 4	-0.3 \pm 0.7	435 \pm 117	WFJ	s1, s5	6 / 6	
2018-02-22	cloudy to sunny	-10.0 \pm 0.4	77 \pm 8	-1.5 \pm 1.2	643 \pm 257	WFJ	s1, s5	12 / 13	
2018-03-03	cloudy to sunny	-5.2 \pm 0.4	68 \pm 15	-1.3 \pm 1.4	478 \pm 186	WFJ	s1, s7	23 / 24	
2018-03-04	sunny	-4.7 \pm 0.5	45 \pm 6	-2.2 \pm 1.1	681 \pm 83	WFJ	s4, s5	24 / 29	
2018-03-28	cloudy to sunny	7.5 \pm 2.0	57 \pm 8	0.5 \pm 0.3	584 \pm 210	BOL	s4, s6	30 / 37	
2018-04-06	sunny	8.9 \pm 3.9	25 \pm 7	1.1 \pm 0.5	697 \pm 112	BOL	s2, s7	23 / 29	
2018-04-08	sunny	9.8 \pm 3.1	52 \pm 22	1.6 \pm 0.6	692 \pm 155	BOL	s1, s7	39 / 40	

2.2.2.4 Snow

The following subchapter, including Table 2.3 and excluding Figure 2.7, is part of the publication: Wolfsperger, F., Meyer, F., Gilgien, M., 2021. The snow-friction of freestyle skis and snowboards predicted from snow physical quantities. *Frontiers in Mechanical Engineering*, 7, 728722.

The snow surface at the gliding track's top section was characterized multiple times during a test day by its temperature T_{ss} , specific surface area SSA , density, volumetric liquid water content LWC and its penetration resistance PR . The SSA characterizes aspects of the snow microstructure of a porous material like snow and is defined as the total surface area of the ice/air interface of a snow sample per ice volume (Fierz et al., 2009). The SSA is high for small and filigree structures and is low for coarse and round ones. T_{ss} was measured using a digital resistance thermometer (HI 98501, HANNA Instruments Switzerland AG, CH). The SSA was deduced from the snow's near infrared reflectivity, measured with an InfraSnow prototype (Gergely et al., 2014) as shown in Figure 2.7. Density and LWC were measured using a dielectric sensor (Denoth, 1994)(FPGA Company GmbH, 2018). On occasions when the snow was dry, which was indicated by snow temperatures below 0 °C, the density was measured. When snow melting started, the increase in the dielectric number of the snow was measured to deduce the LWC (Denoth, 1994). PR was measured using a Swiss Rammsonde with an adapted penetration body ($d = 15$ mm; cone angle = 60°) for groomed snow (Fierz et al., 2009; Wolfsperger et al., 2018). PR was calculated from the energy of a weight ($m_{dyn} = 1$ kg) falling from 0.5 m (h_{fall}) onto the penetration body, which then penetrated the snow by the depth s_{dyn} that was measured. Applying the energy restitution law and including the static weight of the ram penetrometer ($m_{stat} = 1.744$ kg), PR was calculated according to Equation 2.7.

$$PR = \frac{m_{dyn} \cdot g \cdot h_{fall}}{s_{dyn}} + m_{stat} \cdot g \quad (2.7)$$

In order to reduce the dimensions of the snow parameter space T_{ss} and LWC were merged to $TLWC$. For negative snow temperatures, $TLWC$ equals the snow temperature. For snow temperatures of 0 °C, $TLWC$ equals LWC . Merging snow temperature and LWC appeared possible, as they have a defined physical relationship: Liquid water in snow can only be present for snow temperatures of 0 °C, while sub-zero snow temperatures physically stipulate a LWC of 0 %. The snow was visually classified into the main grain shape classes (Fierz et al., 2009) and photographed (DigiMicroscope LCD, Reflecta GmbH, D) on a grid board (1 mm) with a magnification of 20 (Fig. A1 to A6). Each snow measurement was conducted three to 5 times to capture the measurements' uncertainty (Table 3), which mainly was a consequence of the inherent variability of the gliding track's snow surface, but also the result of random, unknown sources of error. The values of the instantaneous snow property measurements during the day were time interpolated to match them to the COF measured at the exact time of the run. For the time interpolation of the values, first and second order polynomials were used

for ρ_s and SSA , as well as smoothing spline approximations for $TLWC$ and PR . The root mean square error (RMSE) of the fit was used to quantify the uncertainty of the measured snow properties. Depending on the snow conditions the uncertainties differed between test days. Beyond the availability of suitable measurement methods, the described snow physical quantities were selected as they allowed to describe the different aspects of snow as a material with sufficient completeness. Thus, it was possible to allocate snow of any type and state to a unique point in the snow parameter space. In snow science, the snow type is defined by its microstructure and density, whereas the snow state is defined by snow temperature, LWC and hardness (Fierz et al., 2009). For the natural snowpack, correlations between those attributes clearly exist (e.g. there is now natural snow layer of high SSA and density), whereas at the surface of a ski slope those natural correlations are partially cancelled due to grooming and skiing. Although correlations still can occur even on slopes, there are no strict dependencies over the whole range of two parameters. For example, new snow generally has low density and hardness, but high-density snow, e.g. wet spring snow, is not necessarily hard. In that case, adding the LWC as parameter is sufficient to explain the low hardness due melted and weakened grain bonds.

In addition to the measurable snow parameters, a categorical approach was used to describe the snow conditions. The snow was categorized as spring-, winter- and new snow, referring to typical snow types, with three sub-categories referring either to T_{ss} (cold < -13 °C, mid = -7 to -13 °C, warm > -7 °C) or to LWC (dry = 0 %, wet = 3 to 8 %, very wet = 8 to 15 %), which added information about the state of the snow (Table 2.3). Whether the snow was categorized as spring snow or winter snow was not related to the time of year, but to the shape of the snow grains. Spring snow consists of so-called melt forms (Fig. A6), caused by melt-freeze cycles, which typically occur in spring with warm days and cold nights.



Figure 2.7: Instruments used to measure the snow properties: InfraSnow (top left), Dielectric sensors for *LWC* measurements (top right) and density (bottom left), and the adapted Swiss Rammsonde (bottom right).

Table 2.3: Snow conditions on each test day: Colloquially described, classified after Fierz et al. (2009), and quantified by the daily range ($T\text{LWC}$) or mean ($\pm sd$) of the measured snow physical properties. HN24 (HN72) describes the height of fallen new snow during the past 24 (72) hours.

date	snow description	grain shape and grain size (mm)	days last snow-fall (HN24, HN72)	since snow-fall (HN24, HN72)	$T\text{LWC}_{\min}$ (°C)	$T\text{LWC}_{\max}$ (°C) / (%)	ρ_s (kg m ⁻³)	SSA (mm ⁻¹)	PR (N)
2017-03-30	spring snow	MFcl (MFpc), 1	8 (8, 8 cm)	-0.5	6.0	451 ± 25	6 ± 0	82 ± 45	
2017-03-31	spring snow	MFpc (MFcl), 1.5	9 (8, 8 cm)	-1.5	5.1	474 ± 34	8 ± 0	146 ± 102	
2018-02-01	new snow dry	DF (PPsd) rimed, 0.25-2	5 (2, 2 cm)	-7.5	-7.0	159 ± 41	82 ± 6	95 ± 29	
2018-02-07	winter snow warm	RG, 0.25	3 (1, 18 cm)	-7.2	-2.8	430 ± 36	11 ± 3	136 ± 30	
2018-02-08	winter snow mid/new snow dry	RG (DF), 0.5-1	0 (1, 1 cm)	-9.7	-8.2	292 ± 45	61 ± 14	104 ± 20	
2018-02-13	winter snow cold	RG (FC), 0.25-0.5	0 (3, 19 cm)	-17.8	-13.0	280 ± 27	37 ± 19	104 ± 17	
2018-02-21	winter snow mid	FC (RG), 0.5	0 (4, 4 cm)	-13.4	-8.3	332 ± 53	40 ± 9	67 ± 16	
2018-02-22	winter snow mid/cold	FC (RG), 0.5	1 (0, 4 cm)	-14.3	-6.9	429 ± 25	17 ± 3	113 ± 34	
2018-03-03	winter snow warm	DF (RG), 0.5	0 (7, 10 cm)	-6.6	-4.8	349 ± 27	44 ± 16	91 ± 28	
2018-03-04	winter snow mid/warm	RG (FC), 0.25-0.5	0 (4, 14 cm)	-10.2	-4.4	339 ± 25	31 ± 10	132 ± 47	
2018-03-28	new snow dry/wet	MF (DF), 0.5	0 (9, 12 cm)	-0.4	10.2	451 ± 31	38 ± 9	104 ± 28	
2018-04-06	spring snow	MFpc, 0.75-3	4 (1, 11 cm)	-7.5	5.7	503 ± 19	5 ± 0	142 ± 118	
2018-04-08	spring snow	MFpc, 14	6 (1, 11 cm)	-2.3	11.9	412 ± 12	3 ± 0	136 ± 115	

2.2.2.5 Data analysis

The following subchapter is part of the publication: Wolfsperger, F., Meyer, F., Gilgien, M., 2021. The snow-friction of freestyle skis and snowboards predicted from snow physical quantities. *Frontiers in Mechanical Engineering*, 7, 728722.

The COF-curves of the runs with sufficiently valid data were analyzed in four different ways: (1) To provide the range of the *COF* and an overall average observed over all runs; (2) To give estimates of *COF* for different categories of snow conditions to relate them to the *COF* in the simplest way; (3) To investigate the influence of speed on the *COF*; and (4) To understand how the *COF* depended on the measured snow and/or weather parameters.

Mean values ($\pm sd$) of the *COF* for single runs were calculated by averaging the COF-curve over speeds from 5 m s^{-1} to 15 m s^{-1} . Depending on the slope of the test track and the snow friction, the analyzed sections were approximately 50 m to 230 m long. Those parts of the COF-curve below 5 m s^{-1} and above 15 m s^{-1} were discarded from the analysis, since the COF-curves of consecutive runs increasingly deviated from each other in those sections. Directly after the start (ca. 4 m from the start), deviations were attributed to body movements while getting into the predefined skiing posture which distorted the velocity vector, and to the process of ski alignment movements, when moving off. At higher speeds, aerodynamic forces gain greatly in importance compared to ski-snow friction, creating increasing uncertainty in the measured *COF*. Overall COF-means ($\pm sd$) were calculated for the group of skiers and snowboarders from the mean values of all single runs. An unpaired two-sided T-test was conducted to compare the overall COF-averages of the two groups. Estimates of *COF* for different categories of snow conditions were calculated by averaging the COF-curves over two to 6 consecutive runs for which the snow conditions were constant.

The snow categories were also used to group runs from the different test days for the speed dependency analysis. The average COF-speed-curves were plotted and compared qualitatively and quantitatively at four points along the track: at the end of the starting section (after 4 m of gliding; COF_{start}); at the COF minima (COF_{min}); and at speeds of 10 m s^{-1} and 15 m s^{-1} (COF_{10} , COF_{15}), where these were reached. The speed dependency was quantified by the COF-difference between two points, divided by the corresponding speed difference.

To determine whether *COF* depended on the snow properties, the COF-mean values were first fitted (least squares) using single parameter regression for each of the different snow parameters. Since the predictive power of these single parameter models turned out to be weak, backwards stepwise multiple regression (least squares) models were applied to parametrize the *COF* to all snow property measures (explanatory variables). In addition, an alternative 4-parameter model was calculated using T_{air} , T_{ss} , RH and the grain shape class, which are quantities commonly assessed by ski technicians and require less measurement equipment, time and know-how. Starting from a model containing an intercept, linear terms, interactions, and squared terms for each predictor, terms were removed stepwise if the sum of the squared errors was significantly changed by the removal (F-Test with $p < 0.05$).

2.2.2.6 Uncertainties in the COF field measurements

The following subchapter, including Table 2.4, is part of the publication: Wolfsperger, F., Meyer, F., Gilgien, M., 2021. The snow-friction of freestyle skis and snowboards predicted from snow physical quantities. *Frontiers in Mechanical Engineering*, 7, 728722.

To estimate the uncertainty in the *COF* measured on-field, two approaches were used. (1) The measured variability of the *COF* was analyzed. First, the *COF*-fluctuation throughout the analyzed section of a single run was quantified by the coefficient of variance $COV_{COF} = sd_{COF}/COF_{mean} \cdot 100$. Second, the reproducibility of several consecutive runs, for which the snow conditions were constant, was analyzed. An average *COF*-speed curve with error bands of $\pm 1\text{ sd}$ was calculated for five consecutive runs on two test days where the highest (February 13) and the lowest (March 4) reproducibility among all test days was achieved. Reproducibility was indicated by the mean width of the error bands throughout the analyzed section (5 to 15 m s^{-1}). (2) The Gaussian equation for the propagation of normally distributed errors was applied, as the *COF* values were calculated from several measured quantities, which had uncertainties likely to propagate to the result. This approach helped to understand how strongly the different terms of Equation 2.5 contributed to the *COF* uncertainty. In the first step, the uncertainties of the components of the gravitational (ΔF_{Gx} , ΔF_{Gz}), aerodynamic (ΔF_D , ΔF_L) and inertial forces ($\Delta(m \cdot a)$, ΔF_{FGx} , ΔF_R) were calculated (Eq. 2.8) assuming a constant speed of 10 m s^{-1} and average values for x_i in the force functions ($m = 80\text{ kg}$; $a = 1.69\text{ m s}^{-2}$; $\alpha = 16^\circ$; $\kappa^{-1} = 100\text{ m}$; $c_D A = 0.529$; $c_L A = 0.224$; $\rho_{air} = 1\text{ kg m}^{-3}$; $v_{wind} = 1\text{ m s}^{-1}$; $T_{air} = 0^\circ\text{C}$). The uncertainties Δx_i of the input quantities x_i were given by the measurement system, estimated, or calculated if they were deduced from other quantities, e.g. the air density (Table 2.4). For velocity and acceleration, the uncertainties were determined by the RMSE between the raw signal (position data smoothing only) and the fully smoothed signal used for force calculations.

$$\Delta F(x_1, \dots, x_i) = \sqrt{\sum_{i=1}^{i=n} \left(\frac{\delta F}{\delta x_i} \cdot \Delta x_i \right)^2} \quad (2.8)$$

The sums of the corresponding force components' uncertainties gave the total uncertainty of the friction force (ΔF_F) and normal force (ΔF_N) (Eqs 2.9, 2.10). The relative uncertainty of the *COF* was then derived from the sum of the relative uncertainties of F_F and F_N (Eq. 2.11).

$$\Delta F_F = \Delta F_{Gx} + \Delta F_D + \Delta(m \cdot a) \quad (2.9)$$

$$\Delta F_N = \Delta F_{Gz} + \Delta F_L + \Delta F_R \quad (2.10)$$

$$\frac{\Delta COF}{COF} = \frac{\Delta F_F}{F_F} + \frac{\Delta F_N}{F_N} \quad (2.11)$$

With regard to the multivariate COF-models, the uncertainties of the *COF* and snow property measurements, as well as the uncertainty of the multivariate regression model itself, were considered. The propagated uncertainties from the snow measurements to the modeled *COF* were calculated using Equation 2.9, but using the regression functions 3.1 and 3.2 instead of the force functions. The uncertainties of the models were expressed in the RMSE of the regression. Finally, all uncertainties were added to yield the total uncertainty of the modeled COF.

Table 2.4: Values and explanations of the assumed uncertainties of the measured and deduced input quantities.

measured input quantity	uncertainty value	comment	deduced input quantity	uncertainty value	comment
position	± 0.02 m	dGNSS accuracy	radius (κ^{-1})	± 0.04 m	propagated from velocity & position uncertainty
			velocity	± 0.08 m s^{-1}	RMSE smoothed vs. raw signal
			acceleration	± 0.09 m s^{-2}	
			slope	$\pm 0.22^\circ$	propagated from velocity uncertainty
mass	± 1 kg	assumption			
drag area	± 0.027 m^2	assumed as 5 % of drag / lift area			
lift area	± 0.011 m^2				
wind velocity	± 0.2 m s^{-1}	RMSE smoothed vs. raw signal	relative air velocity	0.28 m s^{-1}	sum of wind & athlete velocity uncertainty
atmospheric pressure	± 105 hPa	probable diurnal variation	air density	0.05 kg m^{-3}	propagated from variation of T_{air} and p_{atm}
air temperature	± 5 $^\circ$ C				
relative humidity	± 0 %	neglectable			

2.3 Slider-snow friction laboratory experiments

2.3.1 Research design

The design of the laboratory experiments resulted from the set focus on the ski/SB-snow friction at the transition from dry, over moist to wet and very wet snow. This was done because here, the strongest changes of the material properties of snow, and consequently of ski/SB-snow friction, were assumed. Later this assumption was confirmed in the field study (chapter 3.1) but it was also shown that the *COF* on melting snow cannot be well explained by its *LWC* alone. A key to understand those results was assumed in the extent and mode of deformation of the snow's solid (ice) phase, and how that impacted the solid-to-solid *RCA*, as well as the liquid water within the snow and its occurrence at the ski-snow interface. Additional motivation to focus the dry-to-wet snow friction transition was given due to the fact, that it has been poorly studied so far, and also has gained increasing practical relevance with on-going climate warming (Hock et al., 2022; Scott et al., 2023).

As a consequence of the research questions, the laboratory part of this study consisted of four types of experiments. (1) Friction measurements on a short distance linear snow tribometer, aiming to compare the laboratory set-up of a down-scaled ski-snow tribosystem with the reality as captured by the field experiments concerning the *COF* and its snow dependency. (2) Compression tests of snow applying skiing-like pressure to reveal the mode and extent of the snow deformation representing the ski-snow macroscopic contact mechanics. (3) Investigation of liquid water accumulation and redistribution in proximity of the slider-snow interface due to load and compression during the slider contact using a capacitive sensor. (4) Estimations of the microscopic *RCA* of the ski-snow contact using x-ray micro computer tomography (μ CT) measurements.

2.3.2 Snow preparation and characterization

The SSA measurement method as described in the second part of the third paragraph were described in more detailed within the poster publication: Wolfsperger, F., Ziegler, S., Schneebeli, M., Löwe, H., 2022. Evaluation of the InfraSnow: a handheld device to measure snow specific surface (SSA). International Symposium on Snow 2022, Davos. Presented on 26th Sept..

The snow sample preparation primarily aimed to mimic the range of snow characteristics found during the field experiments and focused those snow parameters, which showed the largest effect on the *COF* on the field. Therefore, snow samples' *SSA* and *TLWC* were altered systematically using different preparation methods as described below. In addition, the snow samples had to have a certain compressive strength to withstand the normal loads during testing and they had to be prepared in a highly reproducible manner.



Figure 2.8: Fine-grained snow samples after a series of compression experiments.

Thereto, cylindrical snow samples ($d = 60$ mm, $h = 13.2$ to 20.0 mm) were prepared using nature identical new snow (Schleef, 2014) or ice powder as base material. If using the latter, ice was grinded and sieved with three different mesh-sizes revealing fine (< 0.71 mm), mid (0.71 to 1.5 mm) and coarse-grained (1.5 to 2 mm) ice powder. After storing at -25 °C for several days the slightly sintered ice powders were sieved (1.4 mm) into the cylindrical sample holders, followed by compression of 1 to 5 mm at speed of 0.1 mm/min (Autograph AGS-X, Shimadzu Europe GmbH, D) to adjust the snow density (ρ_s) to realistic values as observed on the field (Fig. 2.8). Afterwards, the snow samples were rested for sintering at -3 °C for around 12 to 20 hours.

Two hours before the experiments, the samples were taken out from the colder sintering chamber to adapt to the air temperature of the test laboratory of -1 °C. Within this period the snow samples height and mass were measured to calculate ρ_s . The different snow types were characterized by their mean densities, standard deviations, and COV_ρ , which are given in the result section. Moreover, the SSA was measured for 3 samples of each snow type. Mean SSA , standard deviation and the average COV_{SSA} over all snow types were calculated to characterize the snow samples microstructure and their variability. In contrast to the field measurements, SSA was measured with a prototype of the new InfraSnow device applying the same measurement principles as described in chapter 2.2.2.4. Although the new InfraSnow devices were developed in closest correspondence to the old prototype used for the field campaign based on the validation by Gergely et al. (2014), several optimizations concerning mechanical components and electronics were implemented. Therefore, the validity of the un-

derlying numerical model, which describes the relation of measured near-infrared-reflectance and the snow's *SSA* and density, had to be verified. This required to conduct optical simulations considering the new sensor specifications and comparisons with the old prototype and *SSA* measurements from μ CT and other optical methods. This detailed evaluation of the InfraSnow method was partly published (Wolfsperger et al., 2022) and can be found in full detail in the appendix. In addition to the described ρ_s and *SSA* measurements, those parameters were also deduced from μ CT scans (MicroCT80, Scanco Medical AG, CH) of single snow samples in dry state, as well as after being refrozen from wet state. Both, ρ_s and *SSA* were calculated as averages of the density and *SSA* profiles as described in chapter 2.3.6.

In a final step of snow sample preparation, the *TLWC* was adjusted from -1 $^{\circ}\text{C}$ up to a maximum of 14.7 % by applying infrared light (Osram Thera RD 150 W) for different times of exposure (0 to 72 s) directly before each experiment. The average *LWC* of the entire snow sample was deduced for the different exposure times and snow samples by melting calorimetry using an in-house built device made of a thermos bottle and a PT1000 temperature probe (GHM 2710, GHM Messtechnik GmbH, D) as presented by Kawashima et al. (1998). According to Equation 2.12 the latent heat of melting of the ice fraction of the snow sample was calculated revealing the *LWC* in mass percent.

$$LWC_{mass\%} = 1 - \frac{c_w}{Q_L} \cdot \left[\frac{m_w}{m_s} \cdot (T_w - T_{ws}) - T_{ws} \right] \quad (2.12)$$

Where c_w is the specific heat of water (4.186 $\text{kJ kg}^{-1} \text{K}^{-1}$), m_w is the mass of water in the calorimeter, m_s the mass of the snow sample, T_w the water temperature before the snow sample was put into the calorimeter, and T_{ws} the mixing temperature of snow and water after complete melting. Including the measured snow density of the sample and the known density of water ρ_w the volumetric *LWC* was revealed as follows:

$$LWC_{vol.\%} = LWC_{mass\%} \cdot \frac{\rho_s}{\rho_w} \quad (2.13)$$

Those destructive *LWC* measurement were done separately from the other tests with additional, but identically prepared snow samples. Depending on the samples *SSA* and ρ_s , same exposure times lead to different *LWC* as the snow samples albedo were different. The reproducibility of the method, which included also variations within the snow sample wetness preparation, was about ± 0.3 vol.%, quantified by the standard deviation from 6 identical measurements at an average *LWC* of 6.5 vol.%.

2.3.3 Snow tribometry

The methodology described in this subchapter, excluding all Figures, was first presented in the following publication: Wolfsperger, F., Szabo, D., Rhyner, H., 2020. How to glide well on wet snow? Can roughness and hydrophobicity lower friction of polymers on snow? *Gliding* (2), 6-14. The method's measurement uncertainty as revealed in the named publication was used in this thesis (see third paragraph).

The COF measured on the field corresponded to speeds between 5 and 15 $m\ s^{-1}$. From the speed range and the skis' running length of 1.41 m (Table 2.1) resulted the duration of loading of the snow when gliding over it of about 0.28 to 0.09 s (including loading and unloading). Including the deformation of the snow, which was estimated between 0.5 and 10 mm, a vertical speed of snow deformation from about 0.004 to 0.21 $m\ s^{-1}$ could be assumed. The average normal pressure underneath a ski was about 5.7 kPa. As far as possible, the tribological measurements in the laboratory were aligned with the kinematics and kinetics of the real skiing situation. This could be achieved in the vertical, but not in horizontal direction, where the speeds were one to two orders of magnitude smaller than at the field tests.

The experiments were performed on a linear friction tester placed in a cold chamber where air temperature was kept at -1 °C. The device consisted of two position or force controlled linear drives. A vertical drive was programmed to press the slider onto the snow sample with a constant speed of 0.01 $m\ s^{-1}$ until reaching a vertical force F_z of 56.3 ± 0.4 N, representing a skiing-like pressure of about 19.9 ± 0.15 kPa. This was followed by a horizontal movement of 106 mm with a constant horizontal velocity 0.1 $m\ s^{-1}$ to induce friction between the slider and snow sample and let the slider entirely pass over the snow sample. Although, by that, the snow samples yielded at the end of the experiments, the friction force signal was not disturbed by an early deceleration to stop the slider being still in full contact with the snow sample (Fig. 2.9 to 2.11).

The slider (90 x 70 mm) consisted of a sintered UHMWPE ski base ($E \approx 600$ MPa), which was glued to an aluminum sample holder. The gliding surface was stone grinded using a ski-sized grinding adapter to be able to grind the small slider in the same way as a ski. Afterwards the slider was waxed with the same hydrocarbon wax as used for the field tests (see chapter 2.2.1). Roughness parameter and contact angles were measured similarly as described for the used skis on the field (see chapter 2.2.1) and are summarized in Table 2.5. A new snow sample had to be used for every measurement. Vertical and horizontal forces were measured with 100 kHz sampling rate and 0.1 N resolution by a force plate, placed under the snow sample (Kistler Model 9254, CH). The displacement was measured with the same sampling rate with 1 μm spatial resolution by a linear encoder (Renishaw, UK). The snow surface temperature of the snow samples was measured with an infrared thermometer (Optris LS, E2006-01-A).

Static (COF_{stat}) and kinetic friction coefficients (COF_{kin}) were measured on dry snow at close to zero (-0.5 to -1 °C) snow temperatures and on snow at the melting point containing different amounts of liquid water. The measurement uncertainty, determined as the standard

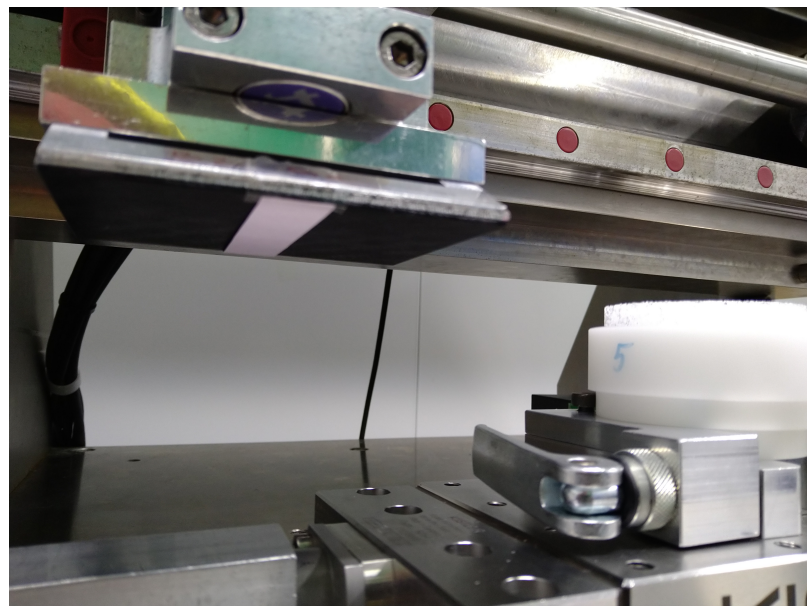


Figure 2.9: Linear friction tester with the mounted UHMWPE slider. The mounted pink strap was not used for compression or friction tests (see chapter 4).

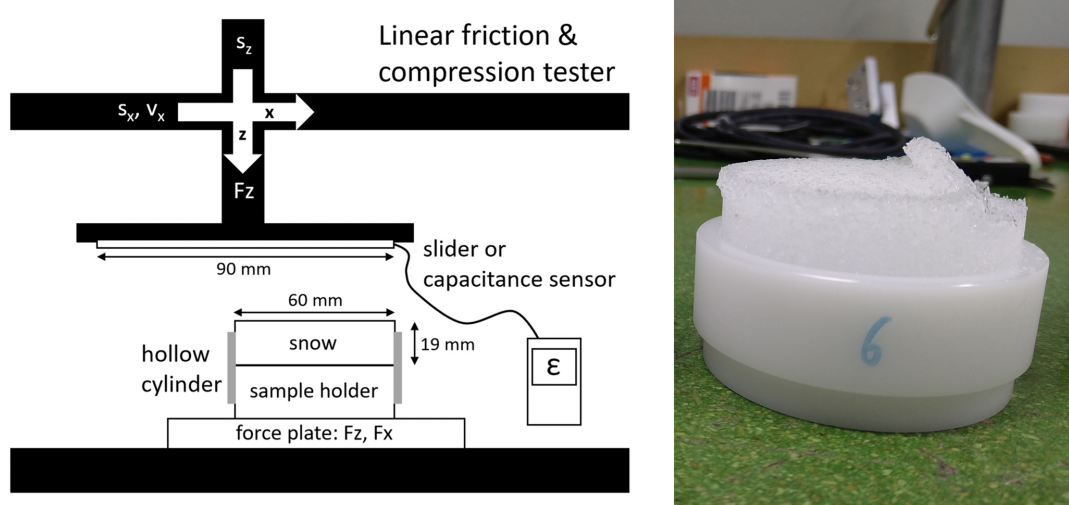


Figure 2.10: Left) Sketch of the laboratory setup for friction and compression tests. Right) A broken snow sample after a friction test.

deviation of multiple identical measurements ($n = 3$ to 10) of the static (kinetic) COF were 13.7% (12.5%) for dry snow, and 7.3% (5.8%) on wet snow as reveled in former experiments (Wolfsperger et al., 2020). Mean COF were calculated from the COF -time raw data curves (Fig. 2.11). COF_{stat} could clearly be identified in the COF -curve as a significant maximum just after the horizontal movement has started. The kinetic friction was defined as the averaged COF -curve over 0.4 seconds starting at the local minimum directly after dropping down from the static friction maximum (Fig. 2.11).

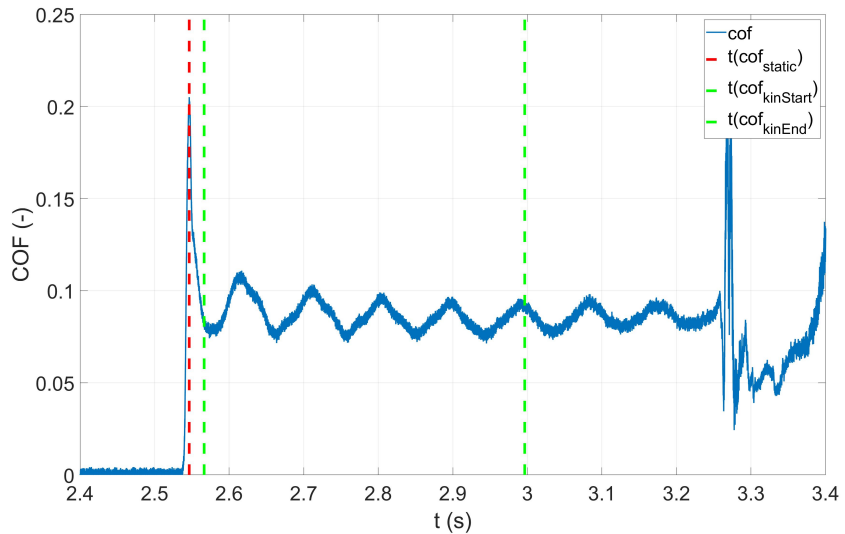


Figure 2.11: Exemplarily COF -curve of a single snow friction measurement starting with a distinct peak (static friction), followed by oscillations on a constant level (kinetic friction) until the snow sample partly collapsed. The coefficient of kinetic friction was calculated as average between the green lines. The oscillations were assumably a result of the strong starting acceleration.

Table 2.5: Properties of the UHMWPE slider including surface roughness parameters ($n = 5$) and dynamic contact angles of distilled water ($n = 7$). The advancing (receding) angle is the contact angle which occurs in the course of wetting (de-wetting) of the ski base.

UHMWPE - slider		
mean peak-to-valley height R_z (μm)	27.9	± 2.9
mean width of profile elements R_{Sm} (μm)	339.0	± 55.9
profile skewness R_{sk} (μm)	-1.1	± 0.2
advancing angle unwaxed ($^\circ$)	92.3	± 3.8
receding angle unwaxed ($^\circ$)	43.2	± 8.6
advancing angle waxed ($^\circ$)	98.4	± 4.2
receding angle waxed ($^\circ$)	72.7	± 3.6

2.3.4 Snow macro-mechanical characterization under compression

A key to understand why snow friction can be very different depending on the snow conditions was to quantify the snow conditions by its physical properties. In contrast to the field experiments, the laboratory infrastructure provided the possibility for mechanical testing of similar snow samples as used for the tribological experiments. The macro-mechanical interaction of a ski with snow influences the ski-snow friction assumably from three sides:

- 1) The resistance of a ski due to snow compaction and plowing.
- 2) The size and the number microscopic contacts between ski and snow (shape, number, force distribution per grain) as the surface grains are assumed to get rearranged when snow yields under the skiers' load.
- 3) The redistribution of water in the pore space of wet snow during such deformations which might affect water accumulations at the ski-snow interface.

To quantify the changing material behavior of different types and states of snow under skiing-like loading, confined compression tests were done with the same device and similarly prepared snow samples as for the friction tests (Fig. 2.9 & 2.10). The snow samples were compressed ($F_1(s)$) with a constant speed of 0.01 m s^{-1} until reaching a force of about 56 N, which was similar as for the friction experiments. The load was kept constant for a short period (0.4 to 1.3 s) depending on the extend of snow deformation until reaching the desired force. This represented the loading dynamics of a skiing speed of about 1 to 4 m s^{-1} (assuming a loaded ski base length of 1.5 m). Due to the different compressibility of wet and dry snow samples and the limited power of the vertical drive, the realized strain rates of dry and wet snow samples deviated from each other ($\dot{\epsilon}_{dry} = 0.29 \pm 0.05 \text{ s}^{-1}$; $\dot{\epsilon}_{wet} = 0.44 \pm 0.05 \text{ s}^{-1}$). A second compression test ($F_2(s)$) was conducted of each snow sample 60 s after unloading to distinguish the permanent brittle and plastic from viscoelastic snow deformation.

The deformation of the snow during the slider-snow contact was characterized by the different modes of deformation (elastic, viscoelastic, permanent brittle and plastic) and its fractions on the total deformation ($s_{elastic}/s_{total}$; $s_{viscoel.}/s_{total}$; $s_{plastic}/s_{total}$), the work used to permanently deform the snow, the snow strength during compression, as well as the snow's rheology under a short static load. The snow deformation during compression was assumed to be dominated by brittle deformation (grain bond failure) as expected from high strain rates above the ductile-to brittle transition of snow and ice (chapter 1.1.1). For dry snow this was also indicated by the crispy force signal during loading (Fig. 2.13 left). Whereas, for wet snow the force signal smoothed indicating a more ductile-like behavior (Fig. 2.13 right). The measured deformations could be distinguished between permanent and reversible elastic and viscoelastic ones. A differentiation between permanent brittle, (instantaneous) plastic and viscoplastic deformations (assumably at small contact spots of ice grains) was not possible based on the measurement data. However, fitting a rheological Burger model allowed the estimation of the time-dependent viscoplastic deformation fraction as explained in detail below.



Figure 2.12: Two fine-grained snow samples after a compression test.

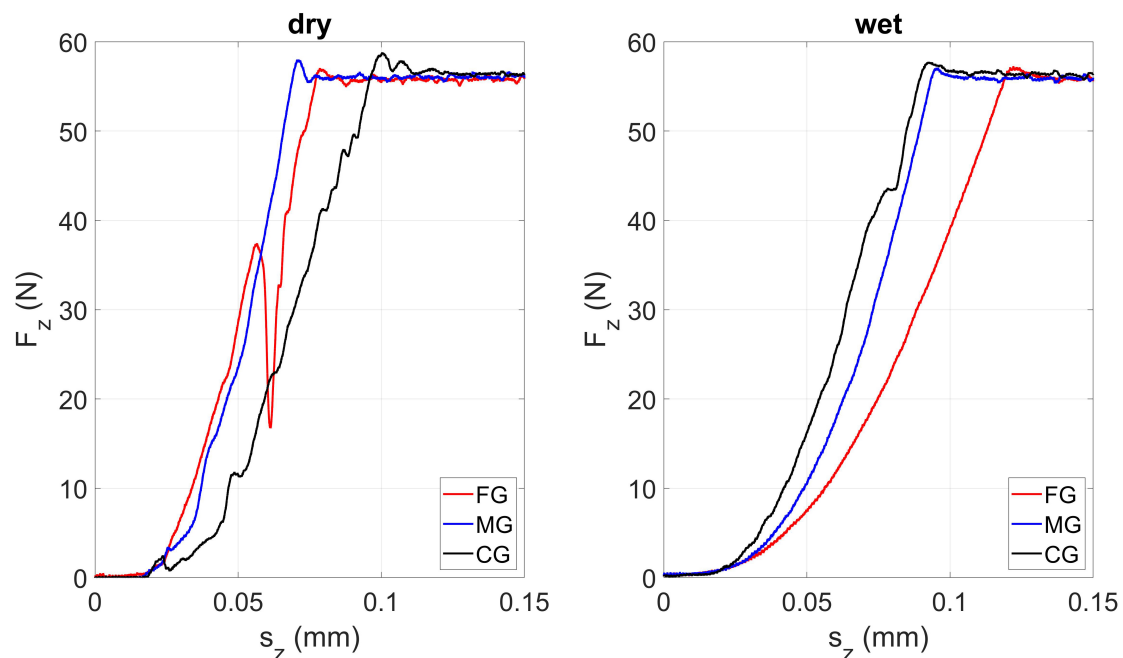


Figure 2.13: Force-displacement raw signals of the compression of dry and wet FG, MG and CG snow samples.

The parameters listed above were revealed from two consecutively measured force-displacement curves with their characteristic loading and unloading phases. The loading phase was divided into three sections to analyze the snow deformation in detail as exemplarily shown in Fig. 2.14 (top) and described in the following:

Section 1 was defined to start with the initial contact ($F_z = 0.5$ N) from where on contacts between the multiple snow surface grains and the slider were build up. This was shown as a slight rise of the force curve over about 0.1 to 0.5 mm. The snow deformation within this section was dominated by brittle failure of single surface grain bonds.

Section 2 was defined by a subsequent linear and much steeper rise of the force curve (Fig. 2.14 top - green line). This section was defined as that part of the force curve, achieving the highest determination of a linear fit ($R_{adj}^2 > 0.995$). During this section the entire snow sample was loaded and compressed equally over the whole snow sample top surface (apparent contact area). The snow deformation was again assumed to be dominated by grain bond failure, but now this happened at many locations concurrently, causing an ongoing compaction related with a linear increase of force. Those multiple loops of bond failures and pore space collapse were understood as a quasi-plastic collapse process where snow density equilibrates with compressive bulk stress (Mellor, 1975). The quasi-plastic compression modulus K_p as calculated in Equation 2.14 was used to quantify the snow strength in that phase of loading. Curves of K_p typically stabilized on a constant level throughout this second section of loading (Fig. 2.14 middle). The average K_p was therefore used as the major parameter to quantify the macro-mechanical properties of the different snow types during this phase of the contact.

$$K_p = \rho_s \cdot \frac{d\sigma}{d\rho_s} = \frac{d\sigma}{\frac{d\rho_s}{\rho_s}} \quad (2.14)$$

During section 3, the loading rate decelerated until the load became static at its maximum, representing the pressure underneath a ski. Assuming, in first approximation, a frustum shaped pressure distribution underneath a ski (Mössner et al., 2023), snow below that ski would experience such a constant stress loading phase during a certain time depending on the speed and the length of the ski. As shown in Figure 2.14 (top) the force reached a plateau, but the snow deformation continued under constant loading indicating the viscous material behavior of snow. To describe the combined elastic, viscoelastic and viscoplastic deformation under constant stress, a Burger model was fitted to the measured strain ϵ from the time of maximal load to the time of maximal deformation as shown in Equation 2.15 and Figure 2.14 (bottom).

$$\epsilon = \sigma_o \cdot \left[\frac{1}{E_M} + \frac{t}{\eta_M} + \frac{1}{E_{KV}} \cdot \left(1 - e^{-\frac{E_{KV}}{\eta_{KV}} \cdot t} \right) \right] \quad (2.15)$$

The Burger model is a rheological model consisting of a parallel spring E_{KV} and dashpot

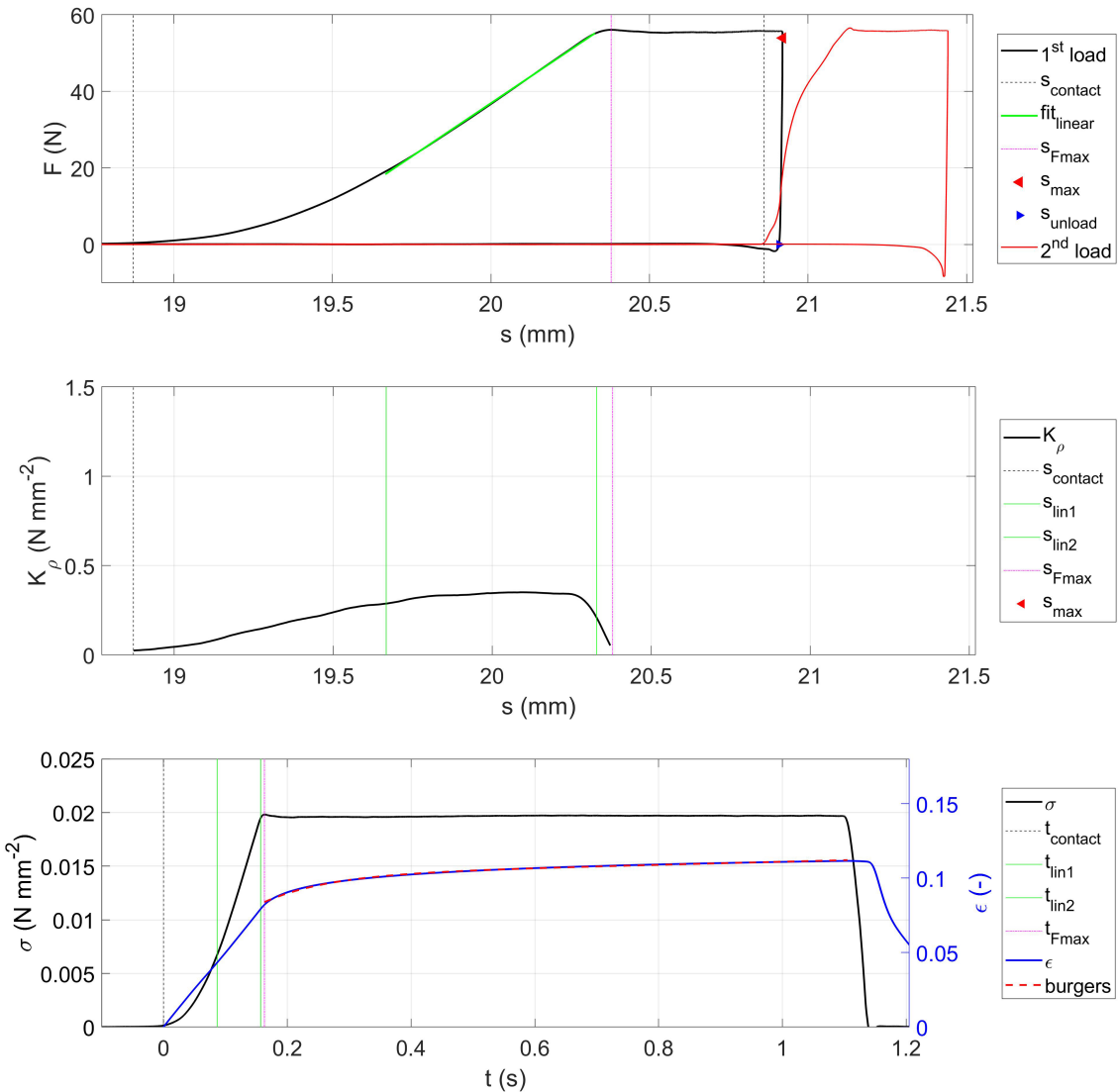


Figure 2.14: Top) Measured force and distance of two consecutive compression tests of a wet ($LWC = 7\%$) fine-grained snow sample including loading and unloading. Middle) Calculated compression module of the first compression experiment, which was averaged throughout the linear section of the force curve marked by the green vertical lines. Bottom) Stress σ , strain and its fit (Burger model) during the period of constant stress of the first compression test.

η_{KV} element (Kelvin-Voigt element), which is combined with a spring E_M and a dashpot η_M , connected in series (Maxwell element). The abrupt elastic deformation after loading is represented by the serial spring E_M . Here, the model interpreted all deformations before loading phase 3 as elastic. As explained before, such deformations could be better characterized with a quasi-plastic compression modulus. Therefore, E_M was not taken into consideration. The focus within this third loading phase were on the following viscoplastic and viscoelastic deformations, which were represented in the model with a serial dashpot as linearly time-dependent deformations, and by the Kelvin-Voigt element describing the change in viscoelastic deformation with an exponential decay.

The loading was followed by the phase of unloading which started from the maximal snow deflection s_{max} and ended when the force came to zero at s_{unload} revealing the elastic deformation $s_{elastic}$ (Eq. 2.16). In some wet snow sample experiments the unloading was followed by slight tensile (negative) force due to adhesion between the slider and the wet snow. The distance between the initial contact at the first loading and s_{max} revealed the total deformation (Eq. 2.17). The distance between the initial contact at the second loading (s_{cntct2}) and the position when the first load became zero (s_{unload}) revealed the viscoelastic deformation $s_{elastic}$ (Eq. 2.18). The permanent deformation was revealed from the distance between the initial contacts of the first (s_{cntct1}) and the second (s_{cntct1}) loading cycle (Eq. 2.19). The loading and unloading curves of the first and second compression and their overlap revealed the total work of permanent deformation w_{def} as formulated in Equation 2.20.

$$s_{elastic} = s_{max} - s_{unload} \quad (2.16)$$

$$s_{total} = s_{max} - s_{cntct1} \quad (2.17)$$

$$s_{velastic} = s_{unload} - s_{cntct2} \quad (2.18)$$

$$s_{plastic} = s_{cntct2} - s_{cntct1} \quad (2.19)$$

$$w_{def} = \int_{s_{cntct1}}^{s_{max}} F_1(s) \cdot ds - \int_{s_{unload}}^{s_{max}} F_2(s) \cdot ds - \left(\int_{s_{cntct2}}^{s_{intrcpt}} F_2(s) \cdot ds - \int_{s_{unload}}^{s_{intrcpt}} F_1(s) \cdot ds \right) \quad (2.20)$$

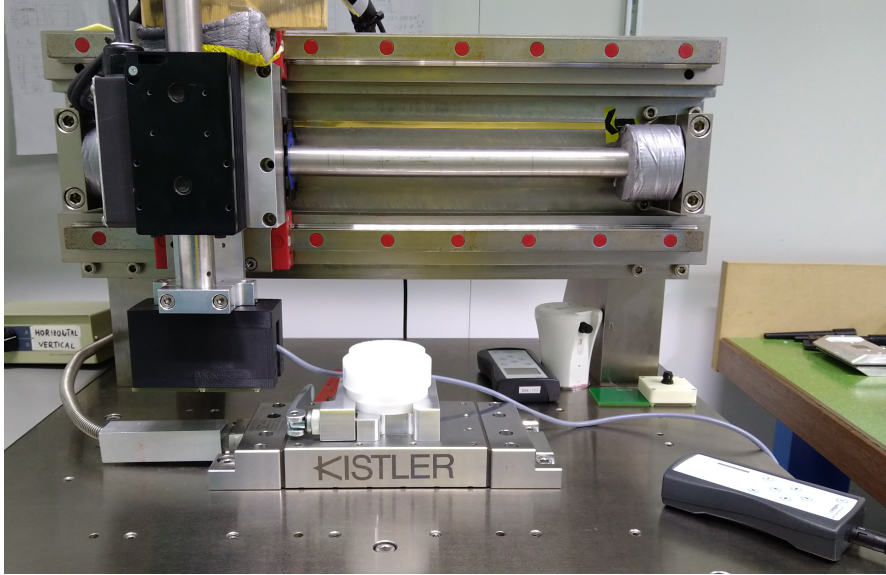


Figure 2.15: Setup of compression tests of snow samples using a co-planar capacitive sensor to monitor of liquid water accumulation at the slider-snow interface.

2.3.5 Snow liquid water redistribution under compression

The ski-snow friction is known to be strongly affected by the amount of liquid water at the ski-snow interface (e.g. Colbeck, 1992). It can be assumed that on wet snow, the amount of water at the interface is not only determined by the prevailing *LWC* of the snow and melt water from frictional heat. Beyond that, snow deformation together with the morphology of the collapsing pore space during the compressive contact is assumed to affect the amount of water at the interface. The here conducted experiments aimed to answer, to what extent liquid water within the snow gets redistributed and accumulated at proximity of the slider-snow interface during the ski-snow contact.

Therefore, a method was developed to estimate the amount of liquid water in proximity of the slider-snow interface. Compression tests were performed similarly as described in the previous chapter (2.3.5), but the slider was replaced by a co-planar capacitive sensor (FPGA Company GmbH, SLF Snow Sensor, CH), which generated an electrical field (20 MHz) permeating the snow sample every 10 milliseconds (Fig. 2.15). The measured sensor capacitance during compression quantified changes of the snow's relative permittivity ε_r^s (also known as dielectric constant), which gave information on the degree of water accumulation in proximity of the snow-sensor interface.

Using capacitive sensors to measure ρ_s or *LWC* of snow (so-called dielectric method) was first introduced by Armin Denoth (1989). The measurement principle uses the fact that air, ice and water significantly differ in the real component of their relative permittivity for

frequencies from 0.01 to 1 GHz ($\varepsilon_r^{ice} = 3.2$; $\varepsilon_r^{water} = 88.3$). In consequence, depending on the volume fractions of ice, air and water within a snow volume, the measured capacitance changes. Measurements on calibration materials with known ε_r (e.g. pure ice, air, PTFE) reveal the proportionality factor to calculate ε_r^s from the measured capacitance. If ρ_s or LWC is aimed to be deduced from ε_r^s , one of either volume fractions of ice or water must be known from additional measurements. Moreover, as the volume fractions do not linearly contribute to ε_r^s , empirical ρ_s/LWC - ε_r^s -correlations (Denoth, 1989; FPGA Company GmbH, 2018) or dielectric mixing models are required (Niang et al., 2006). However, both approaches assume homogeneous distributions of ice, air, and water within the permeated snow volume. This was not the case for wet snow samples in this study, as the liquid water was generated by melting, starting at the sample's top surface, and continuing deeper into the snow sample with increasing infrared-light exposure time.

For heterogeneously distributed water within the snow, ε_r^s depends on the sensitivity distribution of the capacitive sensor, which is determined by geometry and flux density of the sensors' electric field. Typically for co-planar sensors the sensitivity drops exponentially with increasing distance from the electrodes (Hu and Yang, 2010; Hu et al., 2022). Therefore, the amount of liquid water within a defined distance to the sensor could not exactly be quantified. However, considering the typical sensitivity distribution for co-planar sensors, it could be assumed that the higher the permittivity was measured, the more water and the closer to the interface it was. Therefore, the method allowed to describe changes of water concentration in proximity of the interface during a ski-like compressive contact, and regarding this, enabled to investigate the differences between the snow types.

To monitor the water and its redistribution within the different snow types during compression, the relative permittivity at initial sensor contact ε_{cntc} and when fully loaded ε_{cmp} were compared ($\Delta\varepsilon = \varepsilon_{cmp} - \varepsilon_{cntc}$), together with the corresponding compression distances ($\Delta s = s_{cntc} - s_{cmp}$) as shown in Fig. 2.16. To eliminate the permittivity contributions of the solid phase (ice) as good as possible, the relative permittivity of dry snow ε_{dry} were subtracted from the one of wet snow ε_{wet} . However, as the wet snow samples experienced larger deformations, the densifications of the solid phase at the top layers could not be completely retracted. Beyond that, all measurements were corrected with a zero measurement, which measured the capacitance of an empty snow sample holder to distract signal contributions of the sidewalls, its base, as well as of the sensor holder.

The sensor was developed in close cooperation of SLF and FPGA Company GmbH (Ziegler, 2005, 2006, FPGA Company GmbH, 2018), and launched in 2018. For this study a high sampling mode ($f = 100$ Hz) was implemented for laboratory applications, which is available since 2023 (firmware version 2.3). The sensor has a measurement volume of approximately $45 \times 70 \times 17$ mm, which was slightly larger than the snow samples, both horizontally, as well as in height. Therefore, even for homogeneous distributions of the snow sample constituents, the existing sensor calibrations for LWC and ρ_s were not valid. The material of the sensor is a glass fibre epoxy compound (FR-4 PCB laminate).

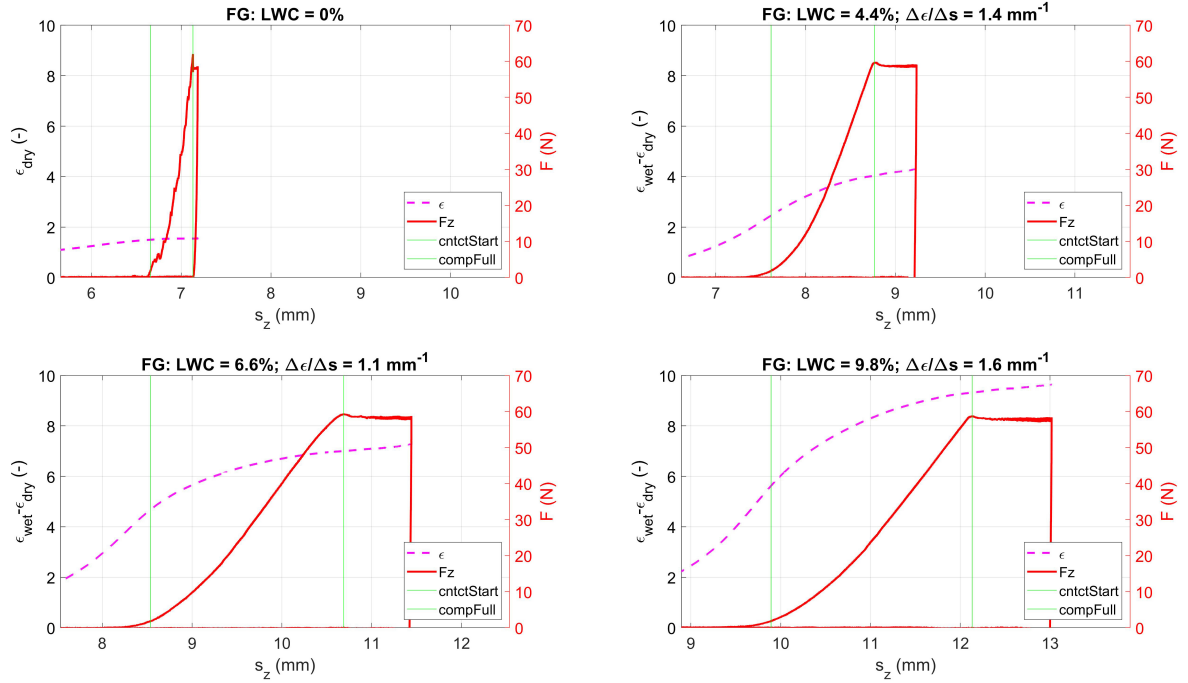


Figure 2.16: Permittivity measurements (dashed, magenta) and compression force (red) over compression distance of fine-grained (FG) dry (top left) and wet snow with increasing LWC (top right to bottom left). The vertical lines in green mark the height at initial sensor-snow contact and at full compression. Corresponding graphs for mid and coarse-grained snow can be found in the appendix.

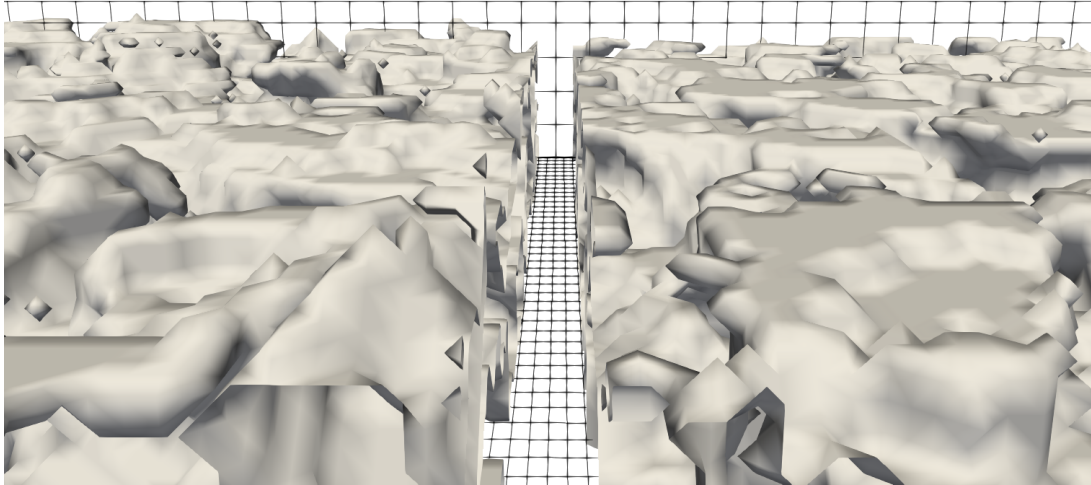


Figure 2.17: Comparison of two snow sample sub-volumes (ca. $9 \times 9 \times 0.9$ mm) before (left) and after (right) the slider contact visualized as 3D surface mesh models. Due to the slider contact, the sample surface on the left side is more equally leveled and has more flat surface features within the same horizontal plane.

2.3.6 RCA estimation and snow morphological changes

μ CT-scans (MicroCT80, Scanco Medical AG, CH) were carried out to analyze morphological changes of the snow as a result of the slider contact, as well as to analyze the snow surface topography and estimate the *RCA* and its dependence on type and state of the snow. As snow samples failed during the friction experiments, the μ CT-scans were done with snow samples from the compression tests as described in section 2.3.4. Snow samples in dry and several wet states were scanned before (pre: FG, MG) and after (post: all types) the contact. Liquid water within the wet snow samples was refrozen before the scans, as it anyway could not have been distinguished from the solid phase (ice) by x-ray computer tomography. Beyond that, it prevented the samples from wet snow metamorphism during the duration (ca. 8 hours) of the scan (voxel = 0.018^3 mm 3 , volume $\approx 40 \times 40 \times 20$ mm).

The raw data revealed from the μ CT-scans were segmented applying the segmentation method established by Hagenmüller et al. (2016), followed by a two-fold analysis: (1) To analyze the morphological changes of the snow, density profiles over the complete sample height were calculated based on the revealed μ CT voxel model (averaged over horizontal slices of $18 \times 18 \times 0.4$ mm with 0.08 mm vertical overlap). (2) To analyze the snow surface topography, the μ CT voxel model of the snow was down-sampled ($5 \times 5 \times 5$ voxels; ParaView 5.11.0-RC2: paraview.simple.ExtractSubset) revealing a xyz-resolution of 0.045 mm, which helped to focus those microstructural features relevant for the *RCA* estimation. Subsets ($18 \times 18 \times 1.7$ mm) of the down-sampled voxel model were then used to generate a surface mesh using a contour filter algorithm (ParaView 5.11.0-RC2: paraviews.simple.Contour).

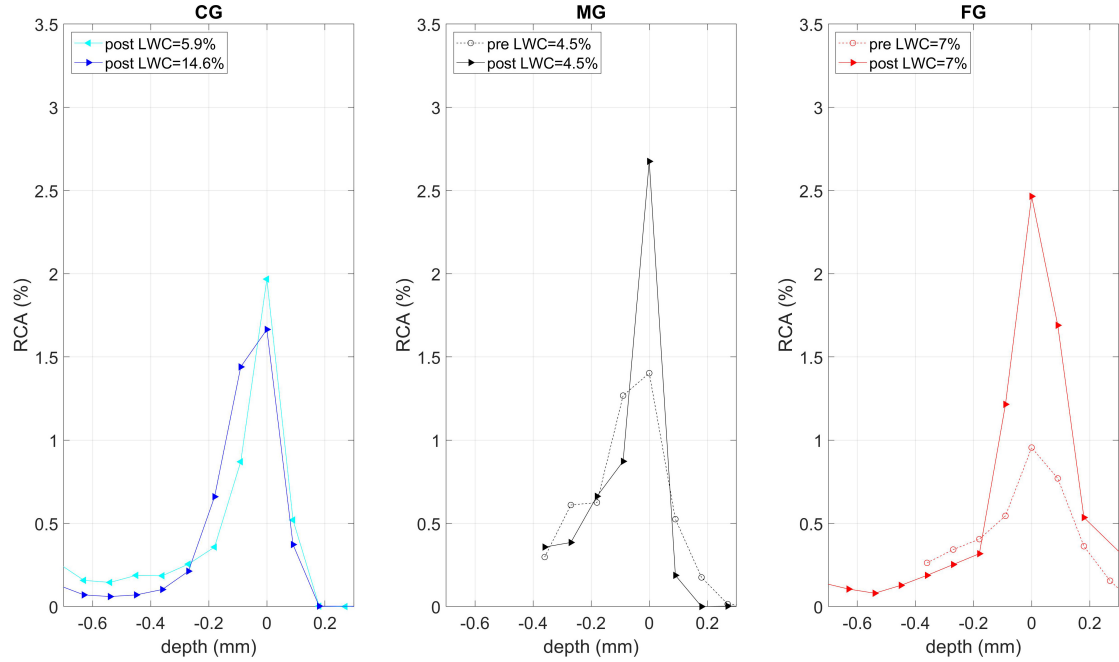


Figure 2.18: Frequencies of flat (horizontal) surface elements along the depth of the meshed snow sample microstructure 3D representation revealed from μ CT-scans.

To detect those features of the snow surface, which had assumably been in contact with the slider, surface elements of four sub-volumes ($9 \times 9 \times 1$ mm) of each snow sample were analyzed by their slope and their number in each horizontal plane (which could be assumed to be parallel to the slider-snow interface). Due to the flattening of the snow surface during the slider-snow contact (Fig. 2.17 left), the number of surface elements in the discretized horizontal planes of the mesh model showed a pronounced peak at a certain height level, compared to before the contact as visible in Figure 2.18 for MG and FG snow. The height level of the horizontal plane with the highest number of flat surface elements was interpreted as the slider-snow interface plane and was set to zero. The RCA_{rel} estimate (assuming a perfectly smooth slider) was then calculated from the sum of flat surface elements (slope $< 10^\circ$) located in the three adjacent horizontal planes, below, above and at the zero level, divided by the cross-section area. The surface topography and the spots of the RCA (black pixels) were visualized plotting 2D colormaps of the snow surface top view, where the contact plane was defined as zero depth ($z = 0$ mm). Deduced from the visualized snow surface with contact spots, the number of contact grains were estimated from manual counting.

Flat surface elements of adjacent planes were included because they appeared to be a result of the slider contact. Moreover, analyzing the RCA variability among the four sub-volumes of each sample, the inclusion of adjacent planes appeared to be a more robust proxy for RCA than using the peak level alone. It can be assumed that the reason for that were limited planarity of the horizontal planes of CT data and the real surfaces of slider and snow, and/or

elasticity and viscoelastic relaxation of the surface after the contact, and/or surface elevations from refrozen water on the contact spots.

However, the RCA_{rel} were clearly shifted towards larger values by including more than the zero plane. This indicated that the external validity of the method was limited, and due to a missing reference method this limitation was not able to be further evaluated. However, concerning the methods reproducibility, a first approximation was given by the scatter of the four independent (no overlap) sub-volumes, which were separately analyzed from each snow sample surface. As shown in the results (see chapter 3.2.5) this scatter was smaller than the differences found between the different snow types. Consequently, the method was used to compare RCA_{rel} estimates related to different types and states of snow.

3 Results

3.1 Ski/Snowboard-snow friction field measurements

The following subchapter 3.1 including all Figures and Tables is part of the publication: Wolsperger, F., Meyer, F., Gilgien, M., 2021. The snow-friction of freestyle skis and snowboards predicted from snow physical quantities. Frontiers in Mechanical Engineering, 7, 728722.

3.1.1 Friction coefficients for skiing and snowboarding

For skiers (snowboarders), average COF over a single run ranged from 0.023 ± 0.006 (0.026 ± 0.008) to 0.139 ± 0.018 (0.143 ± 0.017) (Fig. 3.2, 3.3). The average COF over all runs and conditions was about 0.054 ± 0.018 ($n = 114$ runs) for the skiers, and 0.060 ± 0.020 ($n = 100$ runs) for the snowboarders. The higher overall snow friction for snowboarders compared to the skiers, although statistically significant ($p = 0.008$), was rather small (ca. 12 %) compared to the huge changes in friction caused by different snow conditions (up to 430 %).

On dry, hard frozen spring snow, skiers and snowboarders (values stated in brackets) were clearly fastest, with low COF ranging between 0.026 ± 0.004 (0.031 ± 0.004) and 0.037 ± 0.001 (0.034 ± 0.001) (Table 3.1). With increased snow melting, gliding became slower, reaching the highest COF of 0.082 ± 0.006 (0.072 ± 0.004) on very wet spring snow (Fig. 3.1; Table 3.1). On winter snow, the data showed optimal gliding (minimal COF) at mid to warm snow temperatures with COF of 0.042 ± 0.001 for skiers and 0.049 ± 0.003 for snowboarders. On cold winter snow, which was only measured for skiers, the COF increased up to 0.059 ± 0.001 . Not surprisingly, the “slowest” conditions were observed on new snow. For skiers, on new snow (freshly groomed) the lowest COF was 0.060 ± 0.008 at close to zero snow temperatures. During the same day, COF -values drastically increased up to 0.138 ± 0.015 , due to intensive melting, which illustrates the well-known stickiness of very wet new snow (Fig. 3.1). During heavy snowfalls, COF of 0.079 ± 0.007 were found for skiers. Unfortunately, no snowboard runs were conducted during days with heavy snow fall. For snowboarders, only a slight snowfall event was captured, revealing a COF of 0.059 ± 0.001 (Table 3.1).

The above overview provides an insight into how snow friction changes with different snow

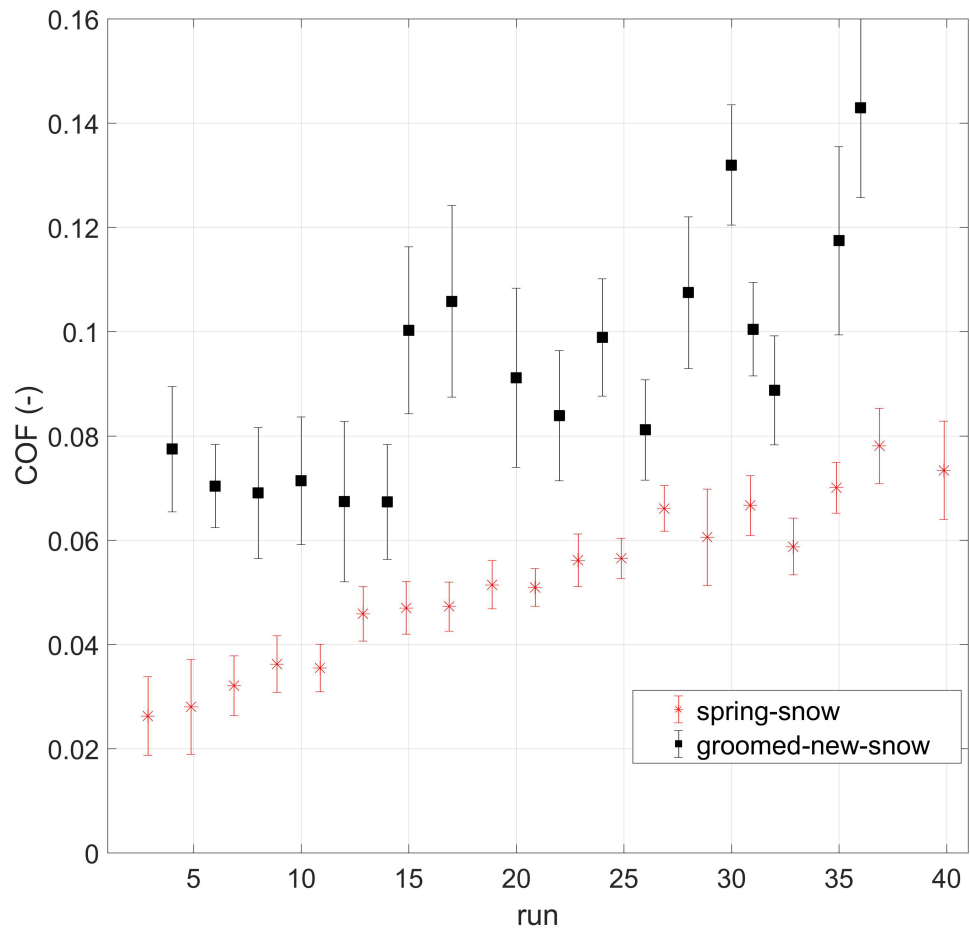


Figure 3.1: COF (mean \pm sd) of consecutive snowboard runs throughout a test day (ca. 9:00 to 15:00) on spring snow (18/04/08), and on groomed new snow (18/03/28) with increasing LWC from 0 % to ca. 10 %. The consecutive numbering of the runs also includes runs performed by skiers which are not plotted.

categories, which group similar types and states of snow. The results showed that variations in both categorical dimensions affected the *COF*. The strongest effect occurred when the state of spring snow changed from dry to very wet, which tripled snow friction within a test day (Fig. 3.1). However, using a categorical approach to link snow conditions to *COF*-values has limitations, as the snow is not described in its full complexity. This might explain why a distinct scatter of the *COF* was revealed within the same snow categories (Table 3.1). Therefore, further snow, weather, or process parameters and their interactions were included in the analysis to determine whether a more precise prediction of the friction of skis and snowboards on snow can be achieved.

3.1.2 Parametrizations of snow friction with snow physical properties

Beyond the snow-specific quantification of snow friction related to a system of ten snow categories, measurable and continuous scaled physical quantities to describe the snow more objectively and accurately were used. This approach aimed to gain a better understanding of the underlying mechanisms behind snow friction and to create a better method of predicting snow friction. This included the idea that any type of snow can be adequately described using five quantities: temperature, *LWC*, density, *SSA*, and penetration resistance. Moreover, linking snow friction to physical snow properties allows the application of snowpack models (Lehning et al., 2006; Hanzer et al., 2020) to forecast snow friction, as a function of weather scenarios and topographies for any ski slope or slopestyle course, worldwide.

Although the *COF* could not be accurately determined from a single snow property alone ($R^2 = 0.04$ to 0.29), single parameter models mostly revealed plausible dependencies and predicted realistic *COF* ranges (ca. 0.02 to 0.10 as means of entire runs). High *COF* were predicted for high *LWC*-values, while low *COF* were especially predicted on hard snow as quantified by a high penetration resistance (Fig. 3.2, 3.3). For skiers in particular, the influence of the snow's *SSA* and density on the *COF* corresponded to what practitioners would expect: snow with a high *SSA* makes gliding slower, e.g. a thin layer of new snow crystals on the track. In contrast, a high-density track, such as a very compacted winter snow slope, usually facilitates fast gliding. For the snowboarders, single parameter models showed a lower degree of determination ($R^2 = 0.04$ to 0.16) and *PR* appeared to be the only useful parameter for predicting the *COF*, although its predictive power was still rather low. In summary, it was found that single parameter models could not sufficiently determine snow friction, since considerable interactions between the snow parameters were assumed. For example, high snow density can be a result of intense melting, which leads to soft snow with a high *LWC* causing high snow friction, as reported in chapter 3.1. However, high snow densities at subzero snow temperatures can involve hard snow with no liquid water content, which causes low snow friction, an aspect that is widely known and shown above. Therefore, the predictive powers of models including multiple snow parameters and their interactions were assessed.

Multivariate models for the *COF* had distinctively higher explanatory power than the single

Table 3.1: Friction coefficients averaged over 2 to 6 consecutive runs with constant snow conditions, categorized into spring, winter and new snow with different snow temperature or snow wetness sub-categories. The overall COF (mean \pm sd) were averaged from 5 to 15 $m\ s^{-1}$. Instantaneous COF -values at the start (after 4 m of gliding; COF_{start}), when reaching the minimum COF (COF_{min}), at 10 $m\ s^{-1}$ (COF_{10}), 15 $m\ s^{-1}$ (COF_{15}) and at maximum speed (COF_{max}), provide information on the COF -speed dependency.

sport	snow description	$COF_{overall}$	COF_{start}	COF_{min}	COF_{10}	COF_{15}	COF_{max}	v_{cofmin}	v_{max}	n	T_s (°C)	LWC (%)	date
SK1	dry	0.026 \pm 0.004	0.064	0.016	0.025	0.023	0.072	8.0	18.4	4	-2...0 °C		2018-04-08
		0.028 \pm 0.004	0.070	0.019	0.027	0.025	0.048	7.5	17.2	6	-2...0 °C		2018-04-06
		0.037 \pm 0.001	0.105	0.036	0.037	0.038	0.035	8.1	22.9	2	-1...0 °C		2017-03-30
	spring snow	0.043 \pm 0.003	0.093	0.038	0.042	0.048	0.051	7.6	22.0	4	5...6 %		2017-03-30
	wet	0.044 \pm 0.005	0.070	0.045	0.043	0.076	7.4	16.6	3	5...8 %		2018-04-08	
		0.054 \pm 0.006	0.068	0.036	0.053	0.058	0.073	6.5	15.9	3	5...7 %		2018-04-06
winter snow	very wet	0.082 \pm 0.006	0.103	0.069	0.082	0.098	0.098	6.4	14.0	4	9...12 %		2018-04-08
	mid	0.042 \pm 0.001	0.100	0.040	0.040	0.044	0.063	10.5	20.7	2	-7...-3 °C		2018-02-22
		0.045 \pm 0.001	0.108	0.044	0.045	0.047	0.064	11.4	21.3	3	-8...-10 °C		2018-02-21
	cold	0.052 \pm 0.001	0.113	0.050	0.051	0.052	0.072	11.0	21.6	3	-14 °C		2018-02-22
		0.059 \pm 0.001	0.114	0.057	0.059	0.060	0.073	11.9	20.2	5	-15...-18 °C		2018-02-13
	dry	0.060 \pm 0.008	0.089	0.059	0.056	0.071	0.071	6.9	13.7	5	-1...0 °C		2018-03-28
new snow	dry (snowfall)	0.079 \pm 0.007	0.108	0.071	0.075	0.096	0.118	7.1	19.1	3	-7 °C		2018-02-01
	wet	0.087 \pm 0.010	0.088	0.066	0.078	0.104	0.104	7.7	11.8	3	3...4 %		2018-03-28
		0.138 \pm 0.015	0.115	0.102	0.133	0.133	0.133	5.1	8.35	1	8...9 %		2018-03-28
	dry	0.031 \pm 0.004	0.071	0.019	0.027	0.033	0.065	8.1	18.1	3	-2...0 °C		2018-04-08
		0.033 \pm 0.002	0.093	0.029	0.030	0.037	0.097	9.0	20.0	2	-2...0 °C		2017-01-31
		0.034 \pm 0.001	0.137	0.030	0.031	0.036	0.074	9.5	16.4	2	-2...0 °C		2018-04-06
SB	spring snow	0.049 \pm 0.003	0.069	0.039	0.051	0.052	0.074	7.1	16.8	3	7...8 %		2018-04-08
	wet	0.061 \pm 0.007	0.171	0.043	0.058	0.061	0.078	7.4	15.8	3	5...6 %		2018-04-06
		0.061 \pm 0.009	0.120	0.046	0.054	0.075	0.087	7.8	18.8	3	4...6 %		2017-03-31
	very wet	0.072 \pm 0.004	0.090	0.061	0.075	0.073	0.076	6.5	15.1	5	9...10 %		2018-04-08
	mid	0.049 \pm 0.003	0.100	0.043	0.047	0.055	0.065	7.3	21.4	4	-4...-5 °C		2018-03-04
		0.052 \pm 0.002	0.109	0.048	0.050	0.055	0.066	8.0	20.8	5	-6...-4 °C		2018-03-03
winter snow	dry (snowfall)	0.059 \pm 0.001	0.121	0.057	0.060	0.058	0.063	8.2	21.8	2	-10...-8 °C		2018-02-08
	dry	0.073 \pm 0.010	0.105	0.045	0.066	0.087	0.087	6.9	13.9	5	-1...0 °C		2018-03-28
	wet	0.097 \pm 0.014	0.095	0.061	0.100	0.120	0.120	6.4	11.8	4	3...4 %		2018-03-28
		0.110 \pm 0.011	0.101	0.076	0.104	0.109	0.109	6.1	11.4	3	5...8 %		2018-03-28
		0.136 \pm 0.014	0.106	0.098	0.140	0.140	0.140	4.5	8.7	2	9...10 %		2018-03-28

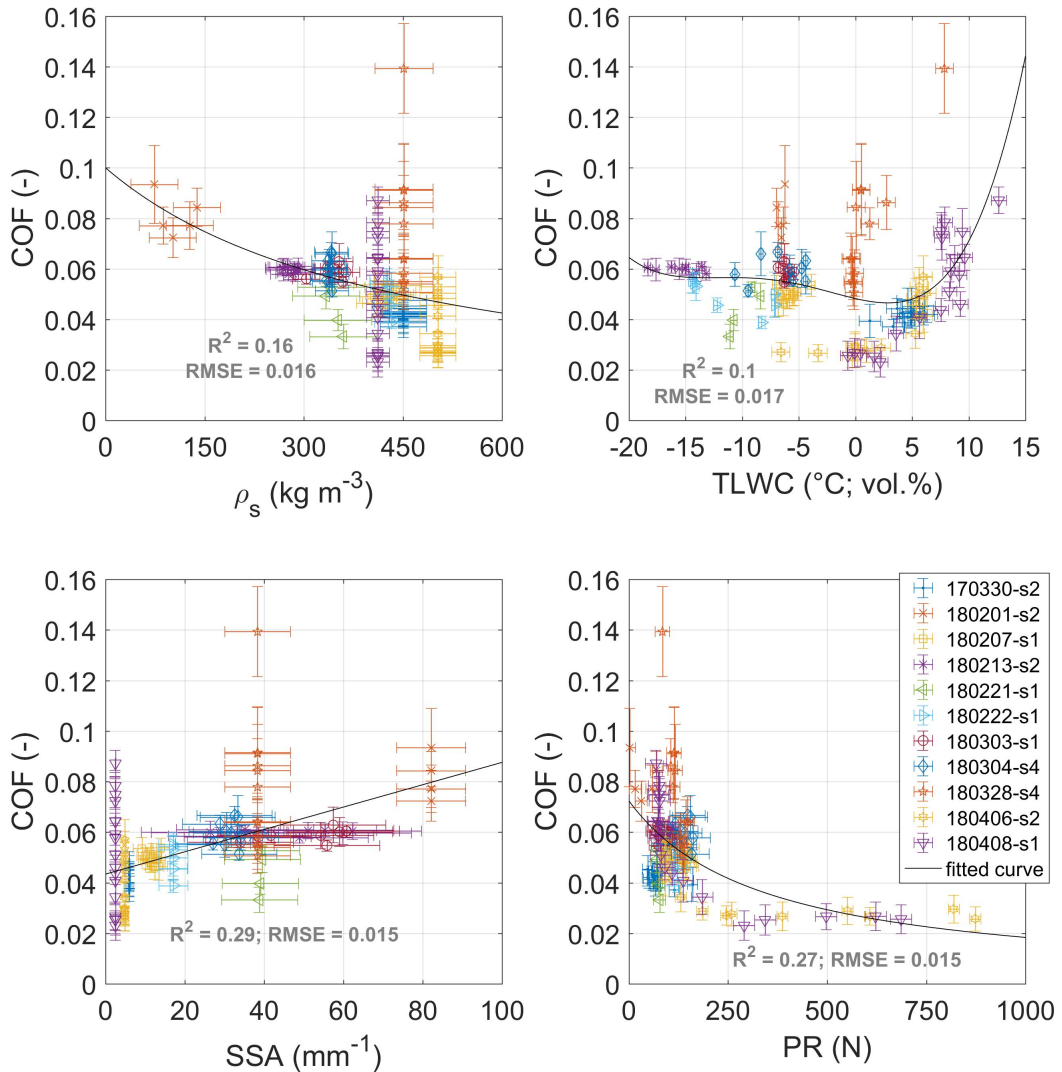


Figure 3.2: Mean ($\pm sd$) friction coefficients of all analyzed ($n = 114$) ski runs plotted versus the corresponding approximated snow properties (\pm RMSE) at the time of each run. Fitted curves represent single snow parameter models specified in the methods.

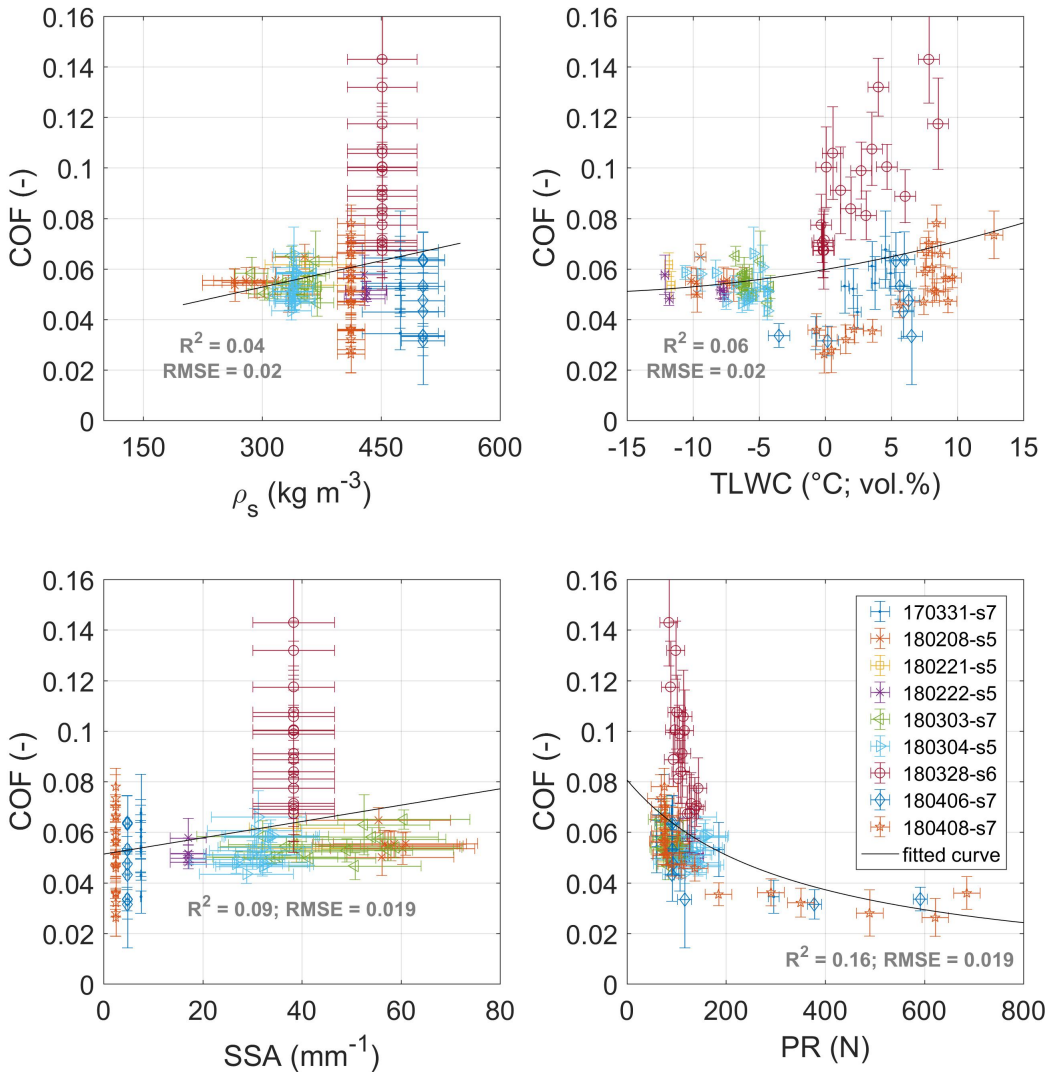


Figure 3.3: Mean (\pm *sd*) friction coefficients of all analyzed ($n = 100$) snowboard runs plotted versus the corresponding approximated snow properties (\pm RMSE) at the time of each run. Fitted curves represent single snow parameter models specified in the methods.

parameter models ($R^2_{adj_{SKI}} = 0.74$; $R^2_{adj_{SB}} = 0.77$; Fig. A7, A8), and RMSEs were reduced from about 0.016 to 0.009 for skiers and from 0.019 to 0.010 for snowboarders. For the skiers' COF-model, snow density was excluded a priori from the multivariate analysis, because density correlated considerably with *SSA* ($r_{pearson} = -0.79$; Fig. A9, A10), whereas density was the weaker predictor of the two in the univariate models ($R^2 = 0.16$ vs. 0.29; Fig. 3.2). The backward stepwise multivariate regression models produced, for skiers and snowboarders, linear terms for the *PR*, *SSA* and *TLWC*, a quadratic term for *TLWC*, and a mixed term for *SSA* and *TLWC*. In addition, the snowboarders' model included a weak quadratic *PR*-term and a mixed term for *PR* and *SSA*. In contrast, the skiers' model additionally included a mixed term for *PR* and *TLWC* (Eqs 3.1, 3.2). The most significant predictors were the *SSA* and *TLWC* and their interactions ($p < 0.001$). Although *PR* was not removed from the models by the backward iteration, its terms and interactions with *TLWC* (skiers) and *SSA* (snowboarders) were of lower significance ($p_{PR}^{ski} = 0.041$; $p_{PR/TLWC}^{ski} = 0.013$; $p_{PR}^{SB} = 0.030$; $p_{PR/SSA}^{SB} = 0.071$; Table A1).

The multivariate models were visualized by plotting the *COF* over *SSA* and *TLWC*, as they were the strongest and most significant predictors. *SSA* and *TLWC* can be understood as measures of the snow type and its thermal state, which supports the value of the snow categories introduced above (Table 3.1). For both groups, three plots are shown, for low, mid and high *PR*, which correspond to the 5-, 50-, and 95-percentiles of all *PR* measurements. All plots revealed similar patterns, with a *COF* peak for high *TLWC* and *SSA*-values and an area of minimal *COF* for low *SSA* and *TLWC* around zero. Interestingly, the models predicted low friction even for snow containing small amounts of liquid water. In the upper half of the plot, contour lines run from top left to the right showing how *SSA* and *TLWC* interacted: the higher the *SSA*, the more friction was affected by changes of temperature or *LWC*. For example, for a skier on coarse-grained spring snow with a low *SSA* (ca. 5 mm⁻¹), friction remained constant at a low level (0.03 to 0.04) over a wide span of *TLWC* (-8 °C to 2 %). In contrast, for snow with a high *SSA* (ca. 60 mm⁻¹), e.g. fragmented new snow particles compressed on an in-run after a few ski/snowboard runs, the same *TLWC* range corresponded to a much stronger *COF* increase (0.07 to 0.11) starting at a higher *COF* level. Following the vertical transects in the *COF* plots could help practitioners to predict changes in snow friction throughout a day, depending on the prevailing snow microstructure (*SSA*) and the expected diurnal warming and melting.

Snow hardness affected the modeled *COF* only if the *PR* shifted from mid to very high values (Fig. 3.4 b vs. c & e vs. f). The diagonal pattern in the upper half of the plots changed slightly to a more vertical pattern, indicating that *TLWC* influenced friction less on hard, warm to wet snow, while *SSA* gained importance. Moreover, the region of minimal friction was shifted upwards, to warmer or wetter snow conditions. In contrast, for lower temperatures at high *PR*, the skiers' *COF* model revealed *TLWC* as the dominating variable, visualized by a more horizontal pattern in the lower half of the plot (Fig. 3.4 c & f). The coexistence of wet and hard snow (high *LWC* and *PR*) is usually a contradictory parameter combination, as snow distinctively softens beyond a certain liquid water content (Fierz et al., 2009). Nevertheless, good examples of good gliding conditions with low *COF*, even when melting occurs, are

water-injected alpine ski racing slopes. Similar to wetness, hard snow with high *SSA* does not occur naturally, but can be produced artificially, to a certain extent. Machine-made snow can link *SSA*-values up to 25 mm⁻¹ with a high *PR* (Wolfsperger et al., 2014).

The comparison of the presented multivariate COF-model for ski with a multivariate model using a common set of explanatory variables (*T_{air}*, *T_{ss}*, *RH* and grain shape class) as used by ski technicians indicated that the latter has distinctively lower explanatory power ($R_{adj_{SKI}}^2 = 0.34$; $R_{adj_{SB}}^2 = 0.37$). This confirmed the benefit of using measurable physical quantities of snow to predict ski-snow friction.

$$COF_{SKI} = (295.441 - 0.142 \cdot PR + 11.825 \cdot SSA + 16.302 \cdot TLWC + 2.215 \cdot TLWC^2 - 0.088 \cdot PR \cdot TLWC + 0.921 \cdot SSA \cdot TLWC) \cdot 10^{-4} \quad (3.1)$$

$$COF_{SNB} = (483.430 - 1.155 \cdot PR + 0.001 \cdot PR^2 + 6.858 \cdot SSA + 0.802 \cdot TLWC + 1.973 \cdot TLWC^2 - 0.032 \cdot PR \cdot SSA + 1.175 \cdot SSA \cdot TLWC) \cdot 10^{-4} \quad (3.2)$$

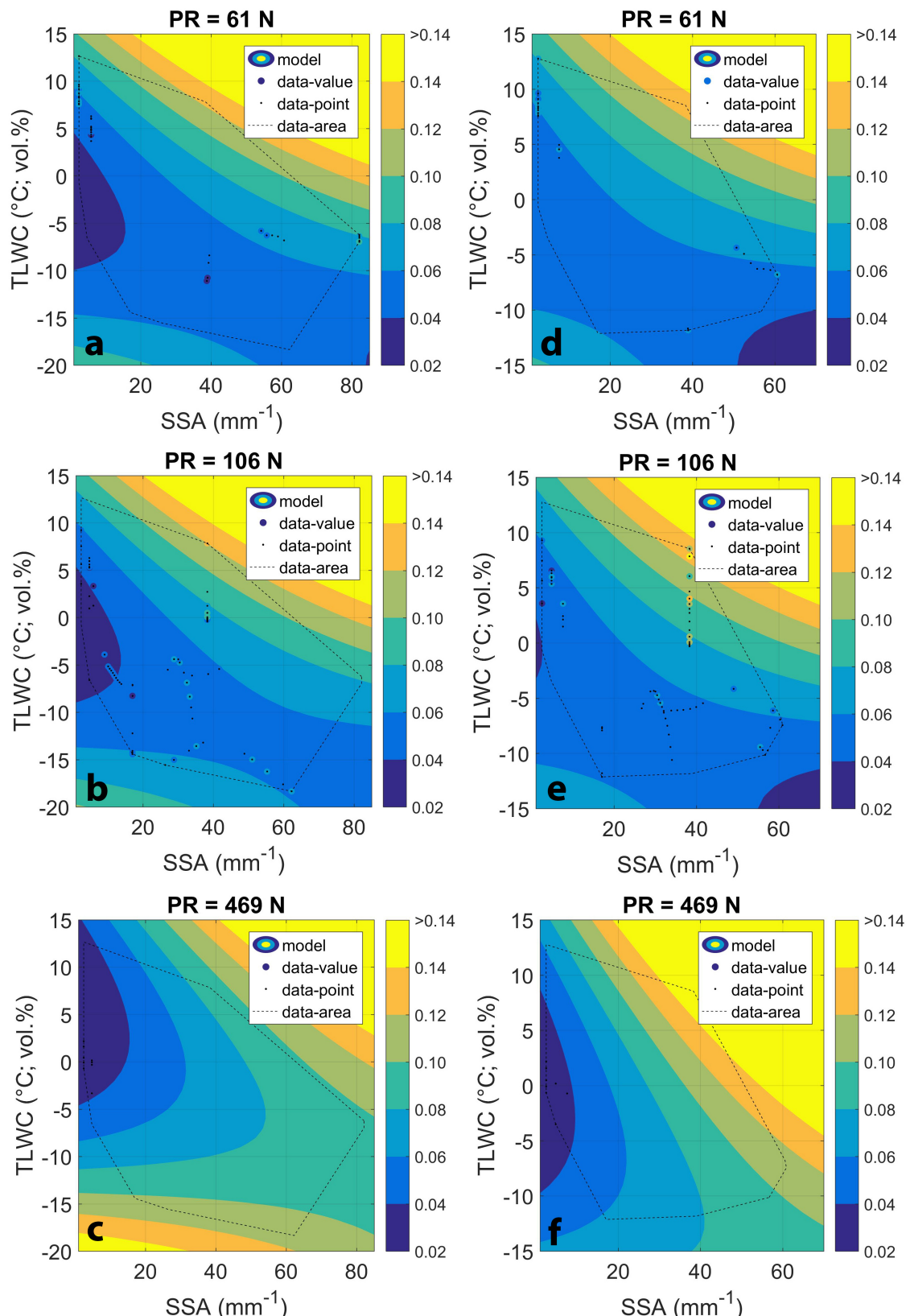


Figure 3.4: COF contour maps of skiers (a to c) and snowboarders (d to f) visualizing multivariate models of the COF-snow property relationship for low (top), mid and high (bottom) PR . The measured COF-values are visualized by small black dots revolved by larger filled circles (= 1 run). If the measurement (filled circle) has the same value (color) as the model (background), only the small black dot is visible.

3.1.3 Speed dependency of snow friction

The friction data presented in Figure 3.1 and Table 3.1 show average values over one run or a couple of similar runs. However, throughout a single run, snow friction was never entirely constant. Moreover, speed is known to be an important process parameter of tribological systems. Speed can increase or decrease friction and abrasion, depending on the prevalent friction regime. Due to the self-lubricating nature of snow friction, the influence of gliding speed on snow friction is particularly important.

The COF-speed curves showed a typical pattern for all runs (Fig. 3.5 a to f), starting with a strong COF-decrease over the first meters of gliding, quantified by the strong reduction from COF_{start} at 4 m to COF_{min} (Table 3.1) (note that 'start' refers to 4 m after the athlete moved off). With increasing speed, the COF stabilized at a fairly constant level (except on wet snow) until the speed reached about 15 m s^{-1} . These parts of the curves were specifically shaped, reflecting the different snow conditions during the tests. Both, the starting section (COF_{start} to COF_{min}) and the mid-section revealed clear COF-speed dependencies for both skis and snowboards. At lower speeds, from right after the start until reaching the COF-minimum (occurring between 3.3 and 7.9 m s^{-1}), a strong, negative speed dependency of the COF was found for all snow conditions (-0.012 ± 0.004 per m s^{-1}) (Table 3.1). At higher speeds (7.9 to 15 m s^{-1}), a clear positive speed dependency was found on wet to very wet spring snow (0.001 to 0.004 per m s^{-1}) and on groomed new snow (0.003 to 0.007 per m s^{-1}). At speeds beyond approximately 15 m s^{-1} the interpretation of the COF-speed curves became more difficult due to increasing noise caused by higher aerodynamic forces, which also led to enhanced posture variability in the athletes.

On winter snow, skiers' COF-minimum was reached relatively late, at an average speed of 11.5 m s^{-1} on cold snow and 9.8 m s^{-1} on mid-temperature to warm snow (Table 3.1; Fig. 3.5 a to b). The decrease in skiers' COF throughout those first meters of gliding was hence stronger on warm winter snow (-0.009 to -0.012 per m s^{-1}) than on cold winter snow (-0.006 to -0.008 per m s^{-1}). After that, skiers' COF stayed approximately constant on cold winter snow, while speed increased further (Fig. 3.5 d). In contrast, on warm winter snow, a slight increase in friction was measured as shown in Table 3.1 (0.001 to 0.002 per m s^{-1}). For snowboarders the COF-minimum on mid-temperature to warm winter snow was reached earlier (7.4 m s^{-1}) than for skiers but was then followed by the same slight increase in friction with increasing speed (0.001 to 0.002 per m s^{-1}).

On dry spring snow, snowboarders' and skiers' COF showed a strong decrease over the starting section (-0.011 to -0.019 per m s^{-1}) reaching very low COF-minima, followed by a distinct COF-increase until speed reached 10 to 12 m s^{-1} (Fig. 3.5 a). For most runs, a stagnation or even a decrease in the COF was observed, while accelerating to 15 m s^{-1} . With increasing snow wetness, not surprisingly, the COF-minimum was higher and was reached at lower speeds (ca. 6.5 m s^{-1}), the speed-COF relationship was more variable during the first meters (0.009 to 0.026 per m s^{-1}), and the COF-rise after passing the minimum was enhanced (0.001 to 0.004 per m s^{-1}) (Fig. 3.5 b).

For dry, groomed new snow, the COF-speed curves were shaped similarly to those for moist to wet spring snow. The *COF* decreased strongly after the start (-0.013 to -0.0018 per m s^{-1} on average), reached its minimum values quickly at low speeds (ca. 7 m s^{-1}), and was followed by a steep COF-increase (0.004 to 0.005 per m s^{-1}) until reaching maximum speeds of around 14 m s^{-1} (Fig. 3.5 e). When new snow became wet, the curves were shifted to higher COF-values and squeezed horizontally. The COF-decline over the first meters of gliding became smaller (-0.005 to -0.012 per m s^{-1}) and minimal friction values (ca. 0.01) were reached at about 5 m s^{-1} (Fig. 3.5 f). The following increase in friction was the strongest of all the tested snow conditions (0.006 to 0.011 per m s^{-1}), limiting athletes' maximum speed to about 12 m s^{-1} on wet and 8.5 m s^{-1} on very wet new snow. In contrast, during snowfalls, a more constant COF-speed curve without a pronounced increase after the COF-minimum (0 to 0.003 per m s^{-1}) was found, comparable to winter snow.

3.1.4 Measurement uncertainties

Throughout the averaged section of a single run, the COF-curves fluctuated by about $\pm 12 \text{ \%}$ on average, and in 95 \% of all runs were between $\pm 3.9 \text{ \%}$ and $\pm 23.5 \text{ \%}$. COF-variations over a single run could partly be explained by the observed speed dependency (Fig. 3.5 a to f), typically showing a COF-decrease at low speeds after starting off, followed by an increase at higher speeds. Comparing several consecutive runs under constant snow conditions revealed a varying reproducibility ranging from ± 0.001 ($\pm 2.4 \text{ \%}$; Fig. 3.6 a) to ± 0.006 ($\pm 10.4 \text{ \%}$; Fig. 3.6 b). The reproducibility clearly increased with decreasing wind and was higher on winter snow and on dry spring snow (Tables 2.2, 3.1).

The calculated COF-uncertainty, obtained from the input variables, turned out higher as the variability of the *COF* of consecutive runs shown in Figure 3.6. The relative uncertainty of the *COF* obtained from the input variables was $\pm 30.2 \text{ \%}$, which corresponds to an absolute uncertainty of about ± 0.018 for a *COF* of 0.06. The main contribution came from the uncertainty of the friction force ($\pm 28.8 \text{ \%}$). This was primarily caused by a high uncertainty in the inertial force $\Delta(m \cdot a)$ ($\pm 15 \text{ \%}$), and was followed by the uncertainties of F_{Gx} ($\pm 8.1 \text{ \%}$) and aerodynamic drag ($\pm 5.7 \text{ \%}$). $\Delta(m \cdot a)$ dominated up to velocities of about 18 m s^{-1} . At higher speeds, uncertainties of drag had the strongest contribution. COF-uncertainty introduced by the normal force was small ($\pm 1.4 \text{ \%}$), and was dominated by gravitational force uncertainty ($\pm 1.2 \text{ \%}$). Nevertheless, radial forces and their uncertainties would become more relevant in transitions, if the terrain is curved ($\Delta F_R = \pm 0.8 \text{ \%}$ with $r = 16 \text{ m}$).

With regard to the multivariate COF-models, total uncertainties of the snow-dependent COF-models were 0.013, for both ski and snowboard. The contribution of the snow measurements' uncertainties were 0.005 and 0.004 for ski and snowboard, respectively. The uncertainties of the snow measurements were on average $\pm 0.8 \text{ \%}$ for *LWC*, $\pm 0.3 \text{ }^{\circ}\text{C}$ for T_{ss} , $\pm 6.6 \text{ mm}^{-1}$ for *SSA*, $\pm 21.1 \text{ N}$ for *PR* and $\pm 31.3 \text{ kg m}^{-3}$ for the snow density.

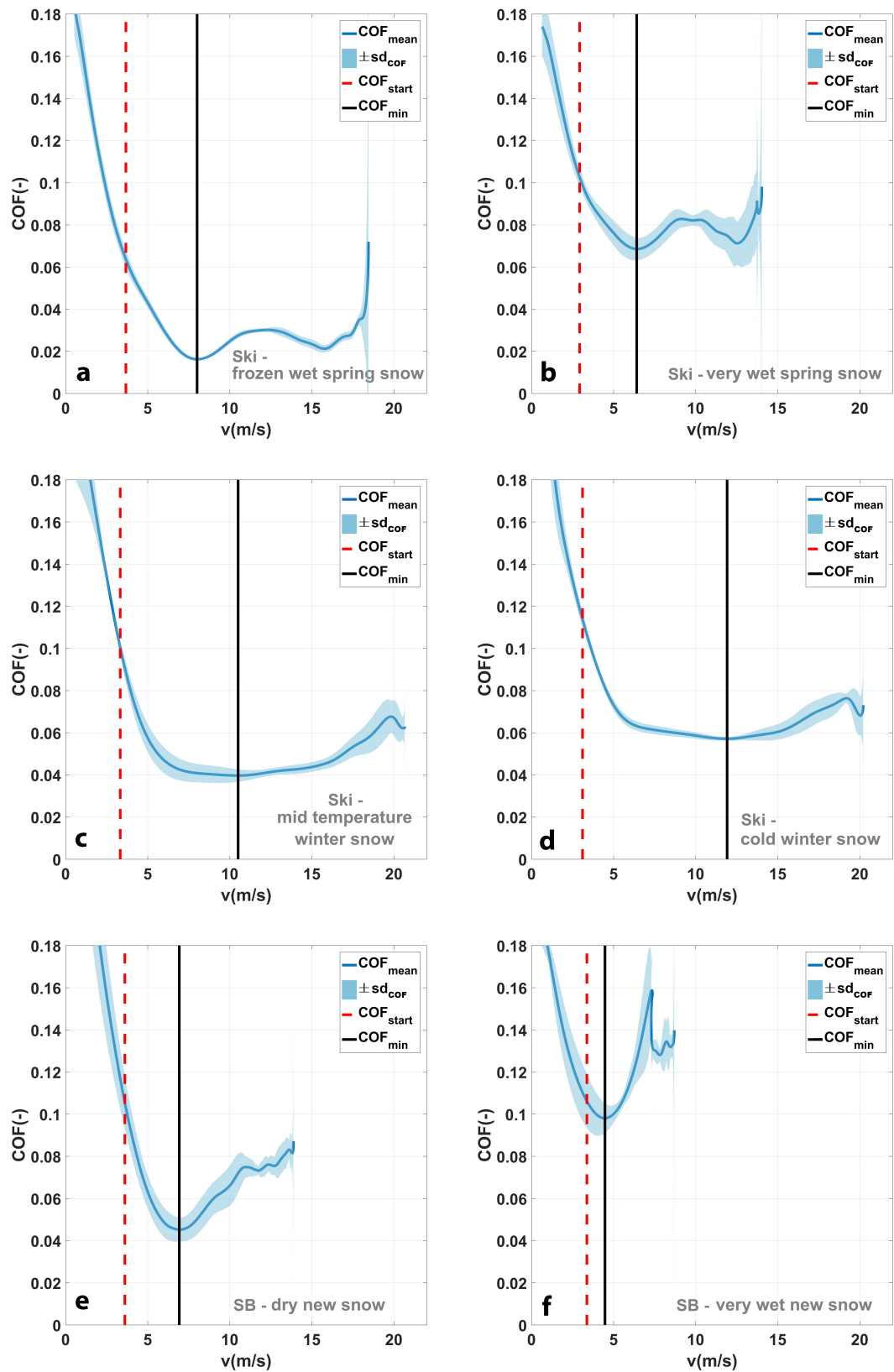


Figure 3.5: Mean COF-speed curves with error bands ($\pm sd$) and vertical lines to mark COF_{start} and COF_{min} for six snow categories: a) Skis on frozen spring snow ($n = 4$). b) Skis on very wet spring snow ($n = 4$). c) Skis on winter snow ($n = 3$). d) Skis on cold winter snow ($n = 5$). e) Snowboard on dry new snow ($n = 5$). f) Snowboard on very wet new snow ($n = 2$).

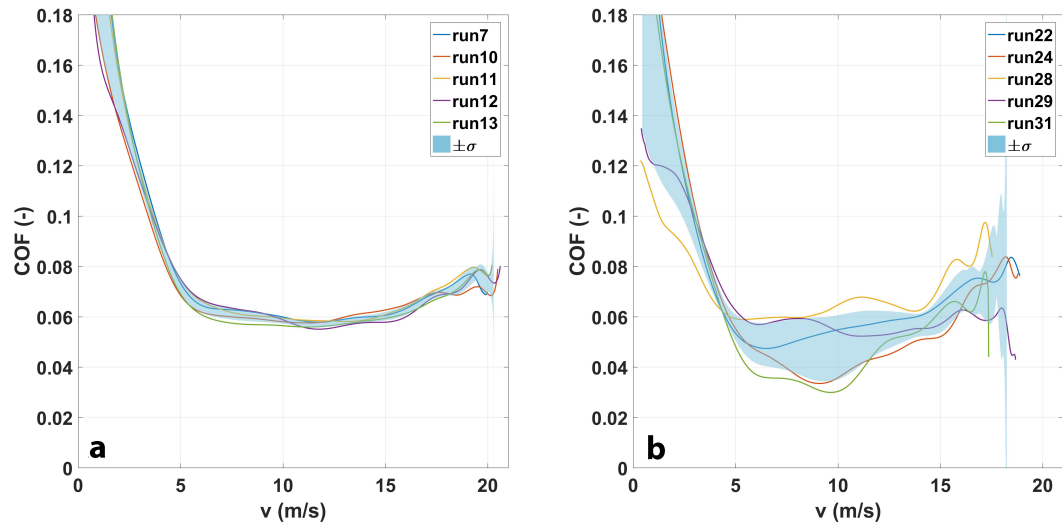


Figure 3.6: a) Five consecutive runs of skier S1 on cold winter snow (18-02-13) with calm air ($v_{wind} = 0.1 \pm 0.7 \text{ m s}^{-1}$, $COF = 0.059 \pm 0.001$). b) Five consecutive runs of skier S4 on warm winter snow (18-03-04) with a light breeze ($v_{wind} = 2.2 \pm 1.1 \text{ m s}^{-1}$, $COF = 0.054 \pm 0.006$).

3.2 Slider-snow friction laboratory experiments

3.2.1 Snow preparation

Snow samples were prepared over a wide range of *SSA* (5.2 to 37 mm^{-1}) and density (146 to 559 kg m^{-3}) (Fig. 3.7, Table 3.2), providing realistic and relevant testing conditions to investigate the ski-snow friction in the laboratory. However, reproducible compression and friction tests were only possible for snow samples with densities above about 350 kg m^{-3} in combination with sintering times between 12 to 20 hours. By that, the samples became sufficiently strong to not entirely collapse when loaded. Therefore, after performing preliminary tests, the final experiments were performed only on the three snow types (Fig. 3.8 to 3.10), fine-grained (FG2mm), mid-grained (MG2mm) and coarse-grained (CG1mm), which were prepared from ice powder of different grain sizes and compression distances of 1 to 2 mm, resulting in sample heights of 18.4 to 19.3 mm.

In total, 121 snow samples were prepared of which 71 were finally used for valid experiments. The mean density of the three different snow types ranged from 363 kg m^{-3} , over 507 kg m^{-3} to 522 kg m^{-3} . The mean *SSA* ranged from 5.6 mm^{-1} , over 8.4 mm^{-1} to about 20.5 mm^{-1} , respectively (Table 3.2). The *SSA*-values revealed from the InfraSnow were slightly elevated compared to those found by the micro-CT. Such smaller deviations can be explained with ongoing sublimation of smallest ice particles during the time between IS and CT measurement

(up to 48 hours) or differences in the compared measurement volumes. The snow samples could be well reproduced (Fig. 3.7). The volume-weight measurements revealed density variations of the samples ranging from 2.3 % (MG2mm, $n = 28$), over 3.4 % (CG1mm; $n = 27$) to 5.3 % (FG2mm; $n = 40$). The *SSA* (InfraSnow method) varied by 5.3 % ($n = 9$) on average for all snow types.

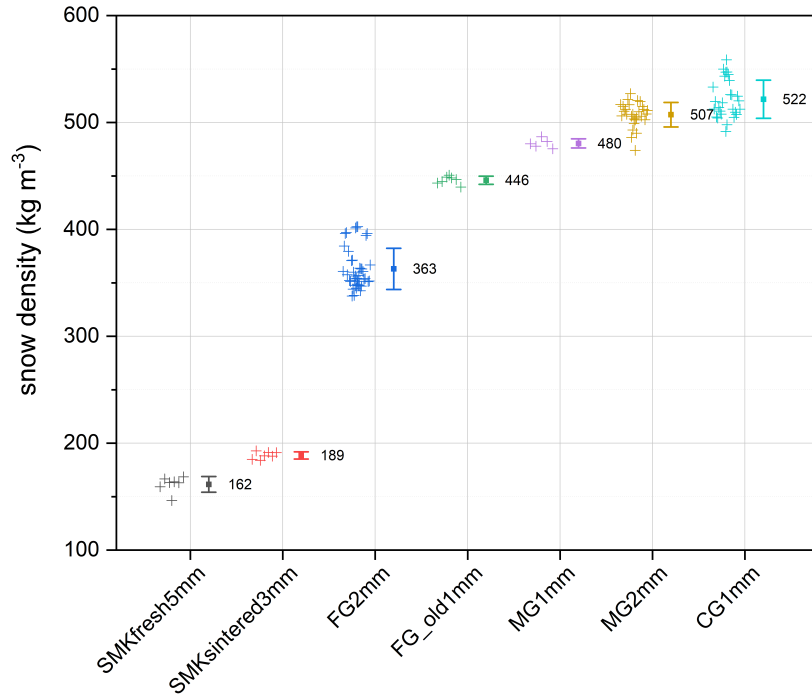


Figure 3.7: The different groups of snow samples and the reproducibility of sample preparation showed by the averages and variation of their density (mean \pm *sd*).

Table 3.2: Density and *SSA* of the prepared samples measured with different methods.

	volume weighted density (kg m ⁻³)	InfraSnow		micro-CT			
		mean	sd	mean	sd	density (kg m ⁻³)	SSA (mm ⁻¹)
SMKsintered3mm	189	\pm	3	35.4	\pm	—	—
SMKfresh5mm	162	\pm	7	37.0	\pm	—	—
FG2mm	363	\pm	19	20.5	\pm	1.1	375
MG2mm	507	\pm	11	8.4	\pm	0.4	514
CG1mm	522	\pm	18	5.6	\pm	0.4	18.4
							7.8

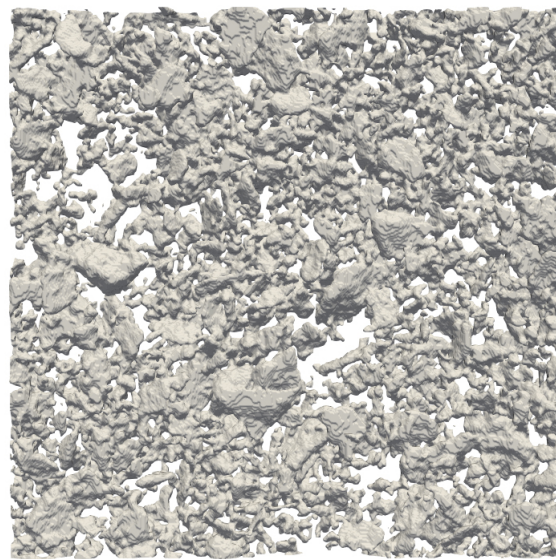


Figure 3.8: 9 by 9 mm crop of the top 0.9 mm of a fine-grained snow sample (FG2mm) in dry state.

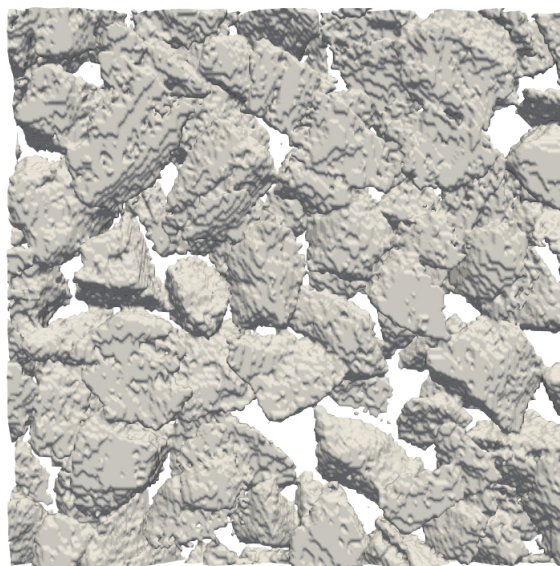


Figure 3.9: 9 by 9 mm crop of the top 0.9 mm of a mid-grained snow sample (MG1mm) in dry state.

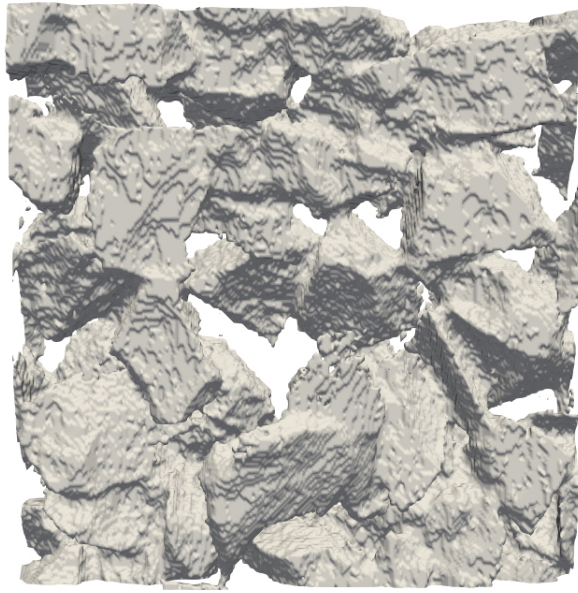


Figure 3.10: 9 by 9 mm crop of the top 2.7 mm of a coarse-grained snow sample (CG1mm) refrozen after having a *LWC* of 5.9 %.

3.2.2 Snow tribometry

The laboratory friction experiments revealed COF_{kin} ranging from 0.06, on dry coarse-grained snow, to about 0.1 on wet fine-grained snow (Fig. 3.11). Differences in friction between the three snow types were found largest for the dry snow state with distinctively lower COF-values of coarse-grained snow type. On fine and mid-grained snow, COF_{kin} were higher and more constant over the tested LWC-values, ranging only from 0.08 to 0.1. For a *LWC* above 10 %, the COF_{kin} were about similar for all snow types.

For all tested types of snow, the data showed a clear increase of the COF_{kin} from dry to wet snow, followed by a COF-decrease which, for the mid and coarse-grained snow types, transitioned into a constant COF-curve for higher *LWC*. This course of the COF-curves had general similarities but was pronounced differently for the different snow types as shown in Figure 3.11. Concerning all snow types, the decrease in friction after reaching a certain content of liquid water was surprising and gave reason to further investigate the water accumulation at the slider-snow interface as well the snow sample deformation as described below.

The measured COF in the laboratory laid within a smaller range as revealed from the on-field measurements (0.02 to 0.14). Although there was a general accordance showing increasing COF from coarse to fine-grained snow and from dry to wet snow. However, when comparing the data in detail, discrepancies existed between the snow friction found on the field and

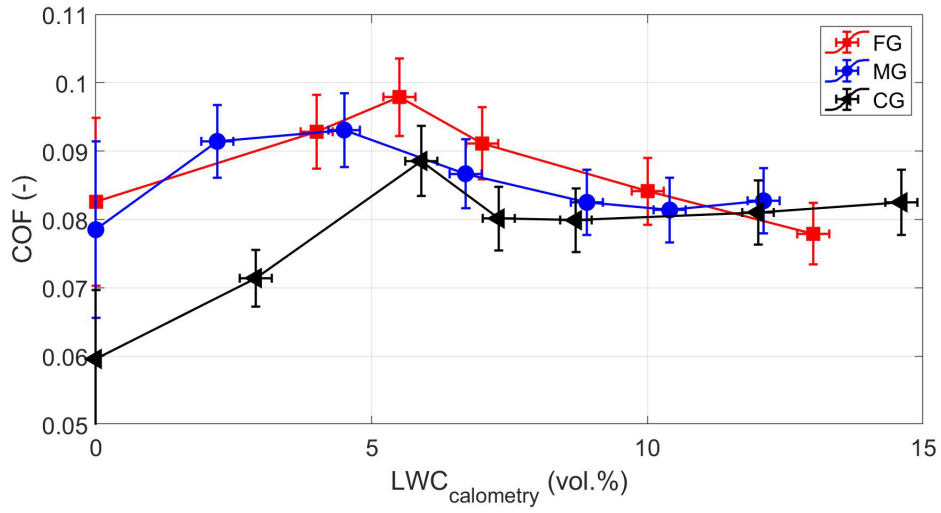


Figure 3.11: Kinetic friction coefficients (COF_{kin}) of a UHMWPE slider on fine, mid and coarse-grained snow in dry and various wet states with liquid water contents from about 2 % to 15 %.

in the laboratory. Most of all, the COF-maximum at mid-level LWC was contrasting the on-field results, where highest COF occurred at maximal LWC . Moreover, the interaction of high LWC and SSA leading to highest COF was not found in the laboratory. Possible reasons for the found differences are discussed in chapter 4.

3.2.3 Snow macro-mechanical characterization under compression

Snow as compressed during the ski-snow contact was shown to be dominated by irreversible brittle and possibly plastic deformations ranging from 0.17 to 3 mm. The corresponding work due to irreversible snow deformation ranged from 5 to 20 mJ for snow in dry state to about 60 to 89 mJ for the wettest snow samples (Fig. 3.12). Elastic (0.01 to 0.08 mm) and viscoelastic deformations (0.01 to 0.18 mm) were distinctively smaller. The different extend of total deformation strongly depended on type and state of the snow. The occurred total strains of the snow samples ranged from 0.014 to 0.106 for mid-grained snow (dry to max. *LWC*), over 0.024 to 0.166 for fine-grained snow, up to 0.038 to 0.141 for coarse-grained snow.

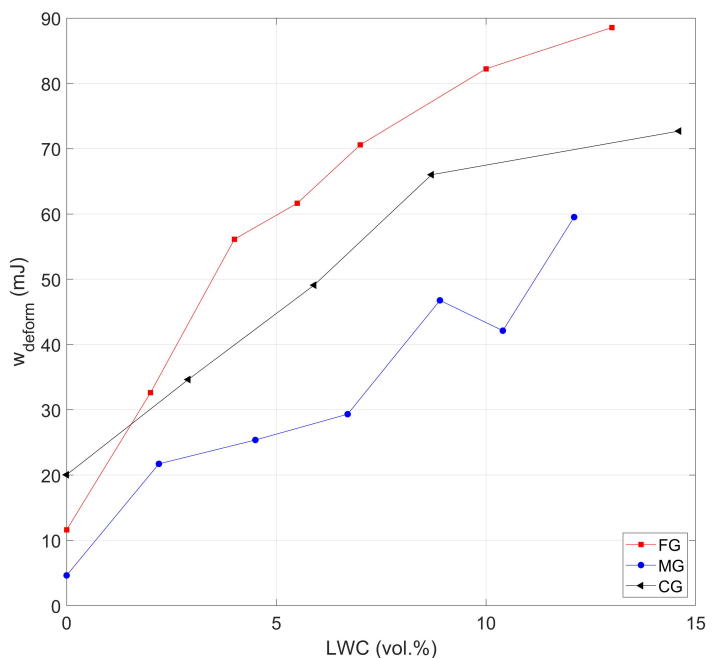


Figure 3.12: Deformation work of fine, mid, and coarse-grained snow in dry and various wet states with liquid water contents from about 2 to 15 %.

The fraction of permanent brittle and plastic deformation was higher than 90 % of the total deformation for 16 out of 19 snow sample configurations (Fig. 3.13, left). In general, those deformation fractions increased with increasing *LWC*, while the fraction of elastic deformation strongly dropped to low values below 4 % as soon liquid water was present (Fig. 3.13, middle). For dry snow, the fraction of elastic deformation ranged from about 5 % for coarse-grained, to about 29 % for mid-grained snow. In contrast to the elastic and plastic fractions, the viscoelastic fraction showed a distinct peak for all snow types at *LWC*-values

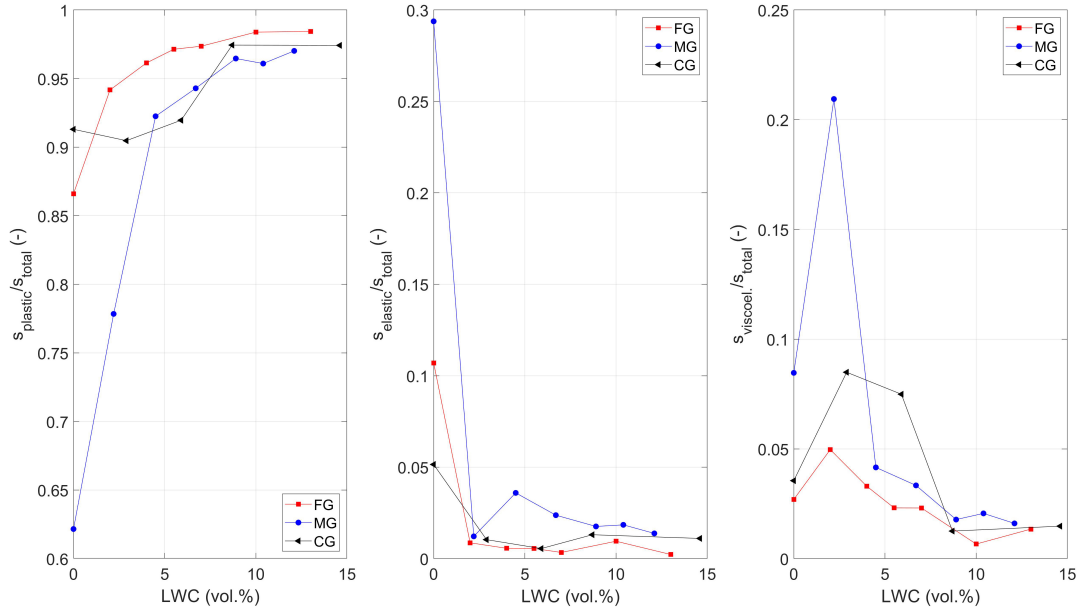


Figure 3.13: Permanent brittle and plastic (left), elastic (middle), and viscoelastic deformation fractions of fine, mid and coarse-grained snow in dry and various wet states with liquid water contents from about 2 to 15 %.

between 2 to 3 vol.%. Those peaks reached 5 % for fine-grained snow, 8 % for coarse-grained, and 21 % for mid-grained snow (Fig. 3.13, right). From the observed deformation modes, MG snow stood out with its relatively low plastic, but high elastic and viscoelastic deformation fractions for zero and low LWC . With higher LWC this characteristic changed, aligning the MG snow type more with the other types. The higher viscoelasticity of MG snow might be caused by an optimal distribution of the normal force over the contact points, so that stresses at the grain bonds were high enough to cause grain bond gliding, and therefore viscoelastic snow deformation (Theile et al., 2009), but low enough to prevent brittle failure.

The major permanent deformation occurred during the loading section 2, where the force rose linearly with deformation. The measured compression moduli of the different snow samples revealed the MG and FG snow type very similar at the dry state with values of about 2.9 N mm^{-2} , but differently in the moist and wet snow state with about 2 to 3 times higher values of the MG snow (Fig. 3.14). Both, MG and FG snow compression moduli distinctively dropped as soon liquid water was existent. For CG snow K_p in dry state was much lower (1.4 N mm^{-2}), staying constant for low LWC , and followed by a continuous decrease down to 0.7 N mm^{-1} with increasing LWC , showing similar values than the FG snow. Comparing the three snow types with each other, MG snow again showed a versatile character. In the dry state, it was comparable to FG snow, whereas in the moist state, it was akin to the CG snow type. As expected, the compressibility of the snow decreased for all snow configurations with increasing snow wetness (Fig. 3.14). However, the dynamic of how the material behavior changed and

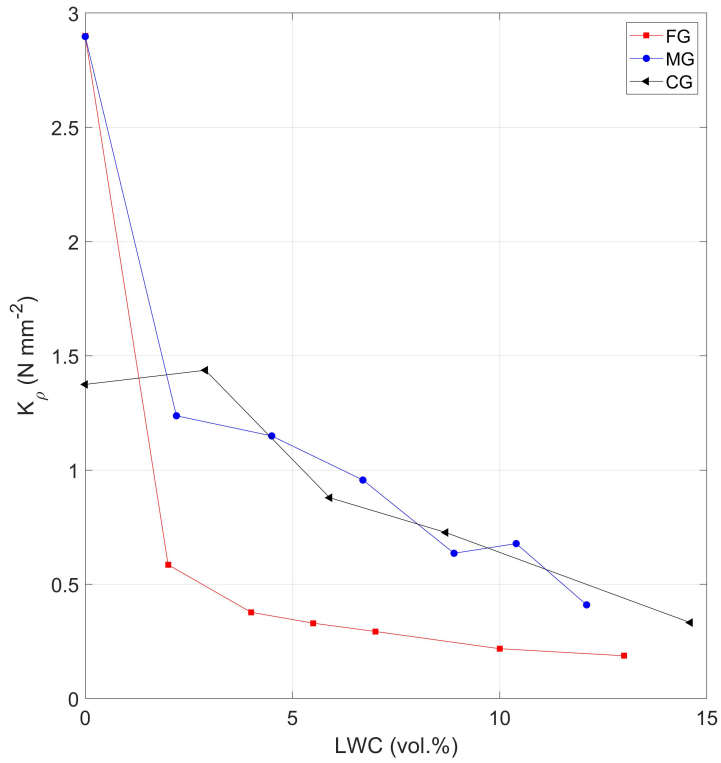


Figure 3.14: Compression module of fine, mid, and coarse-grained snow in dry and various wet states with liquid water contents from about 2 to 15 %.

the differences among the tested snow types, were surprisingly large. For fine-grained snow K_ρ dropped by a factor of about 10 when LWC increased from 0 to 5 %. And, at LWC of 5 % K_ρ differed by a factor up to 3 between FG snow and MG or CG snow. For higher water contents, K_ρ of the three snow types converged again.

The low K_ρ value of dry CG snow might be caused by its large grains, which were loaded rather singly, leading to failure, whereas for smaller grains the number of loaded grains was assumably large enough to distribute the incoming forces more evenly, preventing grains and their bonds from overload and failure. The distinct softening of fine-grained snow was probably a consequence of its low density (363 kg m^{-3}). Due to that, more pore space was compressed as soon as grain bonds got sufficiently weakened by melting and failure. This was different for the other snow types with higher densities (515 kg m^{-3}), which are close to a random close packing density of about 600 kg m^{-3} (Anderson and Benson, 1963), which limits their compressibility even in a granular state after breaking most of the grain bonds.

After building up the force, which was dominated by deformations due to brittle failure and

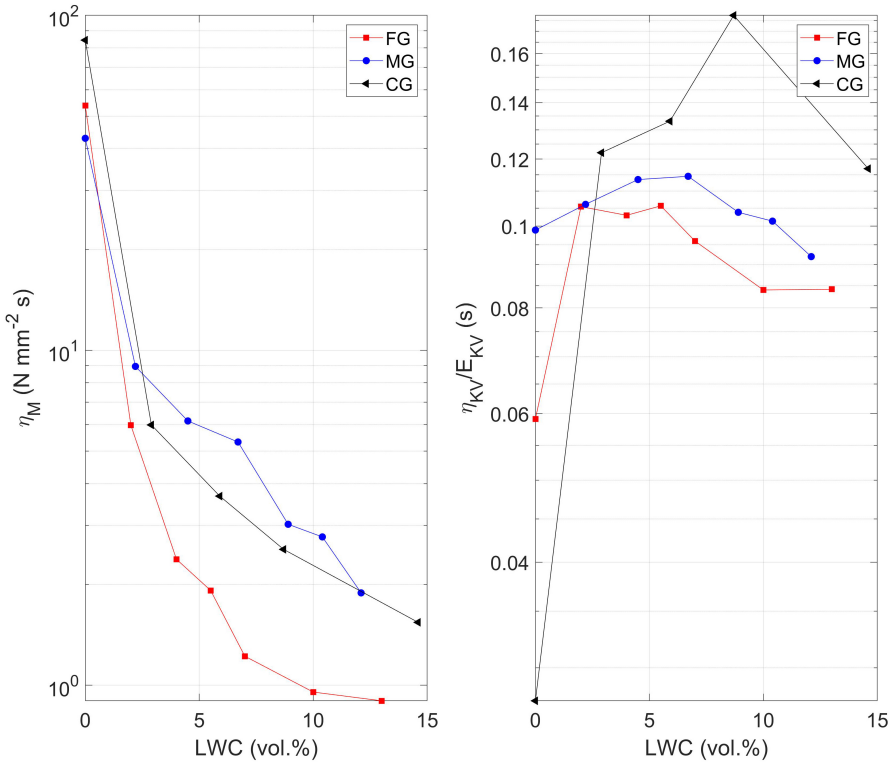


Figure 3.15: Parameter of the burger model fitted to the strains under constant stress loading of fine, mid, and coarse-grained snow in dry and various wet states with liquid water contents from about 2 to 15 %. Left) Dashpot constant representing viscoplastic deformations. Right) Relaxation time (η_{KV}/E_{KV}) representing the viscoelastic deformations.

(instantaneous) plastic deformations, the third loading phase under constant stress followed (Fig. 2.14, chapter 2.3.4), dominated by viscoplastic and viscoelastic deformations. The burger model approximated well the measured viscoplastic and viscoelastic deformations for the different snow configurations ($R^2 > 0.97$; Fig. 2.14, chapter 2.3.4). A strong decrease of viscosity η_M with increasing LWC was found for all snow types. This was most pronounced for FG snow where η_M dropped by a factor of 15 from the dry state to maximal LWC (Fig. 3.15 left). Related to the experiments, this meant that viscoplastic deformation were neglectable for dry snow and grew with increasing LWC up to about 0.1 mm. In contrast, the viscoelastic deformations, expressed by the relaxation time η_{KV}/E_{KV} , increased only until low to mid water contents, followed by a decrease for higher LWC -values (Fig. 3.15 right).

The revealed model allowed to parametrize snow deformations by type and state of the snow, and, beyond that, depending on the duration and extend of loading. For similar conditions as for the measurements ($t_{load} = 0.3$ s corresponds to a skiing speed of 5 m s⁻¹ with a ski length

of 1.5 m; $p = 20$ kPa), the model revealed viscoplastic and viscoelastic strains up to about 0.01, and up to about 0.02, respectively. The latter matched not perfectly with the measured magnitudes of viscoelastic strains (up to 0.01). However, the found rheological description of various types and states of snow, provided a basis to include viscous deformation modes when describing the ski-snow frictional contact. On the one hand, this appeared important on the microscopic scale of contact formation, expecting an increased RCA compared to elastic Hertzian contacts. On the other hand, viscoplastic and viscoelastic deformations appeared relevant regarding the macroscopic snow deformation, and its effects on the liquid water distribution at the ski- snow interface and in its close proximity.

3.2.4 Snow liquid water redistribution under compression

The relative permittivity at the initial sensor-snow contact ε_{cntc} clearly indicated that for FG snow more water was contained closely to the interface than for the other snow types (Fig. 3.16). This can be explained by higher capillary forces due to the snow's higher SSA (finer microstructure), leading to a higher liquid water holding capacity. The higher ε_{cntc} was pronounced for snow with a high overall LWC (as revealed from calorimetry of the whole sample). Whereas for lower overall LWC , ε_{cntc} was only slightly elevated compared to MG and CG snow. For MG and CG snow, ε_{cntc} stagnated for overall LWC above about 9 %. For FG snow this stagnation was not able to be observed, as no samples with overall LWC above 9 % were tested. The found stagnation of ε_{cntc} was explained by the transition from the pendular to the funicular regime, where water percolates from the top of the snow sample down to larger depths (Fierz et al., 2009), and therefore contributed less to the permittivity signal. The found conditions of the initial contact became even more pronounced at full load, showing ε_{cmp} values for FG snow, which strongly exceeded those for MG and CG snow (Fig. 3.17). Consequently, the permittivity increase ($\Delta\varepsilon = \varepsilon_{cmp} - \varepsilon_{cntc}$) from initial to full load was strongest for FG snow, followed by MG snow, and was weakest for CG snow (Fig. 3.17 left). In first summary, the data indicated that during the ski-snow contact, water within the snow accumulated towards the interface in different degree, depending on the snow type.

Taking a deeper look into the processes during the contact, it was revealed that $\Delta\varepsilon$ was not only influenced by the prevailing water and by how well it was hold or drained deeper into the snow sample. The extent and the local distribution of deformation interacted with the containing water. On one side, the amount of prevailing water increased the snow's compressibility due to ongoing melting of grain bonds (Fig. 3.14). On the other side, compressing the snow increased the water (and ice) volume fraction. In consequence, large local deformations occurred at regions of large water content starting at the top of the sample. This interaction of water and deformations was able to amplify the effect of water occurrence near the snow-sensor interface depending on the snow type. To a certain extent, this explained the increasing $\Delta\varepsilon$ from CG to FG snow (Fig. 3.17 right & left): FG snow contained the most water over the smallest height, while experienced the largest total deformation, and the largest local deformations at the narrow, wet and weakened top layer (Fig. 3.18), where

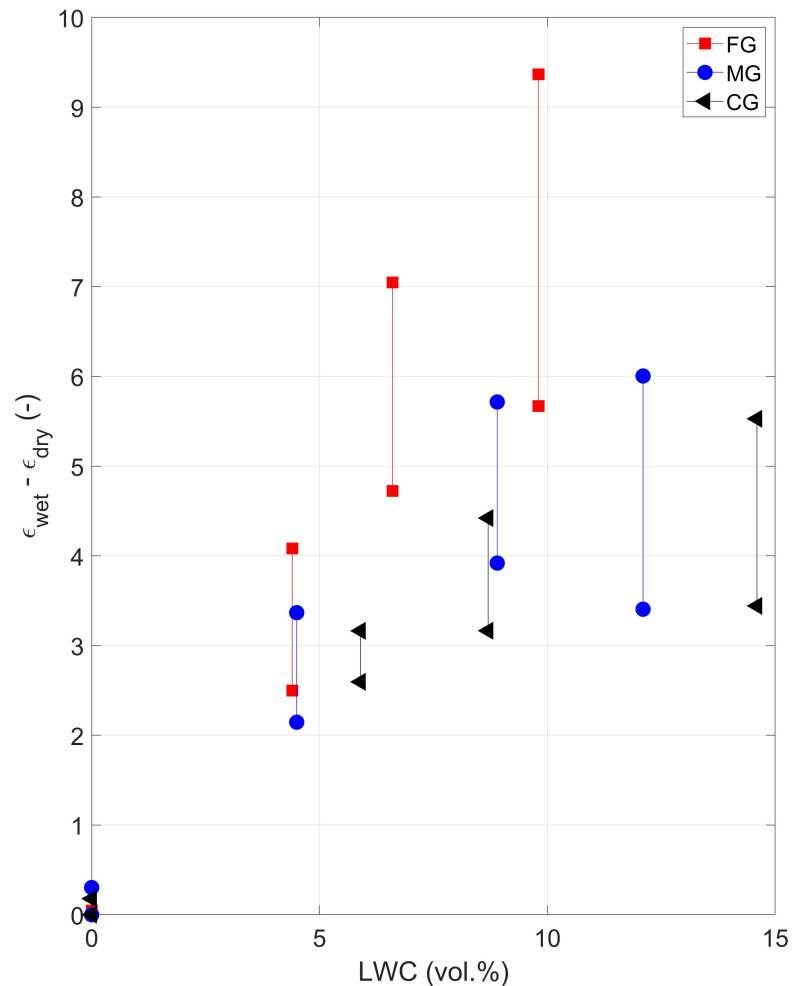


Figure 3.16: Increase of relative permittivity of snow from dry to wet state vs. overall *LWC* at the initial contact of sensor and snow (lower values), and at full load (connected higher values). The overall *LWC* were revealed from calorimetry measurements of the complete snow samples.

the pore space collapsed during loading until reaching full water saturation. This assumably caused an abrupt hydrostatic pressure increase, as well as water moving towards the sensor (Fig. 3.18 right). In contrast, for CG snow, local water concentration and deformations were not high enough to fully saturate the pores with water, preventing the same massive increase of ϵ as for FG snow, although the total deformations were as high as for FG snow (Fig. 3.17 right). Interestingly, for all snow types the total deformation stagnated beyond a certain *LWC* limit, whereas $\Delta\epsilon$ further increased with growing *LWC* (Fig. 3.17 right). Different reason appeared plausible, depending on the snow type. For FG snow, the drop of compressibility of the saturated top layer was somewhat limited by the hydraulic resistance against water, floating into pore spaces of lower, so far dry snow volumes. Whereas for very wet CG snow, which was soaked and weakened throughout its full height, in the case of an entire collapse of the sample, the walls of the sample holder would provide a constant strength to the unbonded ice grains. Together with the supporting sample holder, the maximal packing density of the snow grains determined the observed deformation limits. In that situation, the sinter-material characteristics of snow changed over to a granular like behavior.

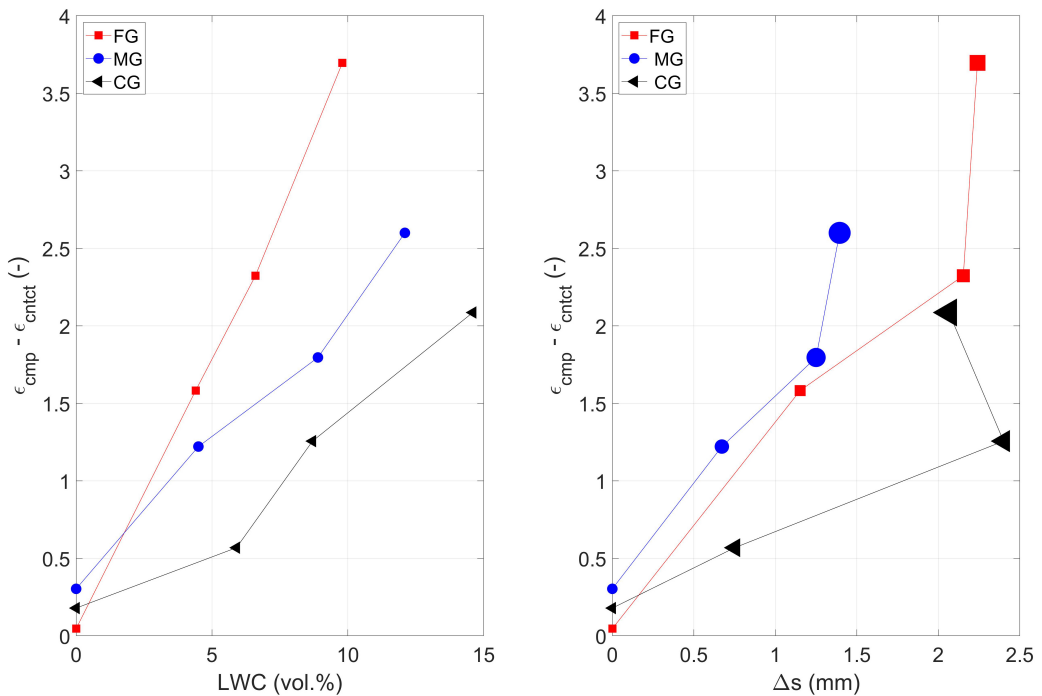


Figure 3.17: Left) Increase of the relative permittivity of snow from the initial snow-sensor contact until full load was reached vs. the overall *LWC*. Right) Increase of the relative permittivity of snow from the initial snow-sensor contact until full load was reached vs. the corresponding snow deformation. The marker size corresponds to the overall *LWC*, which were revealed from calorimetry measurements of the complete snow samples.

In summary, the measurements of the snow's relative permittivity during compression showed that enhanced water accumulations near the ski-snow interface occur in wet snow with high *SSA* and low density. Besides the water-holding capacity, which caused the increased surface-near water content at the initial contact, the high compressibility of wet FG snow was identified as a key property, causing highest surface-near water accumulations at fully the loaded ski-snow contact. Concerning the ski-snow friction, it is important to understand the occurring water at the interface, which originates from the snow itself (beside that from frictional heating) as a process variable which strongly depends on the snow mechanics. Besides the given snow mechanical properties, in the real ski situation the dynamic of snow deformation also depends on the speed of a skier.

In combination with interfacial water, the topography of the snow surface (and the ski) builds the major constrains for the frictional regime of a ski gliding on the snow. Like interfacial water, the snow surface micro-topography cannot be considered as a stationary boundary condition. Instead, it is assumed to be different depending on the snow physical properties, and to change considerably due to the ski-snow contact. Therefore, the following, last section of this study, addressed morphological changes of the entire snow sample during the contact, with a specific focus on the snow surface topography on the microscale.

3.2.5 RCA estimation and snow morphological changes

μ CT-scans of the snow sample before (pre) and after (post) the contact showed a distinct densification of the upper parts of the snow samples due to the irreversible deformation of the ice matrix during compression as well as because of liquid water concentration (Fig. 3.18). The wet snow samples got densified already before the contact, as liquid water from melted snow grains in the very top of the sample were retained in the pore space (Fig. 3.18 middle, yellow). Depending on the *LWC* and the grain size, the distribution of liquid water within the snow sample differed, and so the increase in snow density did. For CG snow only a slight increase of density in the top section of the sample was found (Fig. 3.18 left), as most of the liquid water percolated. Instead for the MG, and especially for FG snow, most of the melted ice was retained at the top of the snow sample due to higher capillary forces (Fig. 3.18 middle, right). At very high *LWC* of the CG snow sample, it was shown that most of the water moved to the bottom where the snow sample was fully saturated revealing a density close to 900 kg m^{-3} (Fig. 3.18 left, red). Although for FG snow, samples with highest *LWC* were not scanned, the density profiles indicated a concentration of liquid water at the very top, contrary to what was shown for CG snow (Fig. 3.18 right, red). Beside the distribution of the liquid water within the samples, the CT-scan revealed density inhomogeneities throughout the FG snow samples, already in the dry state (Fig. 3.18 right, yellow).

After being in contact with the slider, the snow samples' surface topographies indicated RCA_{rel} ranging from about 2.3 % for wet CG snow to about 6 % for wet FG snow (Fig. 3.19). Finding the lowest *RCA* estimates for CG snow was not surprising due to its low number of grains per volume, the strong percolation of water away from the surface, allowing

almost no contact area contribution by (refrozen) water, and its low compressibility in the wet state (Fig. 3.19), which affects both, less horizontal alignment of surface grains and less water concentration by pore compression at interface proximity. The found increase of *RCA* for MG and FG snow generally agreed with this line of reasoning. However, the influence of the liquid water on the *RCA* including the related change of mechanical parameters (e.g. increasing compressibility), was found rather weak when comparing the *RCA* of MG or CG snow with increasing *LWC*. Nevertheless, a tendency to elevated *RCA* with growing *LWC* was supported by the data: *RCA*-means for CG slightly increased from 2.7 to 3.2 %, and for MG from 3.5 to 3.8 %. Beyond that, methodological limitation might have played a role (see chapter 4.2).

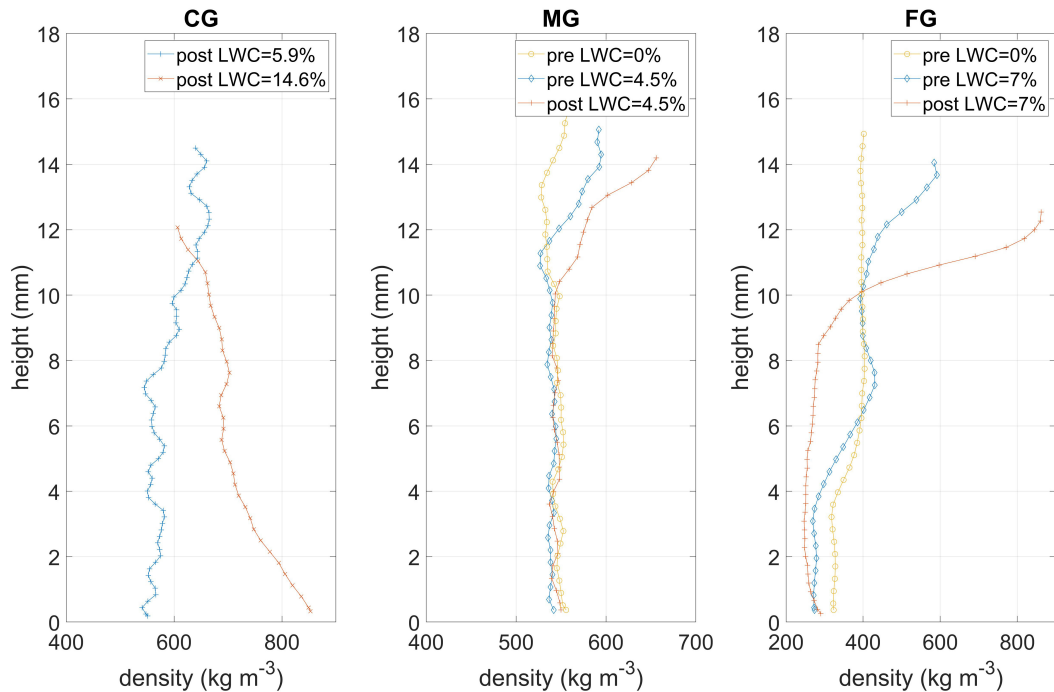


Figure 3.18: Density profiles of the snow samples before (pre) and after (post) the compression experiments.

The topographic analyzes of the snow surfaces indicated for all snow types, that most of the grains at the surface were in contact with the slider (Fig. 3.20 to 3.22), except for one FG snow sample where a systematic decrease of contacts to the left side of the sub-volume was visible (Fig. 3.22 right). Assumably this might have been related to methodological limitations (see chapter 2.3.6). The surface topographies showed the different sized snow pores, which made clear why liquid water within CG snow was hold much worse at the snow's top surface close to the interface. As mentioned above, the *RCA* was only slightly affected by changes of *LWC* and the related mechanical parameter. However, the topography did change from the dry to the wet state as shown in Fig. 3.21: The surface of MG snow

recognizable changed showing increased connections of the grains as well as compaction of the grains within this thin surface volume which corresponds to the measured densification (Fig. 3.18 middle). Whereas the dry to wet transition was clearly visible, different degrees of snow wetness revealed no drastic changes in topography. For CG snow the surface grains appeared just slightly more rounded comparing a *LWC* of 5.9 % with 14.6 %.

The number of contact grains increased from CG ($n_g \approx 25$), over MG ($n_g \approx 52$), to FG snow ($n_g \approx 130$). In consequence, the average load per single grain was assumed clearly higher for CG (2.2 N) snow than for MG (1.1 N) and FG (0.4 N) snow. The averaged contact stresses as deduced from the found range of RCA_{rel} ranged from 865 kPa to 332 kPa. The average size of a contact deduced from the RCA was about 0.04 mm^2 for FG snow and about 0.09 mm^2 CG snow. As shown in Fig. 3.20 to 3.22 sizes of contact spots vary from a few pixels (0.01 mm^2) to about the size of a snow grain (ca. 1 mm^2). The average stresses at the slider-snow contacts, corresponding to the found RCA , were about a factor of ten smaller than the compressive strength of ice at $0 \text{ }^\circ\text{C}$, but in the order of magnitude of the compressive strength of the snow (see chapter 1.1.1).

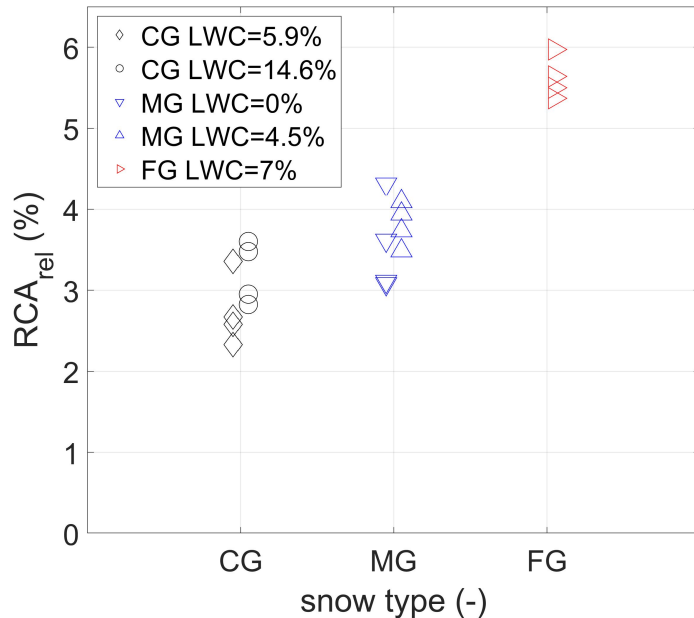


Figure 3.19: Estimated RCA_{rel} of five snow samples after compressive contact with a slider deduced from the samples' flat surface features as revealed from μCT -scans. From each snow sample four equally sized sub-volumes were used to deduce the RCA -values.

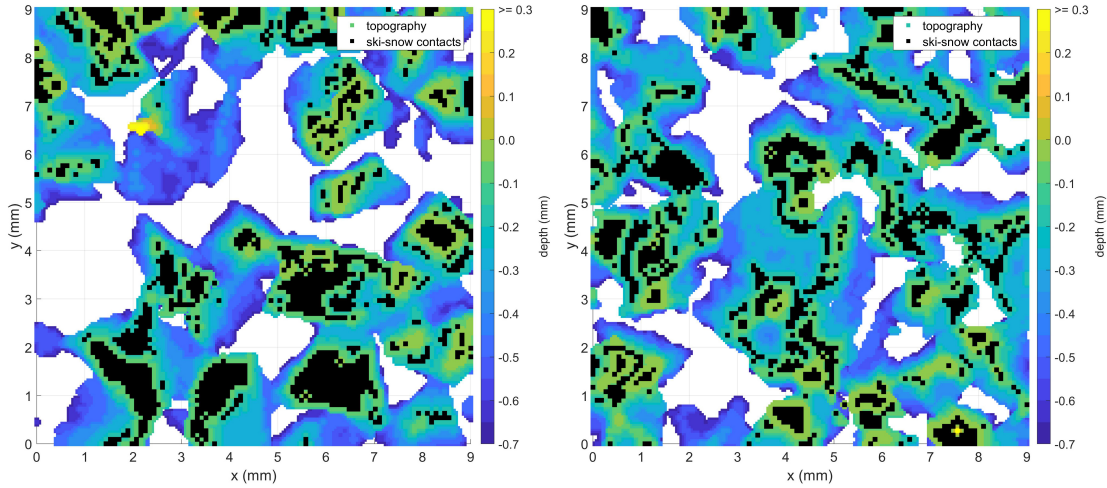


Figure 3.20: Surface topography and contact spots (black) of a coarse-grained snow sample after compressive contact. Left) Snow with a LWC of 5.9 % and a deduced RCA_{rel} of 3.4 %. Right) Snow with a LWC of 14.6 % and a RCA_{rel} of 3.5 %.

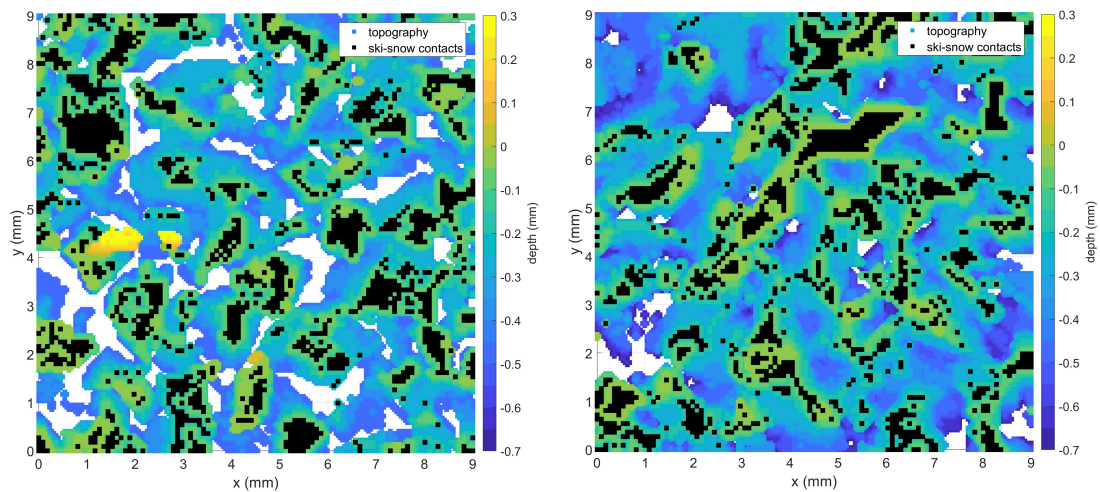


Figure 3.21: Surface topography and contact spots (black) of a mid-grained snow sample after compressive contact. Left) Snow in dry state with a deduced RCA_{rel} of 3.6 %. Right) Snow with a LWC of 4.5 % and an RCA_{rel} of 3.7 %.

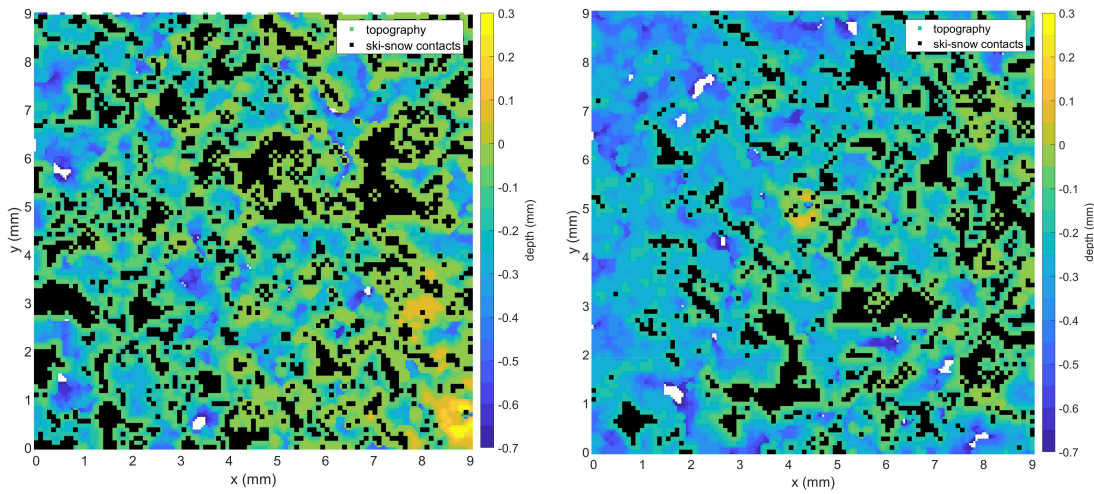


Figure 3.22: Surface topography and contact spots (black) of two fine-grained snow samples after compressive contact. The snow samples had overall LWC of about 7 % and RCA_{rel} of 6 % (left), and 4.6 % (right).

4 Discussion

*The following two paragraphs are part of the publication: Wolfsperger, F., Meyer, F., Gilgien, M., 2021. The snow-friction of freestyle skis and snowboards predicted from snow physical quantities. *Frontiers in Mechanical Engineering*, 7, 728722.*

The presented data quantified how strongly snow properties influence the friction of skis and snowboards and gave new insights on the interaction of snow properties, interfacial water accumulations, the *RCA*, and their role for involved frictional processes.

Snow friction was measured on the real scale over a wide range of snow conditions in a consistent and comparable manner, using the same method and equipment with the same athletes over two winter seasons. For the first time, the effects of changing snow conditions on friction could be related to a set of measurable physical properties of snow and their interactions. In addition, this study showed how speed influences snow friction of real skis depending on the prevailing snow conditions.

Experiments of the slider-snow interaction were performed in the laboratory to investigate the processes behind the dependencies of the ski-snow friction as found on the field. A focus was set on the wet snow friction processes, which revealed the interaction of the snow's interstitial water with its compressibility and microstructure. Beyond that, the formed *RCA* during the slider-snow contact was quantified and compared for different snow conditions.

Within this study measurement methods were developed, adapted, and elaborated, which enabled to quantify mostly inaccessible parameters of the ski-snow tribological system. GNSS-based ski-snow friction measurements, including wind and aerodynamic measurements, were shown to be sufficiently precise to differentiate the *COF* of various snow conditions over a large measurement area. By that, also the influence of speed on the ski-snow friction was measured for the first time under realistic skiing conditions. Precondition for that were adaptations of existing methods towards reliable field-ready snow measurement instruments, e.g. the InfraSnow. Besides a rich set of available experimental and snow analysis methods in the SLF cold laboratory, sensors and analysis methods were further developed (e.g. high temporal resolution *LWC* measurements)

4.1 Ski/Snowboard-snow friction field measurements

4.1.1 Comparison of the results with the literature

The following subchapter is part of the publication: Wolfsperger, F., Meyer, F., Gilgien, M., 2021. The snow-friction of freestyle skis and snowboards predicted from snow physical quantities. Frontiers in Mechanical Engineering, 7, 728722.

The first friction experiments with real skis were conducted by Bowden and Hughes (1939) revealing *COF* from 0.04 to 0.08 by pulling loaded skis ($v = 0.1 \text{ m s}^{-1}$) over fine-grained snow, which was at 0 °C with some melting towards the end of the experiments. Decades later on-field measurements of the *COF* during real skiing revealed values between about 0.009 and 0.1 (Kaps et al., 1996; Habel, 1968; Kuroiwa, 1977; Leino & Spring, 1984) confirming the order of magnitude of the values found in this study. However, the minimal and maximal *COF* obtained in the current study were distinctly higher than those found in former studies. The fact that wind and skiers' drag areas were not measured in the cited studies, as well as the unknown reproducibility due to the low number of identical experiments, raises doubts about the use of those results as reference values. In general, comparisons between studies are difficult due to unknown differences in ski equipment, waxing and snow properties. A more recent study by Budde and Himes (2017) presented a large *COF* data set for CC-skis (at 5 m s^{-1}) with different grindings and wax configurations, using a test sled. *COF* ranged from 0.005 on spring snow ($T_{air} > 0 \text{ }^{\circ}\text{C}$) to 0.035 on new snow ($T_{air} = -25 \text{ }^{\circ}\text{C}$). Their results confirmed the findings of Kaps et al. (1996), with the lowest *COF* being less than 0.01, but did not show the upper boundary of possible *COF* on wet and very wet snow. The average *COF* of 0.013 for the fastest snow conditions (with factory-ground base) corresponded well to the instantaneous minimum of 0.016 found in the current study (Table 3.1), especially considering that CC-skis are assumed to have a slightly better gliding performance compared to freestyle skis. Regrettably, the snow characterization was limited to an oversimplified categorical classification of new, old, and transformed snow. The applied photogrammetry in the earlier studies as well as the use of more recently introduced ski sleds (Swaren et al., 2014) showed that immense effort is needed to conduct accurate on-field measurements revealing true absolute *COF*-values. In contrast, among ski racing teams it is common practice to quantify snow friction by conducting gliding tests with exact time measurements over defined sections. This rather simplistic approach is intended to find significant differences in gliding performance between different types of skis, if conditions are stable and testers have excellent ability to reproduce postures. However, in addition to other methodological concerns (Colbeck, 1994), a uniform quantification of snow friction using a friction coefficient is lacking with this approach.

To overcome those problems, Nachbauer et al. (2016) introduced a real-scale laboratory tribometer that is considered the state-of-the-art *COF*-measurement, providing high accuracy, adequate precision (Hasler et al., 2016), and high validity for a laboratory setup, as real skis or snowboards can be tested. *COF* ranging from about 0.025 to 0.075 have been reported

for alpine skis on machine-made snow (Schindelwig et al., 2014; Rohm et al., 2017). On cold snow (-11 °C) Nachbauer et al. (2016) reported a constant COF over speed (5 to 15 m s $^{-1}$) of 0.06, whereas on warm snow (-3 °C) a COF -increase from about 0.03 to 0.055 was found. In this study, on cold winter snow (-14 °C) a constant COF was found that was slightly lower (0.052, Table 3.1). On warm winter snow, COF also increased with speed up to 0.067 (15 m s $^{-1}$), but were higher at lower speeds (0.046 to 0.053). For boarder-cross snowboards, COF were reported from 0.035 to 0.045 at speeds from 5 to 8 m s $^{-1}$ ($T_{ss} = -6$ °C) (Hasler et al., 2014), which corresponded well with our observed instantaneous COF at 8 m s $^{-1}$ on warm winter snow (-4 to -6 °C) of about 0.045 for a freestyle snowboard (Table 3.1).

In summary, the presented COF correspond well with values from the literature. Comparability of the studies was mainly available for dry snow conditions with COF below about 0.06. This suggests high internal validity of the applied dGNSS-based method and supports there being sufficient external validity for the full range of COF from about 0.02 to 0.14. However, an intrinsic challenge of snow friction measurements, whether in the laboratory or in the field, is the fact that friction forces are small, while noise increases with higher speeds and due to the inherent fragility of snow.

4.1.2 Interpretation and limitations of the friction measured on the field

The following subchapter is part of the publication: Wolfsperger, F., Meyer, F., Gilgien, M., 2021. The snow-friction of freestyle skis and snowboards predicted from snow physical quantities. Frontiers in Mechanical Engineering, 7, 728722.

The introduced snow categories provide simple guidance to what COF -values can be expected, depending on prevailing snow conditions. It was found that the fastest gliding (low $COF < 0.03$) occurred on hard spring snow, followed by warm to mid-temperature winter snow. COF -values up to 0.06 occurred on cold winter snow, comparable with the COF on new snow (groomed) at warmer snow temperatures. On dry snow, the highest COF of up to 0.08 occurred during snowfalls. Higher COF only occurred when the snow became wet or very wet. For spring snow, COF -values up to 0.09 were found, while for groomed new snow values of up to 0.14 were reached. It can be assumed that these are upper boundary values, which are unlikely to be exceeded because much higher LWC-values do not occur at the snow surface due to percolation, and because the unfavorable microstructure of new snow for fast gliding transforms quickly when liquid water is present (Armstrong and Brun, 2008).

Lowest friction (> 0.026) was measured on dry, well sintered, and therefore hard spring snow at close to zero temperatures. The snow compressive strength was high, with small total and permanent deformation. The resulting real contact area was therefore assumed to be small. In addition, close to zero ice temperatures facilitated melt water lubrication, minimizing solid-to-solid contacts. In contrast, the increase of friction on dry winter snow (> 0.042) and new snow (> 0.060) was assumed to be connected to larger snow deformation forming a larger real contact area. Meltwater generation must be assumed as well, even for

the coldest snow temperatures down to -18°C , as a higher *COF* would be expected for solely dry friction (Colbeck, 1992). The large *COF*-differences measured on very wet spring and new snow (0.082 vs. 0.134) with similar *LWC*, support the finding from the laboratory that a key to explaining snow-dependent ski friction is understanding the interaction of snow microstructure, its deformation and resulting real contact area with lubrication and capillary effects due to melt water lubrication, and liquid water dynamics within the snow. However, to identify prevailing lubrication regimes and disentangle *COF*-contributions from real contact area, mixed or hydrodynamic friction, and capillary attraction would require instrumented skis to detect the water film thickness and real contact area during skiing. Moreover, on wet and very wet snow, doubts arose about the *COF*-decrease right after the start. According to the theory, friction should be low right from the start, as sufficient lubrication should occur due to the *LWC* of the snow. A possible explanation could be that at slower speeds, the snow was loaded for a longer period and at a lower strain rate, which may have increased snow deformation and adversely affected real contact area and water distribution at the interface. Beyond that, the analysis of snow friction at low speeds was limited as the slope of the terrain was calculated from the instantaneous velocity vector and not from separate terrain measurements, which had data gaps on several test days. Due to the static postures of the athletes, with very little vertical body movement, the slope calculation worked well as soon the athletes settled into their posture. Before that, during the first 4 meters of gliding at rather low speeds, the *COF*-curves were biased and made analysis difficult.

To find the full range of ski and snowboard friction, tests were conducted on various snow conditions. However, no tests were done on very cold snow between -20 and -30°C . Therefore, the known increase of snow friction on very cold snow was not well represented in the data, especially for snowboards, where the coldest snow was around -13°C (Fig. 3.3; Table 3.1). Moreover, no tests were done on machine-made snow due to numerous snowfalls during the winter of 2017/2018, but measurements were made on frequently groomed and well-sintered winter snow, which had comparable properties (Table 2.3). To overcome the need to measure snow friction in all possible snow conditions, the gaps between discrete snow categories were filled by interpolating snow friction over a continuous snow parameter space. This was achieved using the presented multivariate *COF*-parametrizations, based on a sufficient number of tests on contrasting snow conditions. The area of *COF* data interpolation in the *TLWC-SSA* plane is shown by the dotted black line in Figure 3.3. Outside from that area, and for very high and low *PR*, *COF*-values were extrapolated, which limited their validity. Limitations due to a narrow data set, meaning a small range of tested snow conditions, were also apparent for the single parameter *COF*-models for snowboards (Fig. 3.2).

The abrasion of wax during a test day was not quantified by additional contact angle measurements. Depending on the test track and number of runs, the total distance of skiing on a test day varied from about 13 to 27 km. According to Rohm et al. (2017) significant wax (paraffin) abrasion had to be assumed on cold snow leading to a reduction of the base's water contact angle. Whereas on warm snow, abrasion was reported to be much less keeping contact angles unaffected, at least over the first 9 km. Therefore, the wet snow tests at the test track at Bolgen (Fig. 2.1 a), which was in close proximity to the chairlift keeping the

skied distance small, are probably less affected by wax abrasion.

The uncertainty of the presented COF-values had an upper limit deduced from error propagation calculations of about ± 0.018 , and a lower limit of about ± 0.001 based on the measured variability of COF-averages of consecutive runs under optimal conditions. A limitation of the applied *COF* measurement method was the calculation of relatively small friction forces from accelerations with considerable uncertainties. The magnification of superimposed noise on kinematic data when determining accelerations from displacement data is a known problem in biomechanics (D'Amico and Ferrigno, 1992). The spline smoothing of the position data applied here is an approved method to minimize superimposed noise effects on the raw data Skaloud et al. (2003). Nevertheless, further smoothing of the speed and acceleration had to be conducted to eliminate artifacts in the COF-curves (Fig. A11 & A12). An exact determination of the uncertainty of accelerations used for the COF-calculations was difficult as uncertainty depends on several factors, including the dynamics of the analyzed motion, the specifications of the dGNSS hardware and processing algorithms, the GNSS signal shading and reflection, or the terrain and time-specific satellite constellations (Gilgien et al., 2013, 2015). Gilgien et al. (2015) stated an uncertainty of the applied dGNSS method for instantaneous acceleration of $\pm 0.22 \text{ m s}^{-2}$ for alpine giant slalom ski racing for turning where a virtual pendulum was attached to the head compared to a video based system, which usually provide position accuracies of about 0.001 m to 0.022 m (van der Kruk et al., 2018). Since our gliding tests included no turning the error is expected to be much smaller. The major part of the instantaneous acceleration error of $\pm 0.22 \text{ m s}^{-2}$ was associated with the pendulum swing. In this study, the input uncertainty of the acceleration was therefore calculated as $\pm 0.09 \text{ m s}^{-2}$ (Table 2.4), which is about $\pm 5 \%$ of the average acceleration throughout the analyzed gliding section (assuming a *COF* of 0.06). Assuming a one-percent acceleration uncertainty, the propagated *COF* uncertainty would have been reduced from $\pm 30 \%$ to about $\pm 20 \%$.

4.2 Laboratory experiments in the context of the found ski/snowboard-snow friction

Snow samples were prepared over a wide range of properties, representing the range of snow conditions as observed on the field to a sufficient extend concerning density, temperature and wetness. However, the range of *SSA* and other microstructural features was smaller than on real ski slopes. The snow sample preparation showed good reproducibility, but reproducible friction tests were only possible for snow samples with densities above about 350 kg m^{-3} , and after a sufficient time of sintering. The developed snow preparation techniques allow to widen the snow parameter space to higher *SSA* and diverse grain shapes for future laboratory experiments.

There was a general accordance between field and laboratory friction showing a increasing *COF* from coarse to fine-grained snow and from dry to wet snow. Lowest friction was

measured on coarse-grained snow while highest on wet fine-grained snow. However, the found range in the laboratory was narrower than on the field. Especially the lowest *COF* deviated distinctively (0.06 vs. 0.023). Clearly, the lower speed (1 to 2 order of magnitudes) was the major limitation of the tribometer measurements. Moreover, the *COF*-maxima at mid-level *LWC* were surprising and stood in contrast to the on-field results, where the *COF* constantly increased with increasing *LWC* (Fig. 3.1). An explanation of the found *COF*-maxima in the laboratory might be the large gradient of properties within the snow samples due to the melting method using a light source. By that, the *LWC* quickly rose at the top of the snow sample, while parts below were still dry and especially strong. This might have caused very high local deformations and water concentration at the top, leading to a high *COF* due to capillary drag. For coarse-grained snow, the *COF*-peak at mid-level *LWC* was less pronounced as the water started to percolate earlier and deeper into the sample, which weakened the described effect. However, as under natural conditions melting also starts at the surface, similar conditions might occur on a ski slope. Although, the shown increase of the ski-snow friction in Fig. 3.1 give room for interpretation into that direction, in general the field data does not support the existence of a *COF*-peak due to a temporal maximized surface near *LWC* concentration. As the laboratory test setup excluded macroscopic plowing between the slider and the snow as well as compaction (due to the consecutive order of vertical and horizontal movements), *COF* measured in the laboratory did not include those contributions to friction. Another discrepancy between laboratory and field friction data was the found interaction of *SSA* and *LWC*, which caused highest *COF*-values on the field. This was observed much less in the laboratory, which was in parts caused by the smaller range of *SSA* tested in the lab.

Snow under skiing-like loading, was shown to be dominated by irreversible brittle and plastic deformations, but also elastic and viscoelastic deformations were measured. Beyond that, based on a rheological model, viscoplastic deformation were shown to gain relevance on fine-grained wet snow. The total snow deformations were found large enough showing that macroscopic scaled processes of plowing and compaction can become unnegelectable contributors to the ski-snow friction depending on the type and state of the piste snow. The found extend of snow deformations should also be considered concerning its role on the pressure distribution along a ski and possible adaptations of the ski mechanics to optimize those large-scale ski-snow interactions. Snow's compressibility depended on its type and state in an interacting way. Whereas in the dry state snow of lower density and higher *SSA* was less compressible than high-density and coarse one, this changed to the opposite when the snow became wet. Thus, if snow exceeds a certain wetness, not only lubrication is impacted, also friction due to plowing ($COF_{plow} = 0.034$, at 3 mm sinkage, 400 kg m^{-3} and 10 m s^{-1}) and compaction ($COF_{comp} = 0.002$ at 3 mm sinkage) gains relevance. Whereas elastic deformations were generally small appearing mainly relevant for dry snow, viscoelastic deformation fractions and its corresponding relaxation times, were found to peak for low *LWC*-values for all snow types. This might be related with a maximum grain bond mobility at low *LWC* before those bonds entirely weakened and yielded. Interestingly, for all snow types a correlation of the relaxation time with the measured *COF* in the laboratory was found ($r_{pearson} = 0.69$ to 0.77). This suggested that an increased viscoelasticity of snow caused higher friction.

Assumably, high viscoelasticity might occur if the normal force is at most equally distributed over an optimal number of the contact points which allows to maximize grain bond glide, but still is low enough to prevent brittle failure. Concerning friction, this could lead to a higher number of persistent micro-contacts increasing the *RCA*. However, neither contact spots number, nor *RCA* was found to increase disproportional for high viscoelasticity (e.g., for MG snow with *LWC* = 4.5 % as shown in Fig. 3.21). The compression experiments were limited as deformations were only be measured globally as an average over the entire sample. Information of the deformation distribution within the sample were not accessible. In consequence, found deformations could not be distinguished between microscopic contact deformation of ice or macroscopic snow deformations. Further limitations existed as the presented elastic (and viscoelastic) snow deformations could not be separated from contributions of the slider's UHMWPE. Neglecting the viscoelasticity of UHMWPE, elastic Hertzian contact theory as applied by Böttcher et al.(2017) revealed a deformation of the microscopic contact of about 7 μm , assuming a sphere (ice grain) and a cylinder (grinded ski base) as contact bodies ($E_{\text{ice}} = 9500 \text{ MPa}$; $E_{\text{PE}} = 840 \text{ MPa}$; $\nu_1 = 0.31$; $\nu_2 = 0.46$; $r_1 = 0.5 \text{ mm}$; $r_2 = 0.02 \text{ mm}$), and a normal force per contact of 0.3 N according to Theile et al. (2009). This was comparable to the single grain loads estimated from the found number of contact grains on FG snow in chapter 3.2.5. Compared to the measured maximal elastic deformations (40 to 80 μm on dry snow), the Hertzian contact deformations, and so the contribution of the UHMWPE base, were small. However, concerning the ski-snow friction, it is important to point out the interdependence of microscopic contact deformations and macroscopic deformation of the snow matrix, which influences the distribution of load over the contact spots, determine failure of ice grains and grain bonds, which then strikes back on the micro-contact formation. Besides that, small deformations at the contacts (μm) as well as larger deformation of the snow (mm) were both assumed to influence the formation of a lubrication layer. On the scale of microns at the contacts spots, but also on the scale of millimeters concerning the water distribution in the pore space and between the top surface grains of wet snow.

Experiments on the movement of liquid water within snow under compression showed that during the slider-snow contact, water accumulated towards the interface in different degree, depending on the snow type. On fine-grained snow enhanced water accumulations near the ski-snow interface. Besides the water-holding capacity, its high compressibility was identified as a key property. Concerning the ski-snow friction, it is important to point out that the amount of water, which concentrated near the interface exceeded the typical range of volumetric *LWC*-values. For high *LWC*, the thin snow volume at the top surface was likely to be fully saturated, the snow was easy to compress, and the water could not rapidly flow deeper into the snow. The latter also indicated that the rate of snow deformation, which depends on the speed of the skier, might affect water concentrations at the interface. The found relationships of the *COF* with speed as measured on the field supported the theory of meltwater lubrication reducing snow friction, as the *COF* first decreased at lower speeds, followed by an increase at higher speeds (Fig. 3.5). This behavior matches with the idea of changing lubrication regimes due to meltwater generation from frictional heat (Colbeck, 1992). Moreover, the fact that minimum *COF*-values were reached earlier (at lower speeds) on warm or wet snow, whereas on cold snow the minimum occurred at higher speeds, further

aligned with the theory (Table 3.1). However, there is doubt, that the COF-increase at higher speeds might solely be caused by increased hydrodynamic friction ($\sim v$). In particular, the slope of the COF-curves on new snow appeared too steep, suggesting the involvement of additional processes. Due to the high roughness of the snow surface complete wetting of the ski-snow interface should not increase hydrodynamic friction much, as speed gradients in most parts of the interfacial water would be small. Moreover, Hild et al. (2002) showed that viscous forces within water connecting two surfaces became significantly smaller as expected from the hydrodynamic friction law (Eq. 10) if one surface was hydrophobic. However, the found near surface water accumulation under laboratory conditions, as well as the strong increase in friction from dry to wet snow as found on the field (Fig. 3.5 a vs. b & e vs. f) indicated that a high ski-snow friction is related with large amounts of interfacial water. This could strengthen the idea of a drag force caused by water bridges between unloaded grains and the ski base (see chapter 1.3). Similar as for the hydrodynamic friction, hydrophobic surfaces would reduce such friction contributions, as with increasing hydrophobicity also the contact angle hysteresis decreases (Tab. 2.1). However, as long a no detailed observation of the interface is possible, also other mechanisms could be assumed to explain the course of the COF-curves, e.g. an increasing lubricated contact area as a result snow surface deformations. Clearly, the variability of the snow surface topography and the amount of lubricant complicates a full understanding of ski-snow friction. A rough calculation to compare water volumes from frictional melting with water released from the snow to the interface showed that the latter are at least one order of magnitude higher, even when assuming a thick self-generated water film of 10 μm over a large contact area of 6 % compared to a low *LWC* of only 1 %. Colbeck (1988) proposed the capillary drag to increase as h^3 multiplied by a constant representing the snow conditions. Water available for capillary bridges only included self-generated water removed from the bearing contacts. Based on the findings in the laboratory, interface near water increased approximately with $LWC^{\frac{1}{n}}$, where n described the tested snow conditions between about 0.5 (CG) and 0.8 (FG). Regarding the COF-parametrization from field data, this corresponds to the mixed term of *SSA* and *TLWC*, representing the interactive impact of these two snow properties on the snow friction. The liquid water redistribution experiments were limited as the measured capacitance did provide an estimate on water concentration near the interface, but not an exact quantification of the fraction of wetted interface. A precise comparison of the different water sources in the frictional contact is still lacking. Addressing this limitation, preliminary tests with simple water finder test paper appeared promising and worth to be elaborated for compression test without horizontal movement of the slider.

The analysis of the snow samples before and after the compressive contact using μCT measurements gave two important insights. First, the data revealed the depth of water percolation before and after the contact as well as an exact quantification of the snow sample densification. This pointed out that water contributed to the strong densification at the top of FG and MG snow samples, while for CG snow, water percolated distinctively deeper into the sample and therefore concentrated less at the top. By that, deformations and water accumulation deduced from permittivity and displacement measurements were confirmed and important information on their spatial distributions was added, showing that the finer the snow microstructure was, the more deformation and water occurred towards the slider-snow interface.

Second, μ CT-scans revealed the snow surface topographies as formed during the contact of the slider on various types and states of snow. This allowed to estimate the RCA_{rel} ranging from about 2 to 6 % distributed over approximately 0.3 to 1.6 contact spots per mm^2 . The size of these contacts spots widely ranged between 0.01 and 1 mm^2 . On average the contact sizes were about one order of magnitude smaller than the snow grains. Concerning the formation of the slider-snow contacts, the idea of the microscopic contact which forms under deformation of the softer contact body until the loading force equilibrates the product of compression strength and (absolute) RCA_{rel} (Persson and Tosatti, 1996), appeared transferable to the snow-ski contact where brittle failure of snow and plastic deformation of ice grains form a contact area large enough to counteract the skier's load. This was supported as the found contact stresses deduced from the RCA_{rel} matched well with the compressive strength of snow as expressed by the measured compression modulus or found in the literature (chapter 1). However, plastic deformation of ice grains would require contact stresses one order of magnitude higher. Compared to a RCA_{rel} of an elasto-plastic material, which manifest on the smaller scale of the roughness of a tribological surface, the linear elastic deformation at the beginning of the contact corresponds to the brittle quasi-plastic compression of the snow. During that phase, assumably higher stresses and therefore ice grain deformation likely occurred. Concerning friction, the found RCA_{rel} could be plausibly related with measured COF in the laboratory. Whereas the impact of the LWC on the RCA_{rel} was weak, the RCA_{rel} about tripled from CG to FG snow. On FG snow, up to mid-level LWC , the COF was clearly (30 to 10 %) higher than on CG snow due to increased dry friction and because of smaller contact pressure generating less heat, less frictional melting, and in consequence worse lubrication. Related to the ski-snow friction field data, higher COF on snow of higher SSA (Fig. 3.4) let assume, that the formation of a larger RCA_{rel} is involved. As the SSA on the field were up to a factor of three higher as the FG snow from the laboratory, RCA_{rel} were likely to exceed 10 %. The formation of a large SSA on such snow in combination with the disadvantageous effects on water (worse removal of generated water due to missing drainage space, more concentration of existing water) could also explain the strong COF -increase with speed as shown in Figure 3.5 e and f.

As summarized in chapter 1, calculations and measurements of the RCA_{rel} on snow have been reported from permilles (e.g. Böttcher, 2015; Scherge et al., 2021) to high values up to 9 % (Hasler et al., 2022). The latter study also showed the change of RCA_{rel} from several passes on the same snow track with the RCA_{rel} increasing with increasing snow temperatures and number of runs (9 to 27 % at -1°C ; 2 to 4 % at -19°C). Contact spot sizes have been reported in a similar range as presented above between 0.01 and 0.4 mm from measurements (Bäuerle, 2006), and about 0.01 mm from models (Theile et al., 2009). Colbeck (1988) envisioned the contact spot size for his calculations clearly larger as found here (ca. 3 mm^2). A strong simplification behind the above presented values is the assumption of a perfectly smooth slider. The RCA_{rel} with a slider with a typical roughness of a ski base would be expected to be significantly smaller. Böttcher (2015) approximated this decrease of RCA_{rel} (with Hertzian contacts) from a flat to a grinded base on snow by a factor of about ten (0.2 % vs. 0.02 %). Bäuerle (2006) whose most reliable values laid around 7 %, as well as Hasler et al. (2022) followed a similar approach as applied here, by assuming a plane or a

thin vertical zone as contact plane. As visible in Figure 3.20 to 3.22, there were also surface elements above and below the identified contact plane, which might have been created by the snow-slider contact. Maybe from ice particles or water droplets pulled-up during separation of slider and snow, due to deviations from planarity between the two surfaces, or as an effect of elastic or viscoelastic relaxation. The approach applied within this study, using the discrete distributions of horizontal surface elements of the mesh model of the snow revealed plausible results compared to the literature. However, a detailed proof of the method's reliability is still needed. Further methodological limitations were the low number of scans of the different snow configurations, the time (hours) between slider-snow contact and scan, which allowed further water percolation and wet snow metamorphism, as well as the missing horizontal movements excluding impacts of wear and frictional melting on the contact formation. To literally freeze the contact situation at the moment of interaction shock freezing the snow under load could be an improvement of the experimental setup. Preliminary experiments using pressure films (Prescale 4LW, Fujifilm Europe GmbH) between the slider and the snow surface were discarded as the lower limit of pressure were too high and the necessary time of contact too long.

4.3 Practical implications

*The following paragraph is part of the publication: Wolfsperger, F., Meyer, F., Gilgien, M., 2021. The snow-friction of freestyle skis and snowboards predicted from snow physical quantities. *Frontiers in Mechanical Engineering*, 7, 728722.*

This study has presented, for the first time, a data set that describes the snow friction for freestyle skis and snowboards for a full range from very fast gliding snow conditions to excessively slow ones. It was shown that snow friction can vary considerably from day to day, but also can change within hours. For Olympic freestyle disciplines like slopestyle or big air, it is important to understand this variability as it strongly affects the take-off speed at jumps and therefore determines whether athletes land with low impact in the sweet-spot zone or jump too far or too short, risking severe injuries. Now, based on the findings of this research, the *COF* can be predicted from the prevailing snow physical properties, which can be measured using available and affordable instruments or calculated using numerical snowpack and weather models (Lehning et al., 2006; Hanzer et al., 2020). For that purpose, practitioners should use the shown multi-parameter COF-models given in equation 3.1 and 3.2. The precise calculation of snow friction depending on the weather and snow at a specific venue will help course builders to improve the design of snow parks from a safety point of view, and give organizers of freestyle events the ability to anticipate diurnal changes in snow friction and thus injury risk.

Moreover, the COF-parametrization can be used as an improved input function for mechanical jump design models (e.g. McNeil et al., 2012), including gravity, friction and aerodynamic forces during in-run and flight phase. In addition, the mechanical characterization of snow under compression, can be used to improve the calculation of landing kinetics due to an elaborated description of the force-deformation relation (Wolfsperger et al., under review).

5 Conclusion

Snow was found as the dominating factor of ski-snow friction, mainly because of its variable nature and its quickly changing physical properties. Relating the dominating influence of snow with measurable and predictable snow physical quantities is of practical use as the kinematics and kinetics of a skier can now be calculated much more precisely. The interaction of the snow parameters and their complex role within the various processes of snow friction were found crucial to understand the extend of friction a skier experiences on snow. To explain the huge changes of friction from the lowest *COF* on frozen spring snow to highest values on very wet new snow, five mechanisms of particular importance were identified, based on both, field and the laboratory data:

- (1) The dominating mode and extent of snow deformation under the skier's load, which is determined by the mechanical properties of the snow. Even on groomed snow, macroscopic compaction and plowing can get relevant.
- (2) The found relationships of the *COF* with speed confirmed self-lubrication from frictional heating as a dominating process. The *COF* first decreased at lower speeds, followed by an increase at higher speeds. Minimum *COF*-values were reached earlier (at lower speeds) on warm or wet snow, whereas on cold snow the minimum occurred at higher speeds.
- (3) The formation of solid-to-solid contacts between the ski and the snow, their mechanical interaction, and the resulting real contact area, which manifests on the micro- and the macroscale. Elevated friction of fine-grained snow results from an increased real contact area which impacts dry and hydrodynamic friction.
- (4) The assumption of a capillary drag force due to water bridges connecting unloaded grains with the ski base. This depends on the amount and distribution of water at the ski-snow interface, which moves from the snow pores to the interface depending on the type and state of the snow. The idea of a capillary drag force was strengthened by the strong increase in friction for higher speeds on wet snow, or on snow with a fine microstructure limiting water moving away from the interface.
- (5) Highest friction on wet new snow results from the concurrent increase of real contact area and interfacial water and increases both, hydrodynamic friction as well capillary drag.

Concerning the optimization of the skis and snowboards, the findings of this study indicated the need of highly hydrophobic gliding surface as unfavorable snow conditions facilitating

large amounts of interfacial water. However, rough ski base topographies, which are typically used on wet snow are not promising for very sticky wet-new-snow conditions. Neither the provided water retention spaces have an effect, nor a smaller real contact area is assumed to be achieved, as a consequence of the sponge-like behavior of such snow. For elite sports these snow physical boundary conditions, combined with the climatological tendency to more wet snow conditions and the recent ban of flour based waxes makes the tasks of preparing fast skis increasingly difficult.

Future research on the ski-snow friction should use experimental and modeling methods which enable to measure and represent the mechanics of the ski-snow contact realistically for relevant snow and kinematical conditions. A promising approach might include discrete element or material point methods, which are able to model the visco-elastic-plastic behavior of snow under load including the transition from a porous to a granular material behavior as well as cohesion between single ice grains. Based on existing and the newly found insights into the dependency of the ski-snow friction on snow parameters and its governing processes, it is promising that modeling approaches will help to deliver a more realistic representation of the ski-snow contact morphology, which then can be used as the basis of a thermodynamic and hydrodynamic friction model. However, the implementation of the interaction of liquid water with the ice matrix within a quickly compressed snow volume, will require markedly efforts.

Bibliography

Ambach, W., Mayr, B., 1981. Ski gliding and water film. *Cold Regions Science and Technology* 5, 59-65. doi: 10.1016/0165-232X(81)90040-9.

Armstrong, R.L., Brun, E., 2008. *Snow and Climate: Physical Processes, Surface Energy Exchange and Modeling*, Edited by R. Cambridge University Press.

Anderson, D. L., Benson, C. S., 1963. The densification and diagenesis of snow. In *Ice and Snow: Properties, Processes and Applications*. Eds. Kingery, W. D., 391-411, MIT Press, Cambridge, MA.

Barnes, P., Tabor, D., Walker, J.C.F., 1971. The friction and creep of polycrystalline ice. *Proceedings of the Royal Society of London. A. Mathematical and Physical Sciences* 324, 127155. doi: 10.1098/rspa.1971.0132.

Batto, R., Schulson, E., 1993. On the ductile-to-brittle transition in ice under compression. *Acta Metallurgica et Materialia* 41, 22192225. doi: 10.1016/0956-7151(93)90391-5.

Bäuerle, L., 2006. Sliding friction of polyethylene on snow and ice. Dissertation at ETH Zürich. URL: <https://www.research-collection.ethz.ch/handle/20.500.11850/149368>.

Beitz, W., Grote, K.H., 2001. *Taschenbuch für den Maschinenbau*. Edition: 20. Ausgabe, Springer.

Bianchi, G., Brügger, O., Niemann, S., 2016. Verletzentransporte im Schneesport. bfu Beratungsstelle für Unfallverhütung 2015. doi: 10.13100/bfu.2.283.01.

Blackford, J.R., 2007. Sintering and microstructure of ice: a review. *Journal of Physics D: Applied Physics* 40, 355-385. doi: 10.1088/0022-3727/40/21/R02.

Bowden, F., 1953. Friction on snow and ice. *Proceedings of the Royal Society of London* 217, 462.

Bowden, F.P., Hughes, T., 1939. The mechanism of sliding on ice and snow, R. Soc. Lond. doi: 10.1098/rspa.1939.0104.a172280-298.

Bibliography

Bowden, F.P., Tabor, D., 1950. The Friction and Lubrication of Solids. Volume 1. Clarendon Press.

Bowden, F.P., Tabor, D., 1966. Friction, lubrication and wear: a survey of work during the last decade. *British Journal of Applied Physics* 17, 1521-1544.
doi: 10.1088/0508-3443/17/12/301.

Budde, R., Himes, A., 2017. A high-resolution friction measurements of cross-country ski bases on snow. *Sports Eng* 20, 299-311. doi: 10.1007/s12283-017-0230-5.

Buhl, D., Fauve, M., Rhyner, H., 2001. The kinetic friction of polyethylene on snow: the influence of the snow temperature and the load. *Cold Reg. Sci. Technol.* 33, 133-140.
doi: 10.1016/S0165-232X(01)00034-9.

Böttcher, R., 2015. Zur Tribologie von strukturierten Skibelägen auf Eis und Schnee. Dissertation at the Department of Mechanical Engineering at the Karlsruhe Institute of Technology.

Böttcher, R., Seidelmann, M., Scherge, M., 2017. Sliding of UHMWPE on ice: Experiment vs. modeling, cold regions science and technology. Volume 141, 171180.
doi: 10.1016/j.coldregions.2017.06.010.

Canale, L., Comtet, J., Nigues, A., Cohen, C., Clanet, C., Siria, A., et al., 2019. Nanorheology of interfacial water during ice gliding. *Phys. Rev. X*.
doi: 10.1103/PhysRevX.9.041025.

Carlson, G.L., Tupper, S., 2020. Ski wax use contributes to environmental contamination by per- and polyfluoroalkyl substances. *Chemosphere* 261, 128078.
doi: 10.1016/j.chemosphere.2020.128078.

Carter, D., 1970. Brittle fracture of snow ice, IAHR. 521-528.

Colbeck, S.C., 1992. A review of the processes that control snow friction. Monograph 92-2. Cold Regions Research and Engineering Laboratory. URL:
<https://erdc-library.erdc.dren.mil/jspui/handle/11681/2667>.

Colbeck, S.C., 1988. The kinetic friction of snow. *Journal of Glaciology* 34 , 78-86.
doi: 10.3189/s0022143000009096

Bibliography

Colbeck, S.C., 1994. An error analysis of the techniques used in the measurement of high-speed friction on snow. *Annals of Glaciology* 19, 1924. doi: 10.3189/1994AoG19-1-19-24.

Colbeck, S.C., Parssinen, N., 1978. Regelation and the deformation of wet snow. *Journal of Glaciology* 21, 639-650. doi: 10.1017/S002214300003375X.

CPS-GmbH, 2022a.datasheet: 2000_HC_P-tex_DS_clear_v081117. URL: https://www.cps-gmbh.net/download/datenblaetter/5188_P-tex_black_v110418.pdf

CPS-GmbH, 2022b. datasheet: 5188_P-tex_black_v110418. URL: https://www.cps-gmbh.net/download/datenblaetter/2000_HC_P-tex_DS_clear_v081117.pdf

D'Amico, M., Ferrigno, G., 1992. Comparison between the more recent techniques for smoothing and derived assessments in biomechanics. *Med. Biol. Eng. Comput.* 30, 193-208. doi: 10.1007/BF02446130.

Denoth, A., 1994. An electronic device for long-term snow wetness recording. *Annals of Glaciology* 19, 104-106. doi: 10.1017/S0260305500011058.

Denoth, A., 1989. Snow dielectric measurements. *Adv. Space Res.* 9: 233-243.

Dosch, H., Lied, A., Bilgram, J., 1995. Glancing-angle x-ray scattering studies of the premelting of ice surfaces. *Surface Science* 327, 1451-64. doi: 10.1016/0039-6028(94)00801-9.

Döppenschmidt, A., Butt, H.J., 2000. Measuring the thickness of the liquid-like layer on ice surfaces with atomic force microscopy. *Langmuir* 16, 6709-6714. doi: 10.1021/la990799w.

Eberts, C., 2014. Westen wendet sich von olympia ab. URL: <https://www.sueddeutsche.de/sport/oslo-sagt-nein-zu-winterspielen-2022-westen-wendet-sich-von-olympia-ab-1.2156925>.

Evans, D., Nye, J., Cheeseman, K., 1976. The kinetic friction of ice. *Proc. R. Soc. A Math. Phys. Sci.* 347, 493-512.

Fauve, M., Buhl, D., Rhyner, H., Schneebeli, M., Ammann, W., 2005. Influence of snow and weather characteristics on the gliding properties of skis. In *Science and Skiing III*. Aspen: Meyer & Meyer Sport.

Bibliography

Fierz, C., Armstrong, R.L., Durand, Y., Etchevers, P., Greene, E., McClung, D.M., et al., 2009. The international classification of seasonal snow on the ground. IHP-VII Technical Documents in Hydrology No. 83, IACS Contribution No. 1, UNESCO-IHP, Paris.

Finstad, E., Martinsen, J., Hole, R., Pilo, L., 2018. Prehistoric and medieval skis from glaciers and ice patches in Norway. *Journal of Glacial Archaeology* 3, 43-58. doi: 10.1558/jga.33147.

Florene, T.W., Heir, S., Nordsletten, L., Bahr, R., 2010. Injuries among world cup freestyle skiers. *British Journal of Sports Medicine* 44, 803-808.

Florene, T.W., Nordsletten, L., Heir, S., Bahr, R., 2011. Recording injuries among world cup skiers and snowboarders: a methodological study. *Scandinavian Journal of Medicine Science in Sports* 21, 196-205.

FPGA Company GmbH, 2018. SLF Snow Sensor - user manual. URL: <https://fpga-company.com/wp-content/uploads/2018/12/SLFSnowSensor-User-Manual-Version-1.4.pdf>.

Fukue, M., 1979. Mechanical performance of snow under loading. Dissertation. Tokai University Press.

Gergely, M., Wolfsperger, F., Schneebeli, M., 2014. Simulation and validation of the infrasnow: an instrument to measure snow optically equivalent grain size. *IEEE Transactions on Geoscience and Remote Sensing* 52, 4236-4247. doi: 10.1109/TGRS.2013.2280502.

Gerling, B., Löwe, H., van Herwijnen, A., 2017. Measuring the elastic modulus of snow. *Geophysical Research Letters* 44. doi: 10.1002/2017GL075110.

Gilgien, M., Spörri, J., Chardonnens, J., Kröll, J., Müller, E., 2013. Determination of External Forces in alpine Skiing Using a Differential Global Navigation Satellite System. *Sensors* 13, 9821-9835. doi: 10.3390/s130809821.

Gilgien, M., Spörri, J., Chardonnens, J., Kröll, J., Limpach, P., Müller, E., 2015. Determination of the centre of Mass Kinematics in alpine Skiing Using Differential Global Navigation Satellite Systems. *J. Sports Sci.* 33, 960-969. doi: 10.1080/02640414.2014.977934.

Glenne, B., Gorlin, M., Maseev, W., Zyrjanov, W., Remizov, L., 1987. Sliding friction and boundary lubrication of snow. *J. Tribol.* 109, 614-617. doi: 10.1115/1.3261520.

Bibliography

Bader, R., 1954. Snow and Its Metamorphism. In: Mineralogical and structural characterization of snow and its metamorphism. Eds. H. Bader, R. Haefeli, E. Buchker, J. Neher, O. Eckel, and C. Thams. Beiträge zur Geologie der Schweiz, Geotechnische Serie, Hydrologie, Bern, 1-55.

Habel, B., 1968. Über die Bestimmung von Luftwiderstand und Gleitreibung beim Skilauf. Europa Sport 20, 950-955.

Hagenmuller, P., Matzl, M., Chambon, G., Schneebeli, M., 2016. Sensitivity of snow density and specific surface area measured by microtomography to different image processing algorithms. The Cryosphere 10, 1039-1054. doi: 10.5194/tc-10-1039-2016.

Hanzer, F., Carmagnola, C.M., Ebner, P.P., Koch, F., Monti, F., Bavay, M., Morin, S., 2020. Simulation of snow management in alpine ski resorts using three different snow models. Cold Regions Science and Technology 172, 17. doi: 10.1016/j.coldregions.2020.102995.

Hasler, M., Mössner, M., Jud, W., Schindelwig, K., Guer, M., van Putten, J., Rohm, S., Nachbauer, W., 2022. Wear of snow due to sliding friction. Wear 510-511, 204-499. doi: 10.1016/j.wear.2022.204499.

Hasler, M., Schindelwig, K., Knoach, C., Reichl, W., Nachbauer, W., 2014. Kinetic friction of boardercross-snowboards. Procedia Engineering 72, 310-314. doi: 10.1016/j.proeng.2014.06.054.

Hasler, M., Schindelwig, K., Mayr, B., Knoach, C., Rohm, S., van Putten, J., et al., 2016. A novel ski-snow tribometer and its precision. Tribol. Lett. 63. doi: 10.1007/s11249-016-0719-2.

Haynes, F. D., 1978. Effect of temperature on the strength of snow-ice. Report 78-27. Cold Regions Research and Engineering Laboratory.
URL: <https://apps.dtic.mil/sti/pdfs/ADA067583.pdf>.

Heer, B., Bürgi, F., Weiler, M., 2019. Snowparks: Sicherheitsaspekte bei Planung, Bau und Betrieb. Fachdokumentation Beratungsstelle für Unfallverhütung BFU, Bern.

Henrie, M., Petron, D.J., Pepper, M., Kirkham, J., Chen, Q., Willick, S., 2010. Comparison of ski and snowboard injuries that occur inside versus outside terrain parks: 2001. Medicine Science in Sports Exercise 42, 473-474. doi: 10.1249/01.MSS.0000385054.56383.47.

Bibliography

Hild, W., Schaefer, J.A., Scherge, M., 2002. Microhydrodynamical studies of hydrophilic and hydrophobic surfaces. In Lubricants, Materials, and Lubrication Engineering, International Colloquium Tribology, 13, 821-825.

Hock, R., Morin, S., Adler, C., 2022. High mountain areas. The Ocean and Cryosphere in a Changing Climate. doi: 10.1017/9781009157964.004.

Hock, R., G. Rasul, C. Adler, B. Cáceres, S. Gruber, Y. Hirabayashi, M. Jackson, A. Kääb, S. Kang, S. Kutuzov, Al. Milner, U. Molau, S. Morin, B. Orlove, and H. Steltzer, 2019. High Mountain Areas. In: IPCC Special Report on the Ocean and Cryosphere in a Changing Climate. Eds. H.-O. Pörtner, D.C. Roberts, V. Masson-Delmotte, P. Zhai, M. Tignor, E. Poloczanska, K. Mintenbeck, A. Alegria, M. Nicolai, A. Okem, J. Petzold, B. Rama, N.M. Weyer. Cambridge University Press, Cambridge, UK and New York, NY, USA, 131-202. doi: 10.1017/9781009157964.004.

Hu, W., Wu, B., Srivastava, S.K., Ay, S.U., 2022. Comparative study and simulation of capacitive sensors in microuidic channels for sensitive red blood cell detection. *Micromachines* 13, 16-54. doi: 10.3390/mi13101654.

Hu, X., Yang, W., 2010. Planar capacitive sensors - designs and applications. *Sensor Review* 30, 24-39. doi: 10.1108/02602281011010772.

Hubbard, M., McNeil, J., Petrone, N., Cognolato, M., 2015. Impact performance of standard tabletop and constant equivalent fallheight snow park jumps. *Skiing Trauma and Safety* 20. ASTM International. 51-71. doi: 10.1520/STP15822014002.

Huzioka, T., 1962. Studies on the resistance of a snow sledge, 5. Friction between snow and a plastic plate. *Low Temperature Science*, A20: 159-180.

Kaps, P., Nachbauer, W., Mossner, M., 1996. Determination of Kinetic Friction and Drag Area in alpine Skiing. In *Skiing Trauma and Safety*. Eds. C. Daniel Mote, R. J. Johnson, W. Hauser, and P. S. Schaff. West Conshohocken, PA: ASTM International, 10, 165-177.

Kawashima, K., Endo, T., Takeuchi, Y., 1998. A portable calorimeter for measuring liquid-water content of wet snow. *Annals of Glaciology* 26, 103-106. doi: 10.3189/1998AoG26-1-103-106.

Kinosita, S., 1967. Compression of snow at constant speed. Institute of Low Temperature Science, Hokkaido University. 911-927. URL: <http://hdl.handle.net/2115/20350>.

Koerkamp, G.G., 2014. Sochi's environment in danger.
URL: <https://www.dw.com/en/olympic-winter-games-have-damaging-effect-on-sochis-environment/a-17449525>.

van der Kruk, E., Reijne, M.M., van der Kruk E., Reijne, M.M., 2018. Accuracy of human motion capture systems for sport applications: state-of-the-art review. *Eur J Sport Sci.* 18, 806819. doi: 10.1080/17461391.2018.1463397.

Kuroiwa, D., 1977. The kinetic friction on snow and ice. *J. Glaciol.* 19, 141-152.

Lehning, M., Völksch, I., Gustafsson, D., Nguyen, T.A., Stähli, M., Zappa, M., 2006. Alpine3d: a detailed model of mountain surface processes and its application to snow hydrology. *Hydrological Processes* 20. 2111-2128. doi: 21112128. 10.1002/hyp.6204.

Lehtovaara, A., 1989. Kinetic friction between ski and snow. *Acta Polytechnica Scandinavica, Mechanical Engineering* 93.

Leino, M.A.H., Spring, E., 1984. Determination of the coefficient of kinetic friction between ski and snow from gliding velocity of a skier. *Report Series in Geophysics* 19. University of Helsinki.

Lever, J., Taylor, S., Hoch, G., Daghlian, C., 2019. Evidence that abrasion can govern snow kinetic friction. *Journal of Glaciology* 65, 68-84. doi: 10.1017/jog.2018.97.

Lever, J.H., Asenath-Smith, E., Taylor, S., Lines, A.P., 2021. Assessing the mechanisms thought to govern ice and snow friction and their interplay with substrate brittle behavior. *Frontiers in Mechanical Engineering* 7. doi: 10.3389/fmech.2021.690425.

Levy, D., Hubbard, M., McNeil, J., Swedberg, A., 2015. A design rationale for safer terrain park jumps that limit equivalent fall height, 227-239. doi: 10.1007/s12283-015-0182-6.

Li, Y., Somorjai, G.A., 2007. Surface premelting of ice. *The Journal of Physical Chemistry C* 111(27), 9631-9637. doi: 10.1021/jp071102f.

Lind, D., Sanders, S., 2004. *The Physics of skiing: Skiing at the Triple Point.* 2nd ed., Springer.

Lintzen, N.; Edeskär, T., 2014. Uniaxial Strength and Deformation Properties of Machine-Made Snow. *J. Cold Reg. Eng.* 29: 4. doi: 10.1061/(ASCE)CR.1943-5495.0000090.

Löwe, H., Zaiser, M., Mössinger, S., Schleef, S., 2020. Snow mechanics near the ductile-brittle transition: Compressive stick-slip and snow microquakes. *Geophysical Research Letters* 47(4). doi: 10.1029/2019GL085491.

Makkonen, L., 1994. Application of a new friction theory to ice and snow. *Ann. Glaciol.* 19, 155-157.

Makkonen, L., Tikanmäki, M., 2014. Modeling the friction of ice. *Cold Regions Science and Technology* 102, 84-93. doi: 10.1016/j.coldregions.2014.03.002.

Marty, C., Schlägl, S., Bavay, M., Lehning, M., 2017. How much can we save? impact of different emission scenarios on future snow cover in the alps. *The Cryosphere* 11, 517-529. doi: 10.5194/tc-11-517-2017.

McNeil, J.A., Hubbard, M., Swedberg, A., 2012. Designing tomorrow's snow park jump. *Sports Engineering* 15(1), 1-20. doi: 10.1007/s12283-012-0083-x.

Mellor, M., 1975. A review of basic snow mechanics, IAHS. pp. 251-291. IAHS Publ., 114.

Mitterer, C., Schweizer, J., 2014. Comparing models of different levels of complexity for the prediction of wet-snow avalanches. *International snow science workshop proceedings* 2014, 9-14.

Nachbauer, W., Kaps, P., Hasler, M., Mössner, M., 2016. Friction between Ski and Snow. In: the Engineering Approach to Winter Sports. Eds. Braghin, F. Cheli, S. Maldifassi, S. Melzi, and Sabbioni, E., New York, Springer, 17-32. doi: 10.1007/978-1-4939-3020-3_2.

Nachbauer, W., Schröcksnadel, P., Lackinger, B., 1996. Effects of Snow and Air Conditions on Ski Friction. In *Skiing Trauma and Safety*. Eds. C. Daniel Mote, R. J. Johnson, W. Hauser, and P. S. Schaff. West Conshohocken, PA: ASTM International, 10, 178-185.

Nagata, Y., Hama, T., Backus, E.H.G., Mezger, M., Bonn, D., Bonn, M., Sazaki, G., 2019. The surface of ice under equilibrium and none-quilibrium conditions. *Accounts of Chemical Research* 52. doi: 10.1021/acs.accounts.8b00615.

Nansen, F., 1891. Pa Ski over Gronland. URL: <http://archive.org/details/firstcrossingofg00nansiala/page/viii/mode/2up?view=theater>.

Niang, M., Bernier, M., Stacheder, M., Brandelik, A., van Bochove, E., 2006. Influence of snow temperature interpolation algorithm and dielectric mixing-model coefficient on density and liquid water content determination in a cold seasonal snow pack. *Subsurface Sensing Technologies and Applications* 7(1), 1-22. doi: 10.1007/s11220-006-0020-9.

Oksanen, P., Keinonen, J., 1982. The mechanism of friction of ice. *Wear* 78, 315-324. doi: 10.1016/0043-1648(82)90242-3.

Persson, B., Tosatti, E., 1996. *Physics of Sliding Friction*. doi: 10.1007/978-94-015-8705-11.

Petrenko, V.F., 1994. The surface of ice. Special report 94-22. Cold Regions Research and Engineering Laboratory.
URL: <https://erdc-library.erdc.dren.mil/jspui/bitstream/11681/12326/1/SR-94-22.pdf>.

Petrenko, V.F., Whitworth, R.W., 2002. *Physics of Ice*. Oxford University Press. doi: 10.1093/acprof:oso/9780198518945.001.0001.

Petrovic, J.J., 2003. Review mechanical properties of ice and snow. *Journal of Materials Science* 38(16). doi: 10.1023/A:1021134128038.

Pittenger, B., Fain, S.C., Cochran, M.J., Donev, J.M.K., Robertson, B.E., Szuchmacher, A., Overney, R.M., 2001. Premelting at ice-solid interfaces studied via velocity-dependent indentation with force microscope tips. *Physical Review B* 63, 134-142. doi: 10.1103/PhysRevB.63.134102.

Poirier, L., Lozowski, E.P., Thompson, R.I., 2011. Ice hardness in winter sports. *Cold Regions Science and Technology* 67, 129-134. doi: 10.1016/j.coldregions.2011.02.005.

Popov, V.L., 2015. *Kontaktmechanik und Reibung*. Springer Berlin Heidelberg. doi: 10.1007/978-3-662-45975-1.

Rohm, S., Unterberger, S.H., Hasler, M., Guer, M., van Putten, J., Lackner, R., et al., 2017. Wear of ski waxes: Effect of temperature, molecule chain length and position on the ski base. *Wear* 384, 43-49. doi: 10.1016/j.wear.2017.05.004.

Rosenberg, R., 2005. Why is ice slippery? Physics Today 58, 50-54.
doi: 10.1063/1.2169444.

Salm, B., 1982. Mechanical properties of snow. Reviews of Geophysics 20, 1.
doi: 10.1029/RG020i001p00001.

Scherge, M., Stoll, M., Moseler, M., 2021. On the influence of microtopography on the sliding performance of cross country skis. Frontiers in Mechanical Engineering 7.
doi: 10.3389/fmech.2021.659995.

Schindelwig, K., Hasler, M., van Putten, J., Rohm, S., Nachbauer, W., 2014. Temperature below a gliding cross country ski. Procedia Engineering 72, 380-385.
doi: 10.1016/j.proeng.2014.06.065.

Schindelwig, K., Platzer, H.P., Mössner, M., Nachbauer, W., 2019. Safety recommendations of winter terrain park jumps into airbags. Journal of Science and Medicine in Sport 22. doi: 10.1016/j.jsams.2018.09.229.

Schleef, S., Jaggi, M., Löwe, H., Schneebeli, M., 2014. An improved machine to produce nature-identical snow in the laboratory. Journal of Glaciology 60, 94102.
doi: 10.3189/2014JoG13J118.

Schulson, E.M., 2009. Fracture of ice and other coulombic materials.
doi: 10.1007/978-3-642-03578-48.

Scott, D., Knowles, N.L.B., Ma, S., Rutty, M., Steiger, R., 2023. Climate change and the future of the Olympic Winter Games: athlete and coach perspectives. Current Issues in Tourism 26, 480 -495. doi: 10.1080/13683500.2021.2023480.

Shapiro, L.H., Johnson, J.B., Sturm, M., Blaisdell, G.L., 1997. Snow mechanics: review of the state of knowledge and applications. Report 97-3. Cold Regions Research and Engineering Laboratory.
URL: <http://cgiss.boisestate.edu/~hpm/SnowIcePhysics/Shapiro&al97.pdf>.

Shealy, J., Stone, F., 2008. Tabletop jumping: engineering analysis of trajectory and landing impact. J. ASTM Int. 5(6), 1-6.

Skaloud, J., Limpach, P., 2003. Synergy of CP-DGPS, Accelerometry and Magnetic Sensors for Precise Trajectography in Ski Racing. In Proceedings of the IONGPS (Salt Lake City: UT, USA).

SLF, 2021. SLF IMIS Weather Stations. URL:
https://www.slf.ch/avalanche/stations/IMIS_WFJ2_EN.pdf.

SLF, 2014. Abschlussbericht Skischliffe. Internal report. WSL - Institute for Snow and Avalanche Research SLF. Davos.

Slater, B., Michaelides, A., 2019. Surface premelting of water ice. *Nature Reviews Chemistry* 3, 172-188. doi: 10.1038/s41570-019-0080-8.

Slotfeldt-Ellingsen, D., 1979. Hvorfor er is og sno glatt? (why are ice and snow slick?). SIF Rapport 79 04 03-1.

Soligard, T., Palmer, D., Steen, K., Lopes, A.D., Grant, M.E., Kim, D., Lee, S.Y., Salmina, N., Toresdahl, B.G., Chang, J.Y., Budgett, R., Engebretsen, L., 2019. Sports injury and illness incidence in the Pyeongchang 2018 Olympic Winter Games: A prospective study of 2914 athletes from 92 countries. *British Journal of Sports Medicine*. doi: 10.1136/bjsports-2018-100236.

Spandre, P., Francois, H., Verfaillie, D., Lafaysse, M., Déqué, M., Eckert, N., George, E., Morin, S., 2019. Climate controls on snow reliability in french alps ski resorts. *Scientific Reports* 9, 8043. doi: 10.1038/s41598-019-44068-8.

Sundu, K., Ottersberg, R., Jaggi, M., Löwe, H., 2023. A grain-size driven transition in the deformation mechanism in slow snow compression. *Acta Materialia*, Volume 262, 2024, 119359. doi: 10.1016/j.actamat.2023.119359.

Swaren, M., Karlöf, L., Holmberg, H.C., Eriksson, A., 2014. Validation of test setup to evaluate glide performance in skis. *Sports Technology* 7, 89-97. doi: 10.1080/19346182.2014.968164.

Szabo, D., Schneebeli, M., 2007. Subsecond sintering of ice. *Appl. Phys. Lett.* 90, 151916. doi: 10.1063/1.2721391.

Taylor, J.E., 2015. Skiing into modernity: A cultural and environmental history. *The Journal of Interdisciplinary History* 46(3), 435-436. doi: 10.1162/JINH_r_00871.

Theile, T., Schneebeli, M., 2011. Algorithm to decompose three-dimensional complex structures at the necks: tested on snow structures. *IET Image Processing*, 5(2), 132-140. doi: 10.1049/iet-ipr.2009.0410.

Bibliography

Theile, T., Szabo, D., Luthi, A., Rhyner, H., 2009. Mechanics of the ski—snow contact. *Tribol.Lett.* 36, 223-231. doi: 10.1007/s11249-009-9476-9.

Vanat, L., 2020. 2020 international report on snow mountain tourism. URL: <https://www.vanat.ch/RM-world-report-2020.pdf>.

Wakahama, G., 1968. The metamorphism of wet snow. In proceedings of IUGG, IAHS General Assembly of Bern, 370-379.

Wakahama, G., 1975. The role of melt-water in densification processes of snow and firn, pp. 6672.

Wang, E., Fu, X., Han, H., Liu, X., Xiao, Y., Leng, Y., 2021. Study on the mechanical properties of compacted snow under uniaxial compression and analysis of influencing factors. *Cold Regions Science and Technology* 182, 103215. doi: 10.1016/j.coldregions.2020.103215.

Willibald, C., Dual, J., Schneebeli, M., Löwe, H., 2021. Size controls on the crossover from normal to self-inhibited sintering of ice spheres. *Acta Materialia* 213, 116926. doi: 10.1016/j.actamat.2021.116926.

Wolfsperger, F., Heer, B., Hüsler, A., Bruhin, B., Gander, M. Design parameters and landing impacts of terrain park jumps in Switzerland. Under review of the Journal of Science and Medicine in Sport. Resubmitted on 30th Oct. 2023.

Wolfsperger, F., Hinterberger, B., Christian, J., Matzl, M., Jahnel, R., Spörri, J., Müller, E., 2014. Quantifying Snow Conditions of World Cup Alpine Ski Racing Tracks. In *Science and Skiing VI*. Eds. E. Müller, J. Kroll, S. Lindinger, J. Pfusterschmied, T. Stögg, Meyer & Meyer Verlag, 330-339.

Wolfsperger, F., Meyer, F., Gilgien, M., 2021. The snow-friction of freestyle skis and snowboards predicted from snow physical quantities. *Frontiers in Mechanical Engineering*, 7, 728722. (18 pp.). doi: 10.3389/fmech.2021.728722.

Wolfsperger, F., Meyer, F., Gilgien, M., 2021. Towards more valid simulations of slopestyle and big air jumps: Aerodynamics during in-run and flight phase. *Journal of Science and Medicine in Sport*, 24(10), 1082-1087. doi: 10.1016/j.jsams.2021.05.005.

Wolfsperger, F., Rhyner, H., 2014. Mechanical and dynamical properties of racing snowboards and their modification by different binding plates. In *Procedia Engineering*: Vol. 72. Conference proceedings of the engineering of sport 10., 356-361. doi: 10.1016/j.proeng.2014.06.062.

Bibliography

Wolfsperger, F., Rhyner, H., Schneebeli, M., 2018. Pistenpräparation und Pistenpflege. Das Handbuch für den Praktiker. Davos, WSL-Institut für Schnee- und Lawinenforschung SLF. (pp. 232).

Wolfsperger, F., Szabo, D., Rhyner, H., 2020. How to glide well on wet snow? Can roughness and hydrophobicity lower friction of polymers on snow? *Gliding* (2), 6-14.

Wolfsperger, F., Meyer, F., Gilgien, M., 2019. Towards more valid simulations of slopestyle and big air jumps: snow friction during in-run. 23rd International Congress on Snow Sport Trauma and Safety. Oral presentation held on 12th April 2019.

Wolfsperger, F., Szabo, D., Rhyner, H., 2016. Development of alpine skis using FE simulations. In *Procedia Engineering* 147. Conference proceedings the engineering of sports 11, 366-371. doi: 10.1016/j.proeng.2016.06.314.

Wolfsperger, F., Ziegler, S., Schneebeli, M., Löwe, H., 2022. Evaluation of the InfraSnow: a handheld device to measure snow specific surface (SSA). International Symposium on Snow 2022, Davos. Poster presentation held on 26th Sept.. doi: 10.13140/RG.2.2.31566.95047.

Ziegler, S., 2005. Schneefeuchtigkeitsmessgerät. Bachelor thesis at Hochschule für Technik und Informatik Burgdorf.

Ziegler, S., 2006. Schneefeuchtigkeitsmessgerät. Master thesis at Hochschule für Technik und Informatik Burgdorf.

Appendix

Ski/Snowboard-snow friction field measurements: Supplementary materials

Table A1: Coefficients and their standard errors of the multivariate models.

	parameter	coefficient (-)	standard error (-)	relative standard error (%)
SKI	Intercept	2.954E-02	2.603E-03	9
	PR	-1.419E-05	6.857E-06	48
	SSA	1.183E-03	8.041E-05	7
	TLWC	1.630E-03	4.228E-04	26
	PR · TLWC	-8.812E-06	3.480E-06	39
	SSA · TLWC	9.214E-05	1.026E-05	11
SNB	TLWC2	2.215E-04	2.405E-05	11
	Intercept	4.834E-02	6.494E-03	13
	PR	-1.155E-04	5.242E-05	45
	SSA	6.858E-04	1.879E-04	27
	TLWC	8.017E-05	3.502E-05	44
	PR · SSA	3.188E-06	1.743E-06	55
SNB	SSA · TLWC	1.175E-04	1.123E-05	10
	PR2	1.217E-07	7.021E-08	58
	TLWC2	1.973E-04	3.531E-05	18

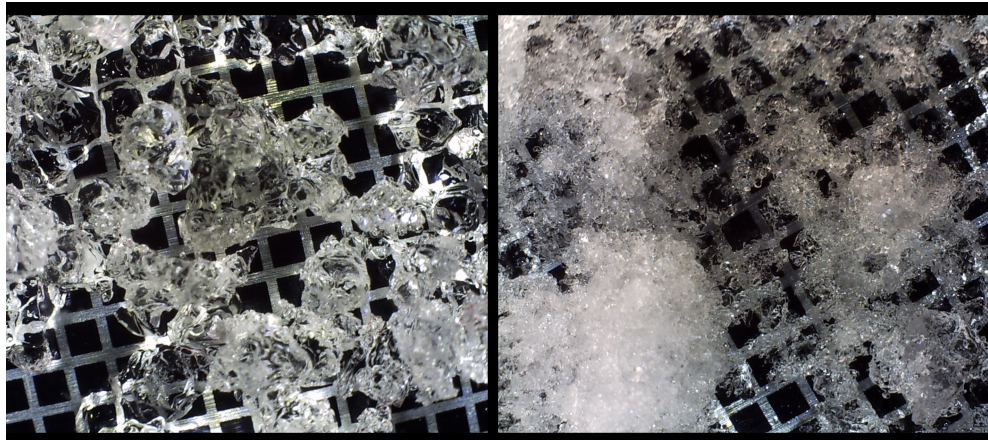


Fig. A1: left) April 8, 2018. right) March 28, 2018.

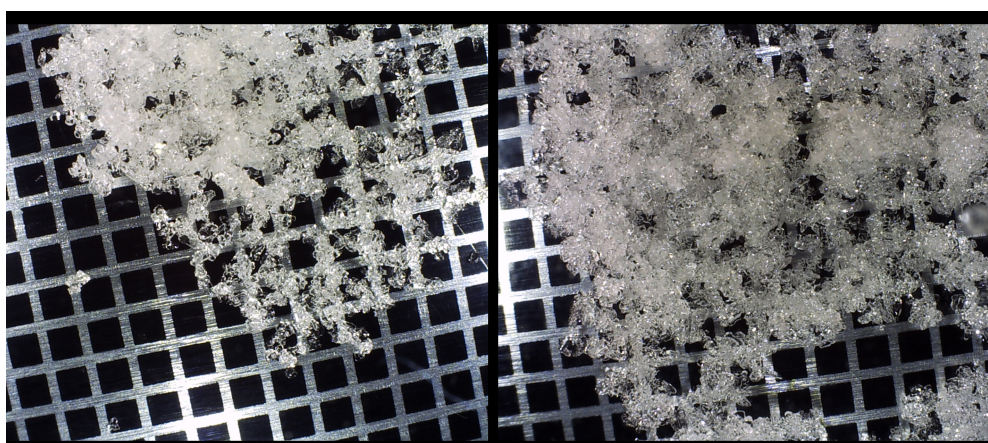


Fig. A2: left) March 4, 2018. right) March 3, 2018.

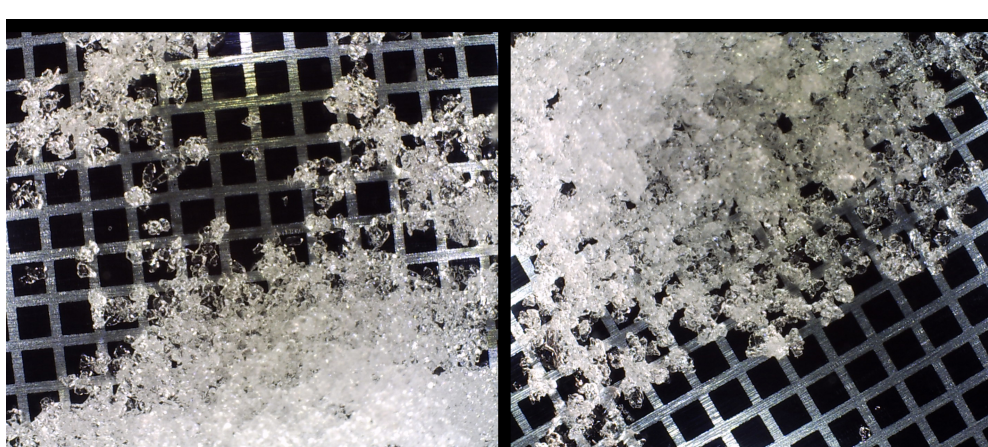


Fig. A3: left) Feb. 22, 2018. right) Feb. 21, 2018.

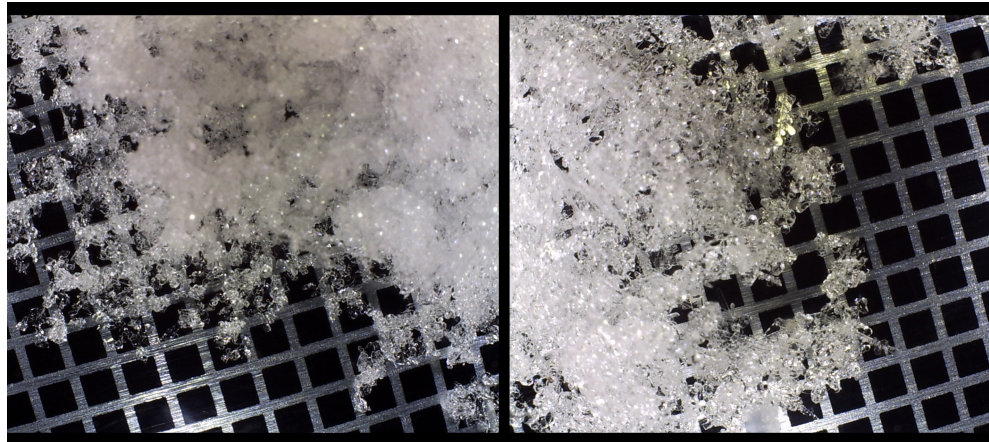


Fig. A4: left) Feb. 13, 2018. right) Feb. 8, 2018.

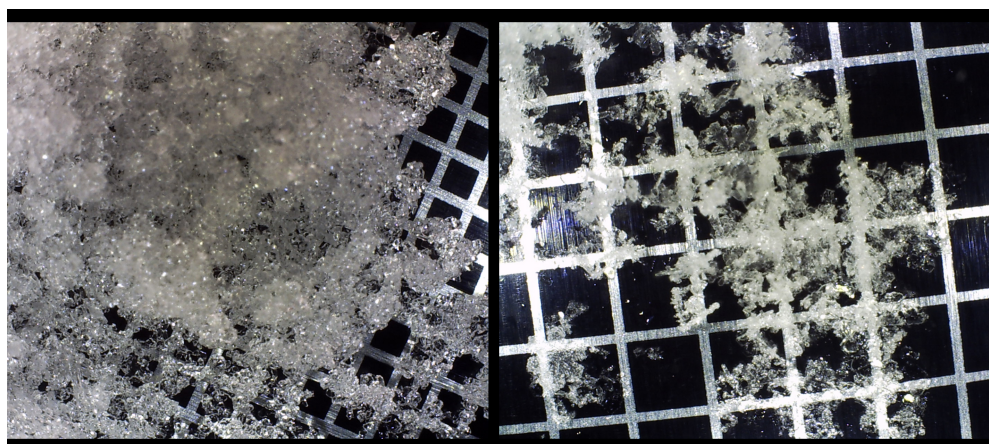


Fig. A5: left) Feb. 7, 2018. right) Feb. 1, 2018. Note that a 2-mm grid board was used.

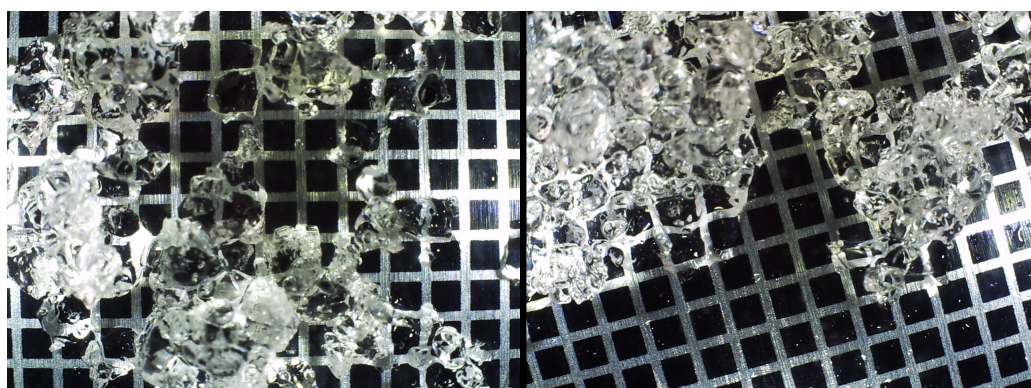


Fig. A6: left) March 31, 2017. right) March 30, 2018.

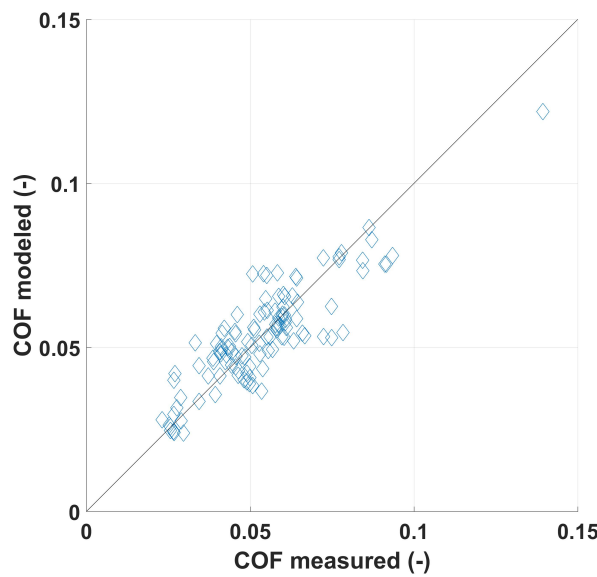


Fig. A7: Comparison of all measured and modeled COF-values for snowboard.

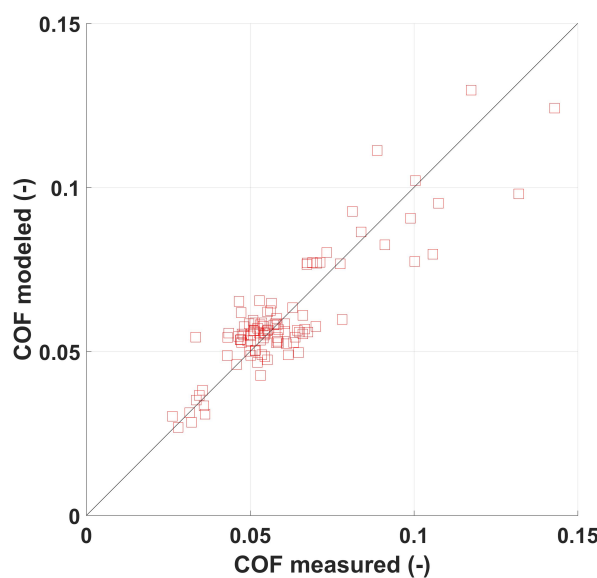


Fig. A8: Comparison of all measured and modeled COF-values for ski.

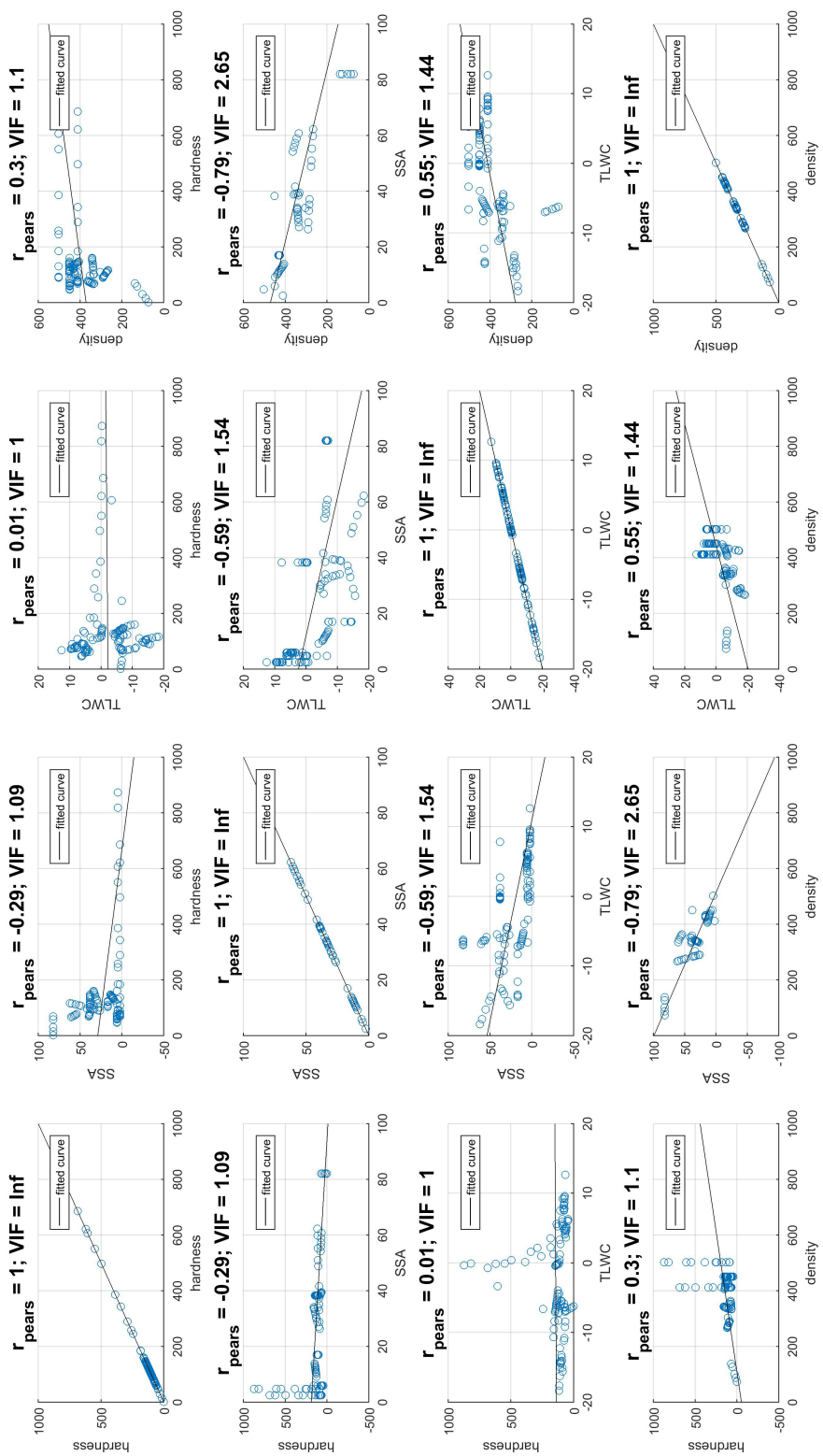


Fig. A9: Scatter plots, pearson correlation coefficient (r_{pear}) and the variance inflation factor (VIF) to identify strong correlations between snow parameters and to quantify the severity of multicollinearity of the multivariate COF-models for the group of skiers.

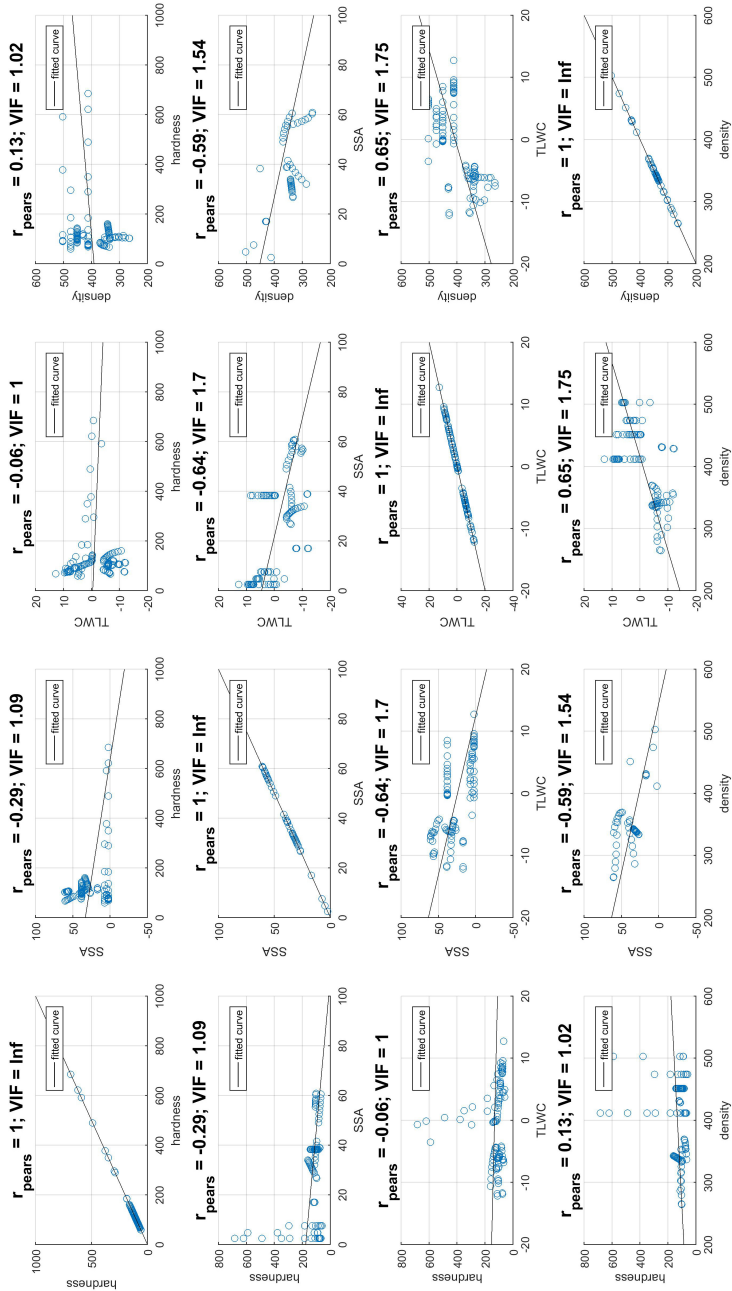


Fig. A10: Scatter plots, pearson correlation coefficient (r_{person}) and the variance inflation factor (VIF) to identify strong correlations between snow parameters and to quantify the severity of multicollinearity of the multivariate COF-models for the group of snowboarders.

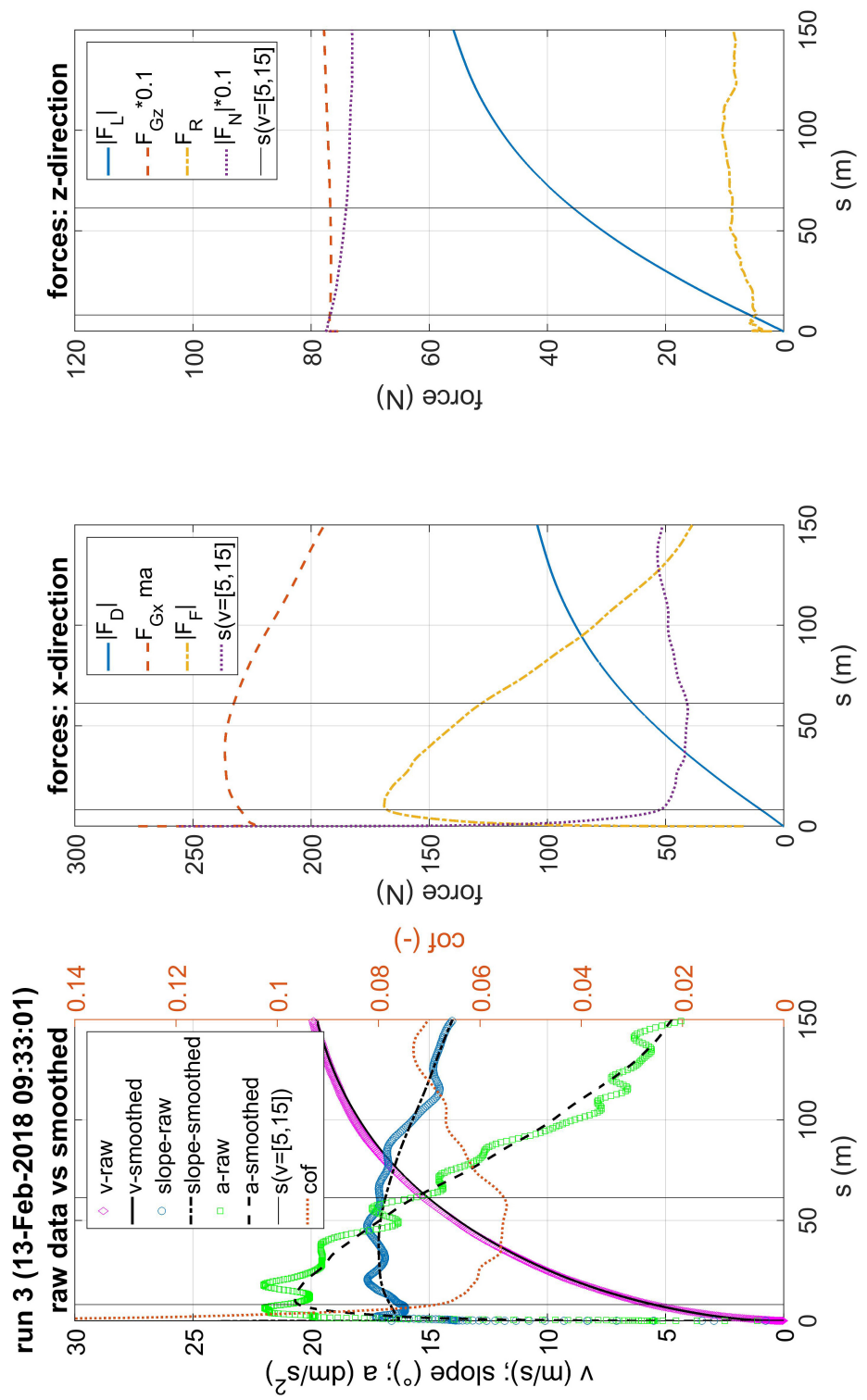


Fig. A11: Example of kinematic data of one run on Feb. 13, 2018. left) Comparison of raw and smoothed data. middle) Force components in x-direction acting on the athlete. right) Force components in z-direction acting on the athlete.

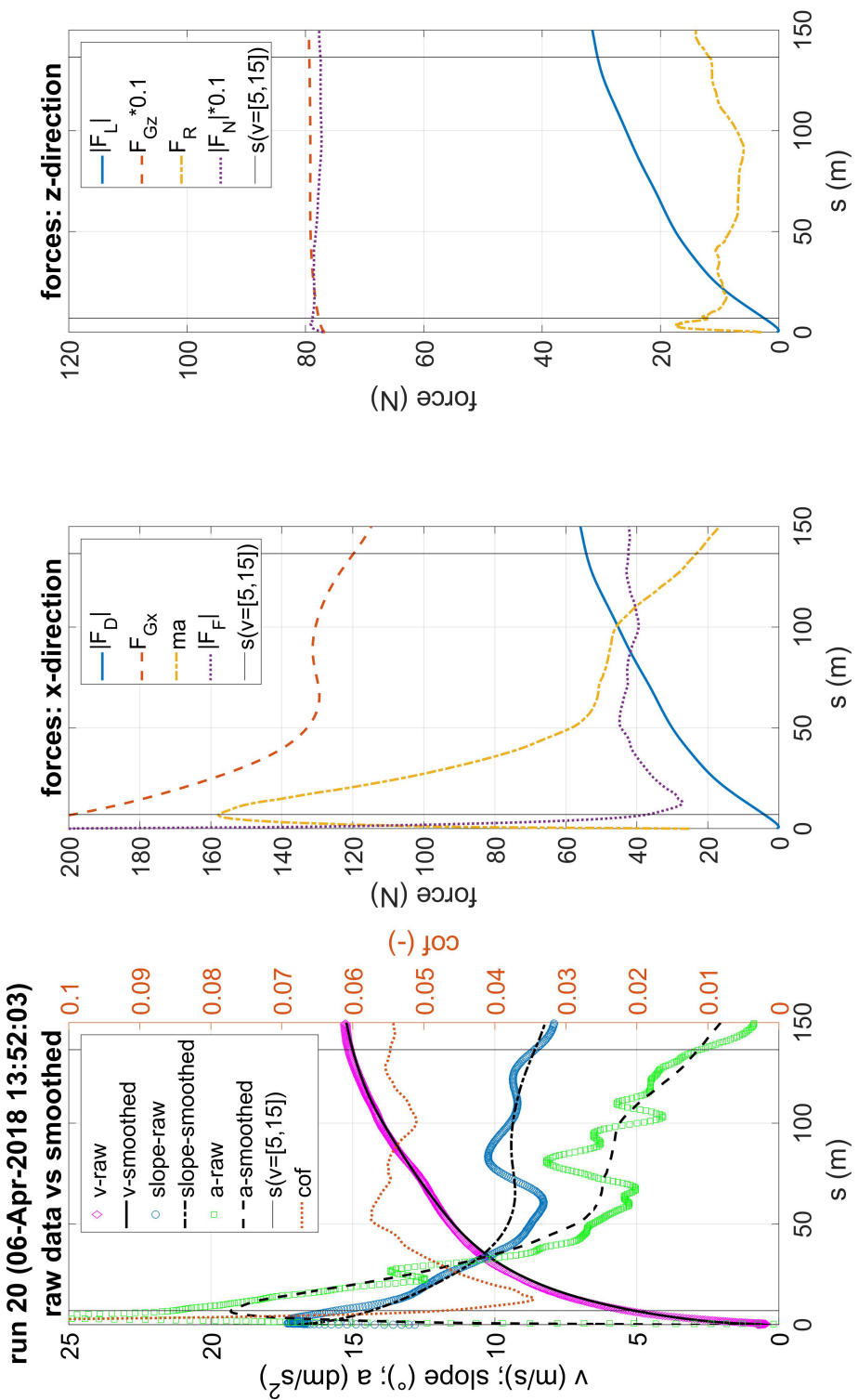


Fig. A12: Example of kinematic data of one run on April 6, 2018. left) Comparison of raw and smoothed data. middle) Force components in x-direction acting on the athlete. right) Force components in z-direction acting on the athlete.

Slider-snow friction laboratory experiments: Supplementary materials

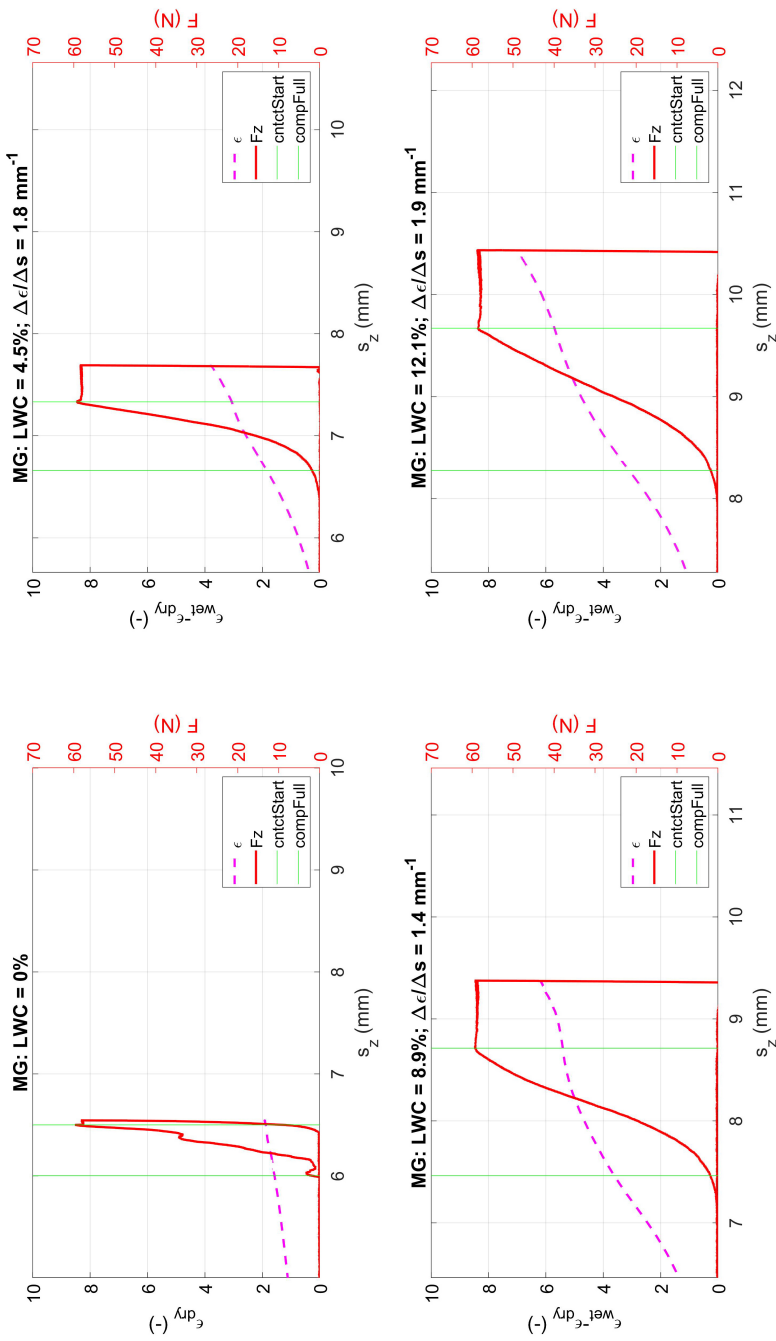


Fig. A9: Permittivity measurements (dashed, magenta) and compression force (red) over compression distance of mid-grained (MG) dry (top left) and wet snow with increasing LWC (top right to bottom left). The vertical lines in green mark the height at initial sensor-snow contact and at full compression.

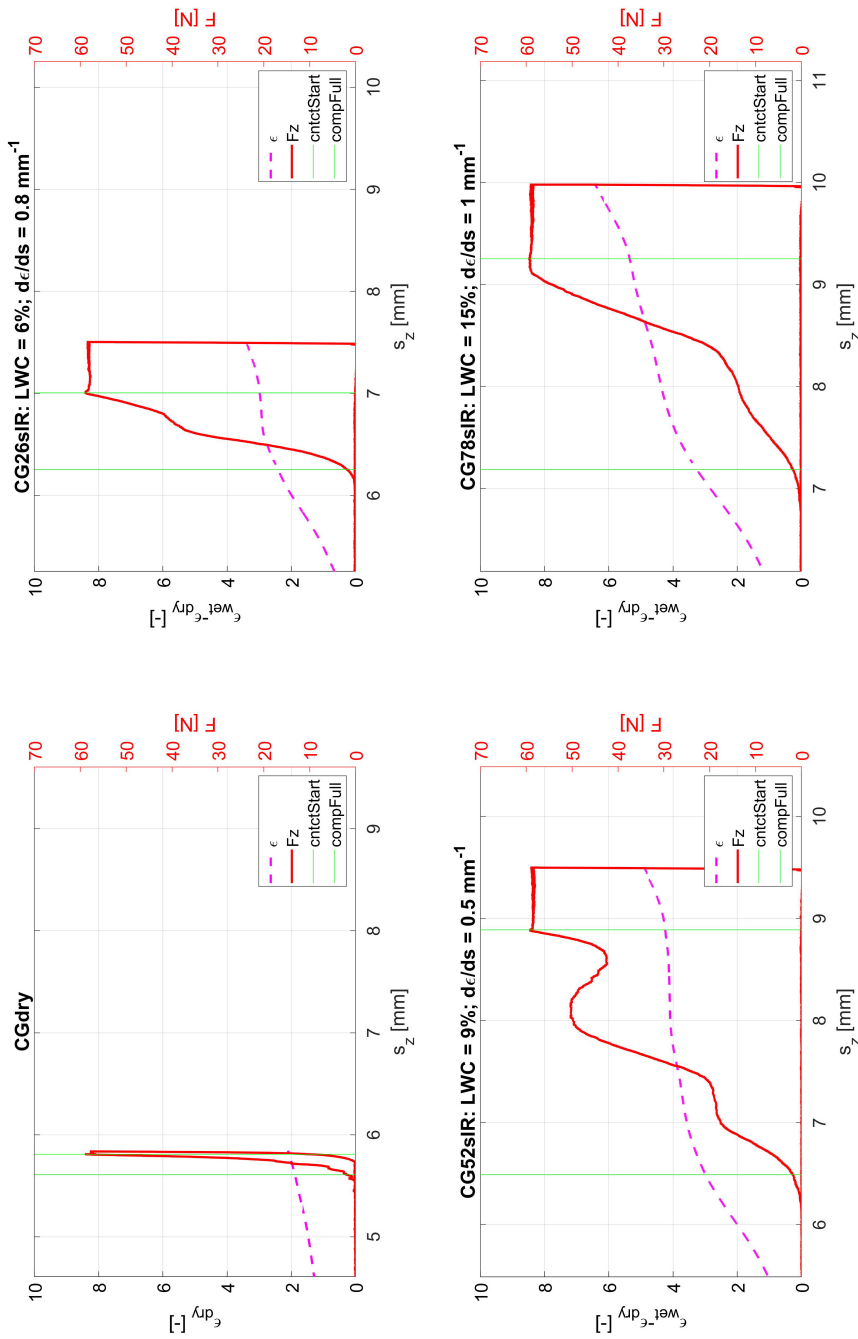


Fig. A10: Permittivity measurements (dashed, magenta) and compression force (red) over compression distance of coarse-grained (CG) dry (top left) and wet snow with increasing LWC (top right to bottom left). The vertical lines in green mark the height at initial sensor-snow contact and at full compression.

InfraSnow development and evaluation

Motivation and idea

The snow microstructure is crucial for any physical process within the snowpack. Measuring snow structural quantities on the field is still limited. Measure snow's SSA from its diffuse near-infrared reflectance (945 nm) combined with a radiative transfer model. Allow non-destructive on-field measurements with an affordable instrument. Therefore, we aimed to develop small batch series of the validated InfraSnow (IS) (Gergely et al., 2014) with a sensor design similar to the existing prototype. Compare lab and field measurements with established methods (IceCube, μ CT & SMP).

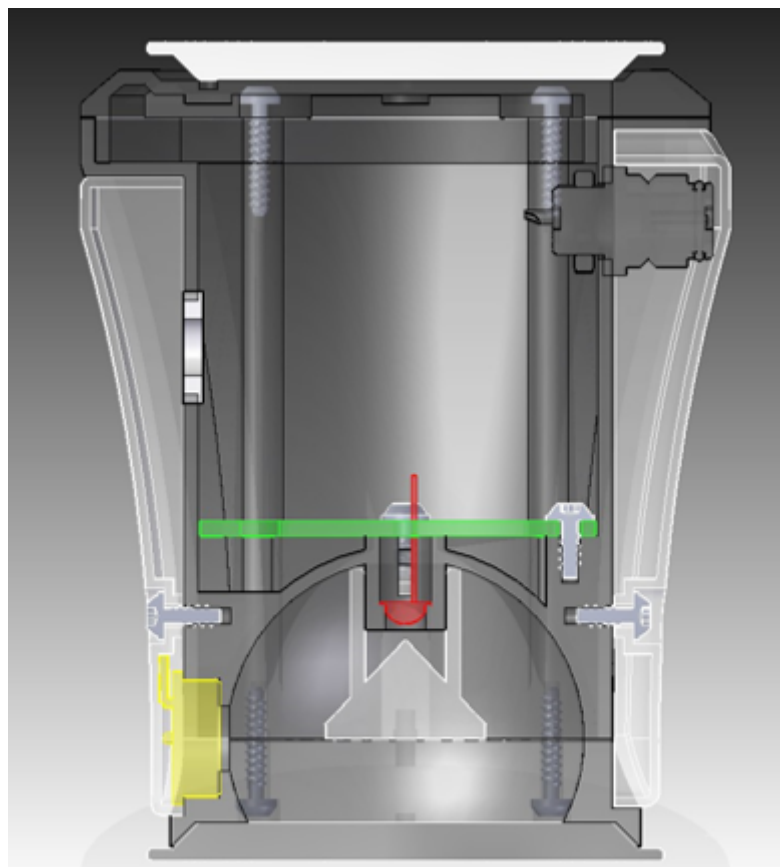


Fig. A11: Cross section of the housing of the InfraSnow showing the integrating sphere ($d = 38$ mm) with the LED light source (red), diffusing cone (white), photodiode detector (yellow), circuit board (green) and the cap which serves as a calibration target.

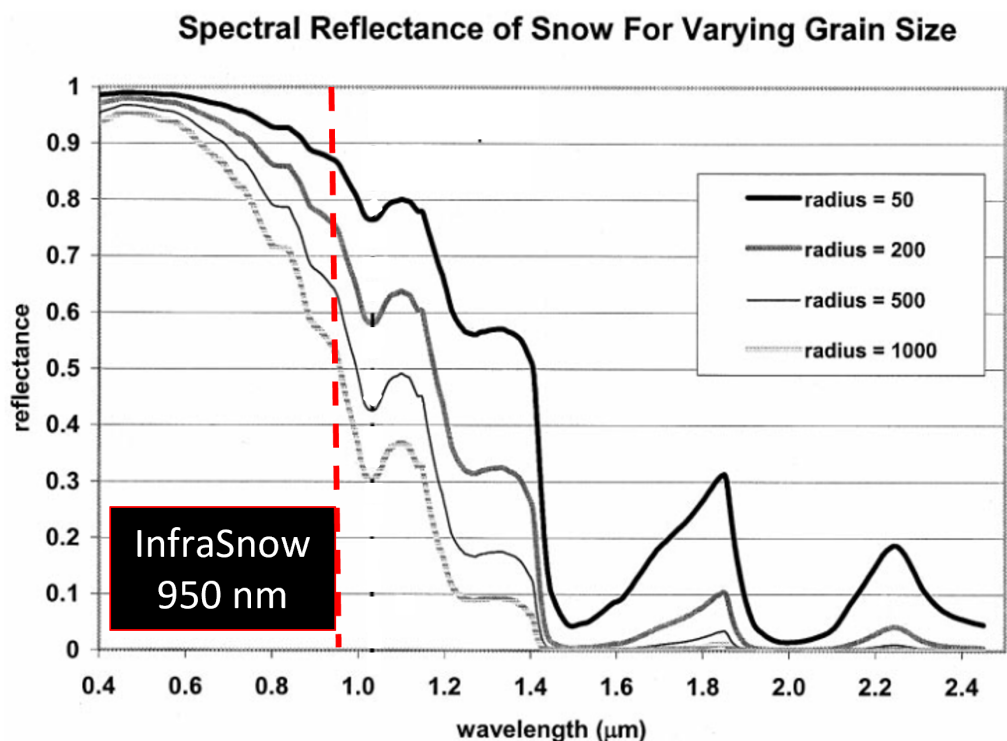


Fig. A12: Spectral reflectance of snow for varying grain size (adapted from Nolin, 2000).

Evaluation of the new prototype

SSA_{IS} deviated -2 % to 81 % ($RMSE_{rel} = 15.2\%$) from the μ CT measurements (Fig. A13)

SSA_{IS} deviated -67 % to 87 % ($RMSE_{rel} = 12.4\%$) from the IC measurements

SSA_{IC} (IceCube) deviated -23 % to 45 % ($RMSE_{rel} = 7.5\%$) from the μ CT measurements

SSA_{IS} deviated on average between -36 % to 10 % from a SSA profile derived from a single SMP measurement (Tab. A1)

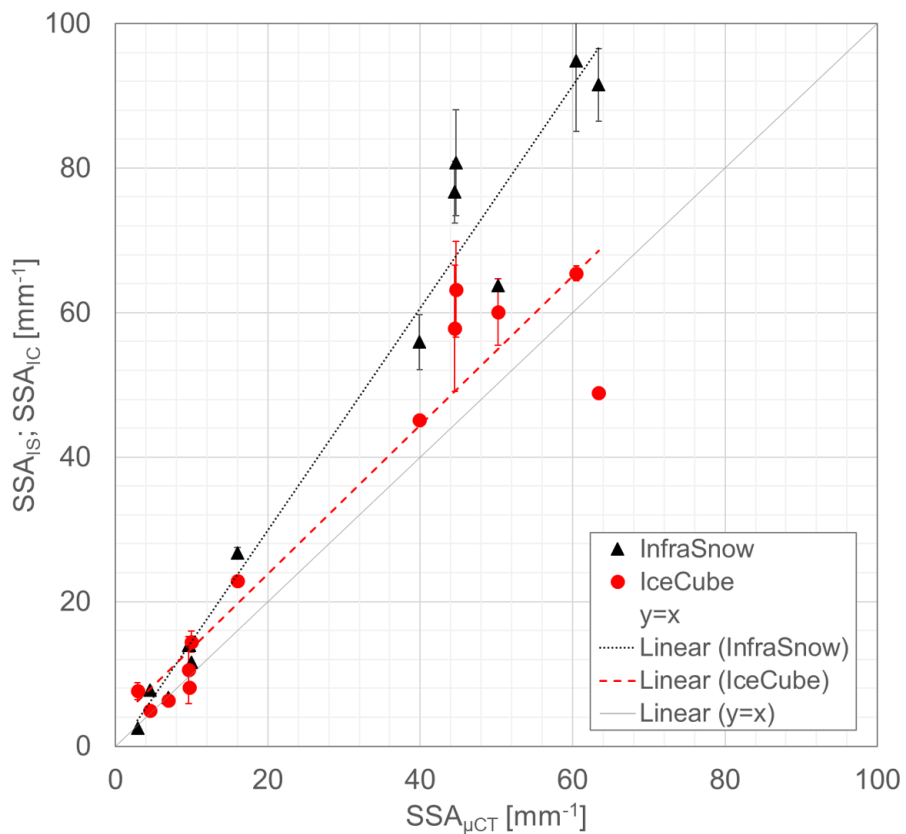


Fig. A13: SSA of 13 snow samples measured in the lab with the InfraSnow and the IceCube versus μ CT reference measurements. The marked (*) data points were excluded from the calculated deviations as the IC snow sampling was limited.

Tab. A2: Minimal, mean, and maximal SSA deviation from a single SSAsMP

date	SSA comparison	e_min [%]	e_mean [%]	e_max [%]
09.12.2021	IS vs. SMP1	-33	-2	144
	IS vs. SMP2	-30	10	185
	IS vs. SMP3	-39	-6	95
15.12.2022	IS vs. SMP1	-45	-15	43
	IS vs. SMP2	-48	-1	56
	IS vs. SMP3	-39	-3	65
22.12.2021	IS vs. SMP1	-56	-19	36
	IS vs. SMP2	-43	-18	56
	IS vs. SMP3	-44	-16	41
12.01.2022	IS vs. SMP1	-55	-29	93
	IS vs. SMP2	-64	-36	64
	IS vs. SMP3	-57	-36	39

Summary an final implementations

IS overestimated the SSA systematically. Therfore, a correction factor k was introduced to fit SSA_{IS} to $\text{SSA}_{\mu\text{CT}}$ ($k = 1.162$; Fig. 5).

Field measurements with a first implementation of k ($= 1.09$) were in good agreement with SSA values deduced from SnowMicroPen (SMP) measurements .

Snow sampling (IC), snow surface preparation (IS), and the snow density ρ (IS) can influence the results considerably: $\pm 20 \text{ kg m}^{-3}$ can lead to an error of up to 20 mm^{-1} . For $\rho > 150 \text{ kg m}^{-3}$ the error propagation remains below 8 mm^{-1}

The InfraSnow is considered an adequate SSA measurement method with an outstanding ease of use

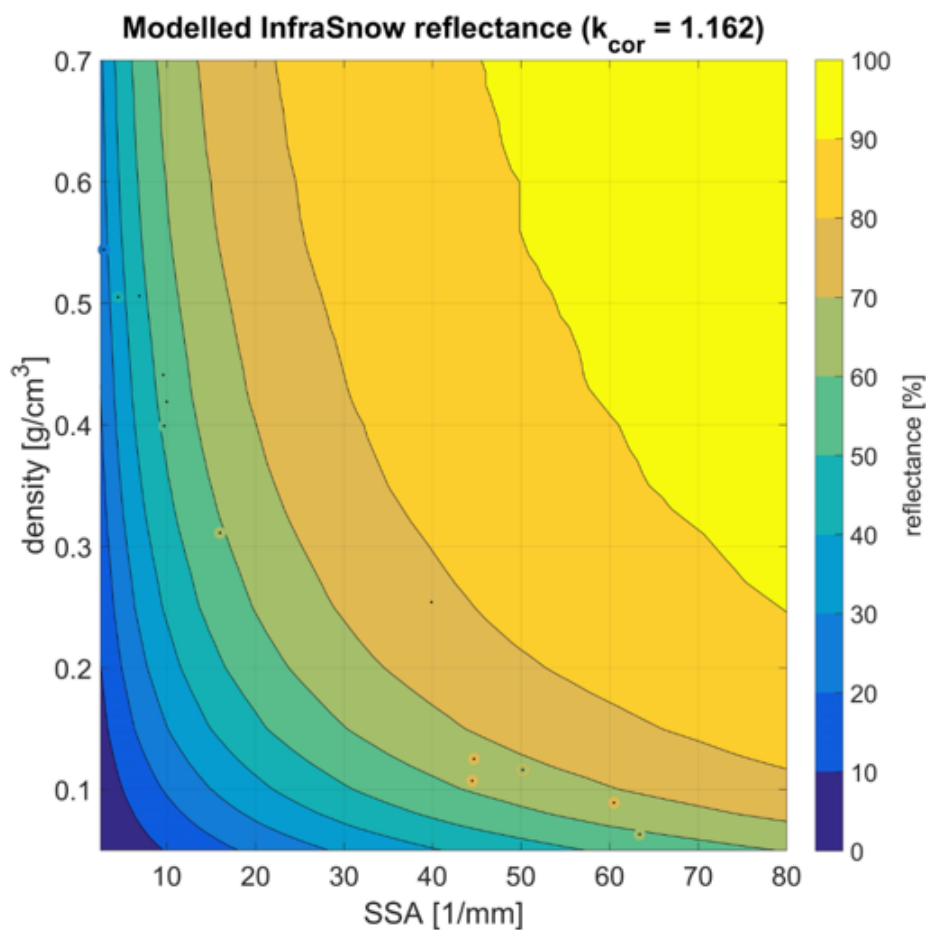


Fig. A14: The expected (model-based) dependency of reflectance, density and SSA of the InfraSnow (contour plot), and the μCT validation data (black dots with colored circle).

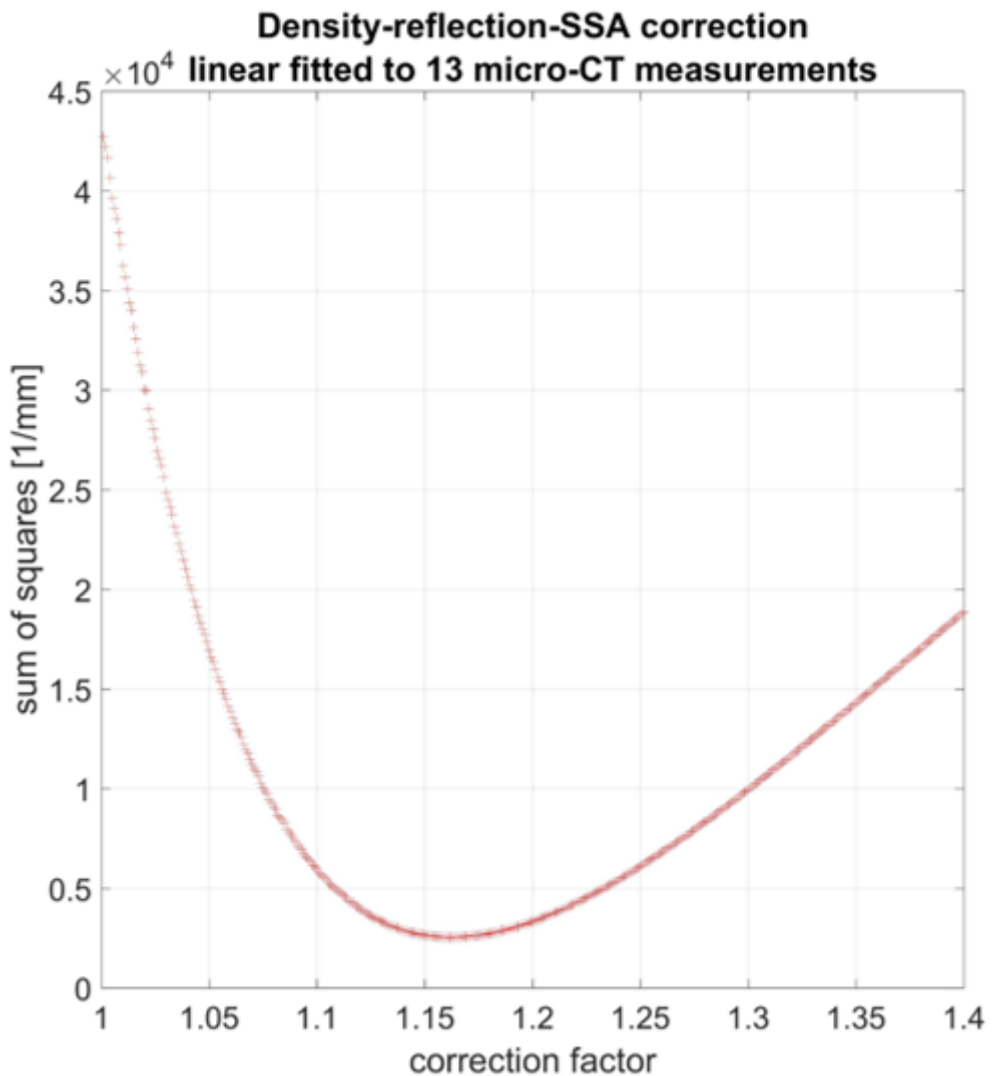


Fig. A15: Sum of squares $\sum(\text{SSA}_{\text{IS}} - \text{SSA}_{\mu\text{CT}})^2$ of 13 snow samples plotted over the linear correction factor to adapt the underlying density-SSA-reflection dependency to best fit SSA_{IS} to $\text{SSA}_{\mu\text{CT}}$.



Fig. A16: InfraSnow prototypes and the ICE CUBE instrument in the SLF cold lab.



Fig. A17: Snow samples preparation in th cold lab.

Curriculum Vitae

Fabian Wolfsperger, was born on the 1st of February 1980 in Freiburg im Breisgau. He visited the Geothe Gymnasium in Freiburg finishing in 1999 with the Abitur. He received the Dipl.-Sporting. degree from Otto-von-Guericke University, Magdeburg, Germany, in 2009. He started 2009 at the WSL-Institute for Snow and Avalanche Research SLF at Davos, Switzerland, as Research Assistant and works today as Technical Staff in the Snow Physics Group. His research interests include the development of snow instruments, interactions of snow and ice with technical surfaces, as well as snow in the context of snow sports and tourism.